MOBILE LIDAR FOR MONITORING MSE WALLS WITH SMOOTH AND TEXTURED PRECAST CONCRETE PANELS

by

Mohammed Dhafer A. Aldosari

A Dissertation

Submitted to the Faculty of Purdue University

In Partial Fulfillment of the Requirements for the degree of

Doctor of Philosophy

Lyles School of Civil Engineering

West Lafayette, Indiana

May 2019

THE PURDUE UNIVERSITY GRADUATE SCHOOL
STATEMENT OF COMMITTEE APPROVAL

Dr. Ayman Habib, Chair

Lyles School of Civil Engineering

Dr. James Bethel

Lyles School of Civil Engineering

Dr. Darcy Bullock

Lyles School of Civil Engineering

Dr. Jian Jin

Agricultural and Biological Engineering

Approved by:

Dr. Dulcy Abraham

This dissertation is dedicated to my parents and wife who have been a source of support and encouragement during the challenges of graduate studies.

ACKNOWLEDGMENTS

First and foremost, I would like to thank my advisor Dr. Ayman Habib for all his advice and support during my Ph.D. studies. He was the first one who introduced me to LiDAR. Without his valuable suggestions on my research and providing excellent study environment, this dissertation would not have been possible. Besides my advisor, I would like to thank the rest of my thesis committee: Dr. James Bethel, Dr. Darcy Bullock, and Dr. Jian Jin, for their insightful comments and encouragement.

My gratitude also goes to my colleagues at Purdue University, especially, Doctors Eui Myoung Kim, Magdy Elbahnasawy, Tamer Shamseldin, Saad Aljadhai, and Ashraf Mahgoub.

I would like also to acknowledge my friends at my previous University (The Ohio State University),that through them I got help. Among them, I would like to thank Justin Crawford, Ahmad Balakhder, and M. Taha Koroglu.

I am grateful to my parents and to my family in Saudi Arabia for their prayers, ceaseless love, support, and endless patience.

Furthermore, I would like to thank my wife, Seham and my kids Renad, Raneem and Dhafer. You are part of happiness in this life, may ALLAH bless you all.

Finally, I would like to thank my country, Kingdom of Saudi Arabia, for funding and supporting my research, specially the King Saud University, my sponsor, for the unwavering support.

TABLE OF CONTENTS

LIST OF TABLES

LIST OF FIGURES

ABBREVIATIONS

AASHTO	American Association of State Highway and Transportation Offcials
DPRG	Digital Photogrammetry Research Group
FOV	Field of View
GNSS	Global Navigation Satellite System
ICP	Iterative Closest Point
ICPatch	Iterative Closest Patch
ICPP	Iterative Closest Projected Point
IMU	Inertial Measurement Unit
INS	Inertial Navigation Unit
L_{cs}	Local Coordinate System
LF_{cs}	Levelled Face Coordinate System
LL_{cs}	Local-Leveled Coordinate System
LPD	Local Point Density
LPS	Local Point Spacing
$lu(S_i)$	Scan-specific laser unit coordinate system
MSE	Mechanically Stabilized Earth
MBR	Minimum Bounding Rectangle
MLS	Mobile LiDAR mapping System
P_{cs}	Panel Coordinate System
RMSE	Root Mean Square Error
SHM	Structural Health Monitoring

TLS	static Terrestrial Laser Scanner
α_L	Longitudinal angular distortions
α_T	Transversal angular distortions
X_o , Y_o, Z_o	The position of the origin of the Panel coordinate system (P_{CS}) relative to the Levelled Face coordinate system (LF_{CS})
θ_{x_P}, θ_{y_P}, θ_{z_P}	The angular rotations representing the relationship between Panel coordinate system (P_{cs}) and the Levelled Face coordinate system (LF_{cs}).

ABSTRACT

Mechanically Stabilized Earth (MSE) walls retain soil on steep, unstable slopes with crest loads. Over the last decade, they are becoming quite popular due to their low cost-to-benefit ratio, design flexibility, and ease of construction. Like any civil infrastructure, MSE walls need to be continuously monitored according to transportation asset management criteria during and after the construction stage to ensure that their expected serviceability measures are met and to detect design and/or construction issues, which could lead to structural failure. Current approaches for monitoring MSE walls are mostly qualitative (e.g., visual inspection or examination). Besides being time consuming, visual inspection might have inconsistencies due to human subjectivity. Other monitoring approaches are based on using total station, geotechnical field instrumentations, and/or Static Terrestrial Laser Scanning (TLS). These instruments are capable of providing highly accurate, reliable performance measures. However, the underlying data acquisition and processing strategies are time-consuming and are not scalable. This research focuses on a comprehensive strategy using a Mobile LiDAR Mapping System (MLS) for the acquisition and processing of point clouds covering the MSE wall. The strategy produces standard serviceability measures, as defined by the American Association of State Highway and Transportation Officials (AASHTO) – e.g., longitudinal and transversal angular distortions. It also delivers a set of recently developed measures (e.g., out-of-plane offsets and 3D position/orientation deviations for individual panels constituting the MSE wall). Moreover, it is also capable of handling MSE walls with smooth or textured panels with the latter being the focus of this research due to its more challenging nature. For this study, an ultra-high-accuracy wheel-based MLS has been developed to efficiently acquire reliable data conducive to the development of the standard and new serviceability measures. To illustrate the feasibility of the proposed acquisition/processing strategy, two case studies in this

research have been conducted with the first one focusing on the comparative performance of static and mobile LiDAR in terms of the agreement of the derived serviceability measures. The second case study aims at illustrating the feasibility of the proposed strategy in handling large textured MSE walls. Results from both case studies confirm the potential of using MLS for efficient, economic, and reliable monitoring of MSE walls.

1. INTRODUCTION

1.1 Background

The technology of mechanically stabilized earth (MSE) walls construction, first proposed by Henri Vidal in the 1960s, has been extensively used in the U.S. since the 1970s (Koerner and Koerner, 2011). MSE walls are earth retaining structures that are constructed by placing alternating layers of reinforcement and compacted soil behind a facing element to form a composite material which acts integrally to restrain lateral forces. MSE walls retain soil on steep, unstable slopes with crest loads. MSE wall systems have a large number of applications; and many public and private entities participate in their development and implementation, including highway agencies and transportation engineers and industrial and residential private developers. Approximately 40,000 MSE walls have been built in the U.S., and 75% of them are constructed as modular block-faced panels (Koerner and Koerner, 2011). MSE walls are so commonly used in the U.S. not only because of their low construction cost, aesthetics, and ease of installation, but also their ability to tolerate large total and differential settlement without structural distress compared to cast-in-place concrete walls (Schmid, 2011; Abu-Hejleh et al., 2001). For example, in the state of Indiana, there are roughly 1,200 to 1,500 MSE walls, excluding those on local public agency (LPA) routes (Rearick and Khan, 2017).

MSE wall panels are constructed using pre-cast concrete modular facing blocks (Lin *et al.*, 2019). The panels are manufactured in various shapes and sizes and several architectural finishes with a facing that is either smooth or textured, and then are usually installed on the project site. One of the main functions of an MSE wall facing panel is preventing backfill soil materials from leaking out of joints; in other words, these panels prevent erosion while permitting excessive water to exit through them.

MSE walls are comprised of many parts, including a reinforced area behind the face that essentially consists of many compacted backfill layers, geosynthetic or metallic reinforcements, foundation soil or rock, and precast concrete panels (Lin *et al.*, 2019; Passe, 2000). The system is compatible with many types of reinforcements, including geotextiles, geogrids, geosynthetic, and steel meshes. These components are shown in Figure 1.1.

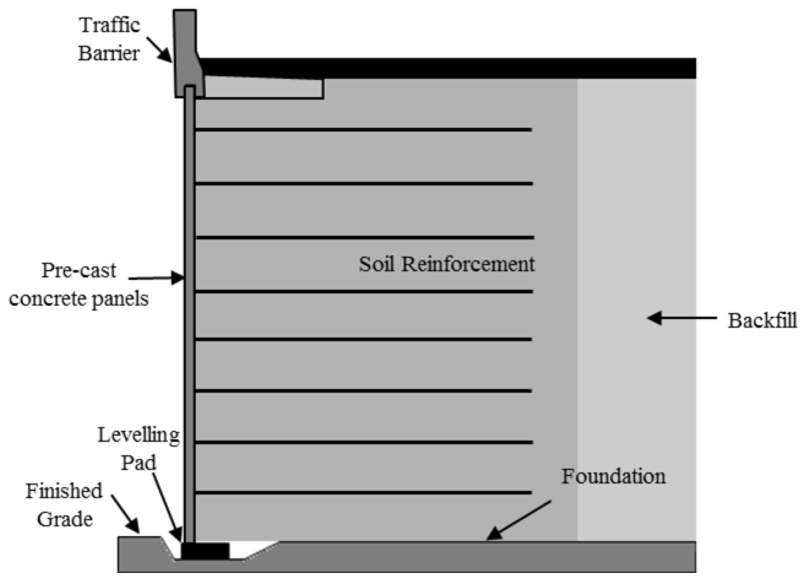

Figure 1.1 Typical cross section profile of an MSE wall (modified after Passe, 2000)

The geotechnical design of an MSE wall structure is inspected mainly for its internal and external stability to meet the intended standards and performance measures. Vertical displacements (settlements) of an MSE wall basically depend on the wall's external stability, specifically, the consolidation of the soil beneath it, which depends on the soil type and water content. Large settlements are expected during the early stage of an MSE wall's construction because the soil experiences a new load, resulting in immediate consolidation. When compared to cast-in-place retaining walls, MSE walls built with pre-cast concrete panels are able to accommodate more settlement without impacting the structural condition of the MSE wall. In the short term, MSE walls are monitored upon installation to ensure that settlement of the foundation has stopped so that the subsequent construction activities over it that are not tolerant to settlement can take place, such as slabs, traffic barriers, and pavements. The internal stability inspection process focuses on the reinforcement tensile strength leading to reinforcement spacing intervals, the connection strength between the facing and reinforced soil mass, and the resistance of soil pullout (Lin *et al.*, 2019; Oskouie et al. 2016).

The internal stability of an MSE wall is affected by the type of backfill selected and the excessive dynamic loads expected, such as moving traffic on pavements. Horizontal movements (lateral displacements) of an MSE wall depend mainly on its internal stability and are caused by the pullout of the soil reinforcement. These horizontal movements are generally observed as the MSE wall is constructed. Limiting the lateral displacements to less than the tolerable value prevents undesirable settlements and damage to surrounding structures and transportation infrastructure, such as pavements (Koerner and Koerner, 2011). Displacements greater than pre-specified thresholds potentially may result in critical damage that is detectable by visual inspection as shown in Figure 1.2 and Figure 1.3 (Lin *et al.*, 2019 and Oskouie et al. 2016).

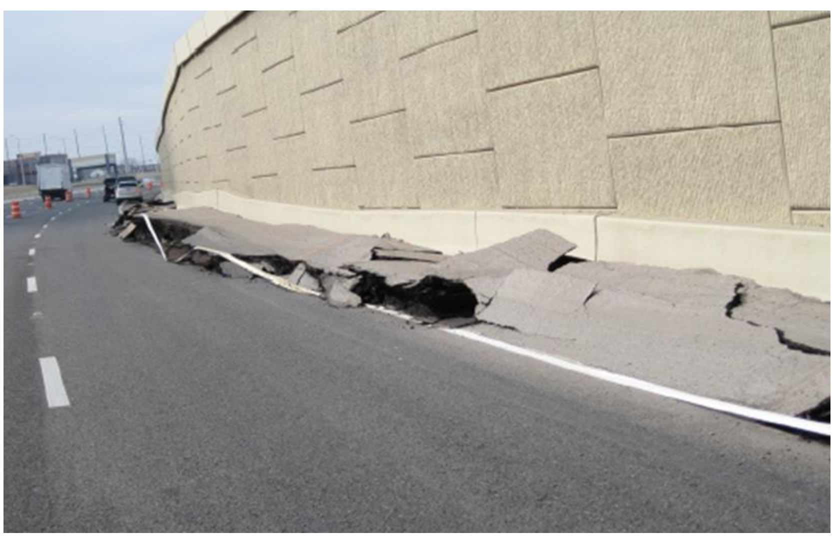

Figure 1.2 Failing of pavement because of design issue (Schmidt, 2011)

Figure 1.3 Failing of MSE Wall because of the panel collapse

MSE walls, like other infrastructure systems, are periodically monitored according to the agency's asset management criteria during and after the construction stage to ensure that their expected performance measures are met. Infrastructure monitoring is the process of discovering damages or changes in the geometric characteristics of civil infrastructure systems. The damages in question are caused by the expansion of material defects under certain loading conditions or the erosion of the material around the soil reinforcement. Damage may occur from a single sudden event (e.g., an earthquake) or can accumulate over a long period of time. The presence of such damage signifies that changes have occurred in the material and/or the geometrical properties of the infrastructure system. If the damage is left untreated, it can grow to the point of failure (i.e., the system no longer operates within acceptable standards) (Farrar and Worden, 2007). Examples of damage include material cracking, corrosion of steel reinforcements around the soil, and excessive movement or excessive bending of the steel. Depending on the civil infrastructure system, infrastructure monitoring is conducted to reach submillimeter precision measurements and is typically performed by static terrestrial laser scanners (TLS) (Chang et al., 2003).

Civil infrastructure systems have many structural members so the failure of one member will not cause an immediate failure in the whole system. However, not being able to specify which member is causing the failure makes the identification and localization of the failure challenging. Accurately monitoring MSE walls is critical for detecting design and/or construction problems that may lead to damages, such as cracks in a wall facade or highway pavement or a structural failure in the facing panels.

A variety of techniques that utilize a range of instruments have been used to study and monitor the performance measures of MSE walls. Some of the current MSE wall monitoring techniques are based on highly qualitative approaches (e.g., visual inspection or examination) and very traditional approaches, such as the measuring tapes and plumb lines. Such techniques often have inconsistencies due to human subjectivity that vary over time (Oats et al., 2017). Visual inspection and other traditional approaches are the primary form of infrastructure systems evaluation used to support decisions relating to their safety, maintenance, and repair (Chang et al., 2003). This assessment includes many steps, such as observation, data collection, analysis, decision-making, and documentation. However, human assessment has certain limitations. First, human inspection is expensive and time-consuming. Civil infrastructure systems also are relatively large and are often in a difficult environment, which introduces challenges in reaching and accessing the critical regions and thus requires a trained inspector in such situations. Second, human inspection can be inconsistent because human abilities and perceptions vary, and the visual data are still manually analyzed and documented by humans. Therefore, depending on an engineer's subjective, qualitative, or empirical knowledge, false evaluations may be followed by inaccurate reports and documents. Third, human inspection is, in some cases, time critical. In other words, there might be an immediate need for decision-making based on visual evaluation in some cases; for example, an immediate response during a disaster to identify repair needs or closure of civil infrastructure systems or discovering a need for unscheduled data collection during a scheduled observation visit.

Other methods of infrastructure monitoring include using ruler scale, total station, global position system (GPS) or TLS systems. These methods are capable of providing high accuracy and reliable performance measures when performed by expensive surveying experts. However, the data acquisition and processing strategy involved in these methods (1) are time-consuming and include tedious work, (2) may be subject to physical or traffic limitation, and (3) have not been fully tested when dealing with special textured MSE walls. Even though total station surveying is commonly used, the low redundancy of surveyed points and setup errors of the total station can result in errors in the serviceability measures of MSE walls. Another disadvantage is that the specific points for possible deformation monitoring must be marked and only this specific region on the infrastructure is monitored before the field work, which results in a spare network of discrete points. Also, these data may not be sufficient in some cases to extract reliable information from the infrastructure being monitored. These points should be accessible for measurement by operators during the field work campaigns, which imposes a risk of damage in the case of failure of the civil infrastructure systems (McGuire et al., 2016).

Due to the large number of existing MSE walls, the limited monetary resources, and the time-critical needs that exist, the frequency of scheduled inspections is not always sufficient to detect problems in a timely manner. In order to verify the structural integrity of infrastructure systems, an ultra-high-accuracy wheel-based Mobile LiDAR mapping System (MLS) has been developed to efficiently acquire data in a short time for monitoring MSE walls. In addition, MLS is capable to operate in the special conditions typical for construction works (e.g., presence of vehicles, obstacles, etc.).

MLS can be used to derive standards and recently-available serviceability measures as proposed by Lin et al. (2019). These measures include out-of-plane-offsets, three-dimensional position, and angular deviations for the panels that constitute the MSE walls. The MLS is a complete multi-tasking monitoring system and is usually comprised of the following: (i) a platform and power supply; (ii) a control module; (iii) an imaging module; (iv) a positioning and orientation module; and (v) a data processing module. The kinematic platform can be a land vehicle, a backpack carried by a human operator, an air vehicle, or a marine vehicle, either manned or unmanned, that provides a sufficient power supply for the mission operation. The control module is responsible for data acquisition based on a time or distance interval. The imaging module may include video cameras, digital cameras, and/or laser scanners. The positioning and orientation module is the most expensive component and the most crucial for the determination of the geographic location of ground objects and encompasses a global navigation satellite system (GNSS) receiver, an inertial measurement unit (IMU), and/or a distance measurement instrument (DMI) (Shamseldin, 2018).

1.2 Research Objectives

This dissertation presents a systematic and scalable approach that can handle smooth or textured precast concrete panels for monitoring the measurement of deformations of MSE walls. It further provides a mathematical characterization of the relative three-dimensional position and orientation of all MSE wall facing panels as well as an overall statistical information report pertaining to meeting standards and new available performance measures. This systematic approach enables effective monitoring and assessment of the long-term performance of MSE walls.

The aim of this approach is to maximize useful information about the MSE wall components (each panel) being examined while minimizing the subjective human intervention required by traditional approaches. Providing civil engineers with feedback on the monitored MSE walls is expected to assist in the decision-making process regarding timely precautionary steps during the design and/or construction stages.

The objectives in this dissertation are as follow:

1. Development of a monitoring strategy that could be used for the delivery of both standard and recently-available serviceability measures,
2. The monitoring strategy is based on reliable, scalable data acquisition procedure – more specifically, point clouds captured by a Mobile LiDAR mapping System (MLS) will be used for serviceability measures derivation, and
3. The strategy could handle MSE walls with smooth or textured precast concrete panels along either planar or piece-wise planar façades.

1.3 Scope of work

The field of infrastructure monitoring is extensive, and the types and goals of the assessments conducted vary greatly. This dissertation provides a review of the components of MLS (e.g., type, number, and location of laser scanners), focuses on the data acquisition process and the data processing aspects of MSE walls. The specific focus of this dissertation is the data processing and extraction of information for meeting standard and recently-available measures.

This dissertation does not address the communication (e.g., transmission of signals), data management (e.g., storage), and diagnostics (e.g., forecasting remaining life of MSE wall) aspects of monitoring civil infrastructure. Furthermore, this research assesses the structural deformation of MSE walls (i.e., panels' offsets and angular deviations). Providing further specific structural defects (e.g., cracks and erosions) for maintenance/rehabilitation purposes is out of the scope of this research.

1.4 Structure of the dissertation

The content of the remaining chapters of this dissertation is as follows:

- Chapter 2 – Literature review of MSE walls monitoring techniques using laser scanning, MLS and other instruments (e.g., camera sensors). Chapter 2 will cover the existing MSE wall monitoring strategies with an emphasis on those utilizing LiDAR point clouds.
- Chapter 3 – Mobile LiDAR for monitoring MSE wall with smooth precast concrete panels. This chapter is a paper that was submitted to the Remote Sensing Journal.
- Chapter 4 – Mobile LiDAR for monitoring MSE wall with textured precast concrete panels. This is a paper that was submitted to the Journal of Surveying Engineering.

Chapter 3 and Chapter 4 present the developed MLS data acquisition system and the case studies used in this research. In chapter 3, a case study is presented to illustrate that MLS can provide similar performance measures to those derived from TLS for smooth MSE walls. In chapter 4, two case studies are presented with the first one focusing on illustrating the capability or MLS in deriving similar performance measures to those derived from TLS for *textured* MSE walls. The second case study, on the other hand, aims to illustrate that the data acquisition modality and processing strategy are capable of monitoring large MSE walls along a transportation corridor.

- Chapter 5 – Conclusions and recommendations for future work. This chapter concludes with the main findings of this dissertation and the recommendations for future work.

2. LITERATURE REVIEW

2.1 Introduction

As mentioned in Chapter 1, the main objective of this dissertation is threefold. First, it establishes a systematic and scalable apparatus for monitoring an MSE walls-based approach for the measurement of deformations/displacements of MSE walls. Next, it establishes an approach for the mathematical characterization of the relative three-dimensional (3D) position and orientation of all MSE wall facing panels. Finally, it provides overall statistical information reporting of the performance measures for standards as well as recently-available performance measures. The first step is a systematic and scalable approach for monitoring an MSE walls-based approach for the measurement of deformations/displacements of MSE walls. Previous research techniques focusing on the performance measures will be addressed in Section 2.2.

The relevant past research work pertaining to this dissertation is reviewed in section 2.3. Building upon the past efforts, this dissertation proposes a mathematical characterization of the relative 3D position and orientation of all MSE wall facing panels. The chapter concludes with a summary and a discussion of the drawbacks found in the literature.

2.2 Standard Serviceability Measures

Long-term MSE wall performance relies on a well-designed and constructed system that meets the specifications provided by the U.S. Department of Transportation (USDOT). MSE walls require routine inspections to ensure they meet the pertinent structural and safety standards. Internal and external inspections are conducted to ensure that reinforcement rupture and pullout from the facing panels are prevented. A commonly accepted set of serviceability measures include the longitudinal angular distortion (α_L) and the transversal angular distortion (α_T), which were proposed by the American Association of State Highway and Transportation Officials (AASHTO) in 2014. The longitudinal angular distortion (α_L) is defined as the ratio of the differential settlement between two points along the length of the MSE wall to the horizontal distance between them as illustrated in Figure 2.1(a). The transversal angular distortion (α_T) is defined as the lateral deflection of the MSE wall divided by its height, as illustrated in Figure 2.1(b).

Table 2.1 provides the tolerable values for the α_L of MSE walls constructed using incremental pre-cast concrete panels with different joint widths.

During the construction of an MSE wall with incremental pre-cast concrete panels, the tolerable value for α_T when measured with a 10-ft. long straight edge should be less than 1/160. In contrast, at the end of wall construction, (α_T) should be less than 1/240 when measured using a plumb line dropped from the top to the bottom of the constructed wall. To supplement the angular distortions standards, in 2009 the Federal Highway Administration (FHWA) provided guidelines for a tolerable out-of-plane offset of pre-cast concrete panels. According to the guidelines, the out-of-plane offset at any joint should be less than 9.53 mm (3/8 in.) during wall construction. These performance measures are computed during the construction stage and throughout the service life of the MSE wall. Deformations greater than the allowable standard values potentially can result in major damages, such as cracks on MSE wall facings or highway pavements, which are detectable by visual inspection. One should note that the standard serviceability measures are global measures for a given face of MSE wall. These standard measures would not be capable of identifying the part of the MSE wall where the failure occurred. The standard serviceability measures, with the exception of the out-of-plane offset, are global measures focusing on the vertical settlement and lateral deflection of an MSE wall. However, most MSE wall failures are closely related to local deformations, such as relative angular tilt and displacement among neighboring panels. This type of standard measure can lead to incorrect decisions and unnecessary costs for unneeded repairs. However, in most cases, when a failure happens in an MSE wall, it is a local failure. For example, a seepage of soil between panels is considered a local failure in an MSE wall (see Figure 2.2). In contrast, this seepage would be considered a global failure if standard measures were used to check the integrity of the MSE wall. The new available serviceability measures proposed in this dissertation can help pinpoint the exact location of that failure; more specifically, the exact panel can be specified and repaired rather than the whole MSE wall and thereby minimize the time, labor, and materials expended.

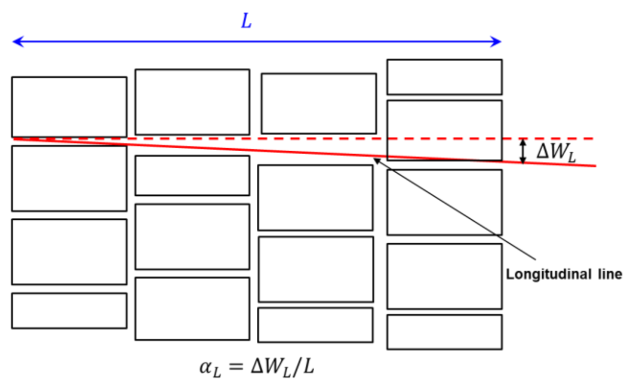

(a)

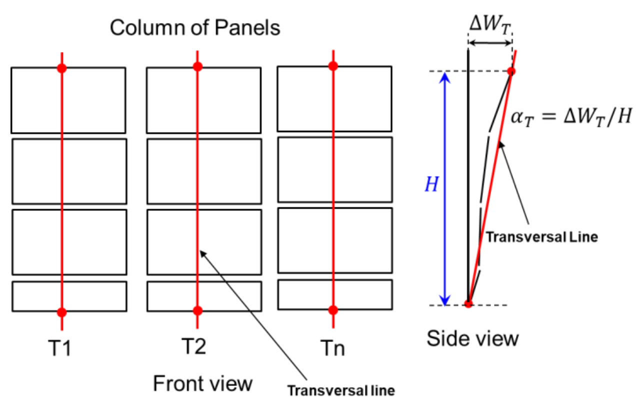

(b)

Figure 2.1 Definition of (a) longitudinal and (b) transversal angular distortions

Figure 2.2 An MSE wall failure due to excessive angular deformation (bulging between neighboring panels)

Table 2.1.Tolerable longitudinal angular distortion (α_T), values of MSE walls constructed with incremental precast concrete panels (modified from AASHTO 2014).

Joint width w_J (in)	Panel area ≤ 2.8 m2 (30 ft2)	2.8 m2 (30 ft2) < Panel area ≤ 7 m2 (75ft2)
19 mm (0.75 inch)	$\alpha_{L,tol}$ = 1/100 = 0.01	$\alpha_{L,tol}$ = 1/200 = 0.005
13 mm (0.50 inch)	$\alpha_{L,tol}$ = 1/200 = 0.005	$\alpha_{L,tol}$ = 1/300 = 0.003
6 mm (0.25 inch)	$\alpha_{L,tol}$ = 1/300 = 0.003	$\alpha_{L,tol}$ = 1/600 = 0.002

2.3 Existing MSE Walls Monitoring Approaches

2.3.1 Traditional Approaches

Infrastructure monitoring is a process designed to determine the damages or changes in the geometric characteristics of civil infrastructure systems at regularly scheduled intervals. Monitoring structural elements includes checks such as measuring deflections and detecting and characterizing cracks. The measurement of deflections is necessary to verify that deformations are occurring within the expected limits, which is important in terms of assessing the physical condition of civil infrastructure systems (Olsen *et al.*, 2009). Deformation monitoring of civil infrastructure systems is particularly important to ensuring both the public safety and the serviceability of the structure (Detchev *et al.*, 2013). Damage in MSE walls is caused by the expansion of material defects under certain loading conditions or the erosion of material around the soil reinforcement. Damage may occur from a single, sudden event (e.g., an earthquake) or can accumulate over a long period of time. The presence of damage signals that changes are taking place in the material and/or the geometrical properties of the infrastructure system. If the damage is left untreated, it can grow to the point of failure (i.e., the system no longer operates within acceptable standards) (Farrar and Worden, 2006). Examples of damage are material cracking, corrosion of steel reinforcement around the soil, and excessive displacements or bulging (Figure 2.3) (Chang *et al.*, 2003).

Figure 2.3 Relative concrete facing panel movement (bulging)

Infrastructure monitoring includes checks such as displacements/movements in any direction as well as angular rotation. Accurately monitoring civil infrastructure is critical for detecting design and/or construction problems which may lead to damages such as cracks on a wall façade and highway pavements or failures in facing panels. Several research initiatives are currently using static terrestrial laser scanning (TLS) for deformation estimation, which will be reviewed along with some geotechnical techniques in the next two subsections.

2.3.1.1 Visual Inspection

A variety of techniques employing a range of instruments have traditionally been used to study and monitor the performance of MSE walls. Some of the current MSE wall monitoring techniques are based on highly qualitative approaches, such as visual inspection or examination, and very traditional approaches, such as measuring tapes and plumb lines. These techniques may produce inconsistencies due to human subjectivity, which can introduce variance over time (Oats *et al.*, 2017). Visual inspection and other traditional approaches are the primary form of infrastructure systems evaluation used to support decisions relating to their safety, maintenance, and repair (Chang *et al.*, 2003). Visual inspection can provide broad information about the status of a structure's engineering components. For example, the inspection should be at such a level of detail as to discover all indications of deterioration/damage, such as the surface or color of the concrete, cracks, leaching, rust streaks, or deformation (see Figure 2.4). However, the effectiveness of visual inspection depends on the knowledge and experience of the investigator. Broad knowledge in structural engineering, concrete materials, and construction methods is needed to extract the most information from visual inspection. This assessment should include many steps, such as observation, data collection, analysis, decision-making, and documentation.

Figure 2.4 Cracking at the corner of a pre-cast concrete panel in an MSE wall

2.3.1.2 Geotechnical Instruments

In addition to visual inspection, different geotechnical engineering research instruments have been used extensively to inspect the deformation measures of civil/structural engineering, which include inclinometers, wire-strain gauges, optical-fiber sensors, inductive laser transducers, and linear voltage displacement transducers (LVDTs) as explained in González-Aguilera *et al.* (2008), Maas and Hampel (2006), and Mills *et al.* (2001).

The inclinometer commonly used today in different areas of civil engineering was developed from a device built in 1952 by S. D. Wilson at Harvard University. It first became available commercially in the late 1950s by the Slope Indicator Company (Green and Mikkelsen, 1988). Inclinometers, also called tilt sensors, are the main instruments currently used in the industry for monitoring MSE walls. An inclinometer is used in geotechnical engineering to measure the slope or angle of objects based on gravity (Dunnicliff, 1993). The inclinometer system is comprised of several components: wheeled probe, reel, cable, readout unit, and accessories (cable gates, battery chargers, and spare batteries) (see Figure 2.5).

Figure 2.5 Components of inclinometer system (GeoSense, 2014)

The cable is connected to a readout unit and data can be recorded manually or automatically. The inclination of the casing with respect to gravity is measured at incremental depths, and the entire casing profile is obtained by numerical integration. Sets of readings taken periodically enable knowing both the magnitude and the rate of the lateral casing movement to be calculated. The casing is normally set in vertical drill holes or attached to a structure in a vertical position to measure horizontal movements. It also can be set horizontally to measure heave or settlement but will not measure movements in a horizontal plane. Movements of casings inclined up to 45 degrees also may be monitored but with considerably less accuracy. Inclinometers can be used for measuring deformations in landslides, natural slope creep, temporary excavations, earth and rock embankments, slurry walls, shafts, tunnels, lateral pile movements, and settlements beneath tanks, fills, and foundations (Green and Mikkelsen, 1988).

An inclinometer is installed (see Figure 2.6) in a single section of an MSE wall facing to measure deformations. The inclinometer system mainly consists of the inclinometer casings, an inclinometer probe with a control cable, and an inclinometer data recorder. The proper location of the inclinometer for measuring the deformations of an MSE wall is to the rear of the pre-cast panel of the MSE wall facing. A borehole is needed for an inclinometer installation at the wall section, prior to construction, to measure deformation. An inclinometer probe control cable and a wireless data recorder are needed to collect the data for the MSE wall facing deformations in each MSE wall section. The inclinometer casing is spliced for extension according to the wall height during construction (Jiang, *et al.*, 2015).

Different kinds of inclinometers offer accurate measurement up to +/- 0.1 degree of slope or angle for various applications. These sensors are available in configurations and packages to meet various customer demands for measurement range and harsh environmental.

(a)

(b)

Figure 2.6 Inclinometer installation

Another instrument frequently used is the optical-fiber sensor. Optical-fiber sensor technology is based on different measurement principles and has produced several types of instruments capable of measuring displacement, strain, acceleration, vibration, temperature, humidity, and pressure (Udd, 1996).

Electrical strain gages are applied to both geogrids and geotextiles, usually by adhesive bonding or mechanical attachment (Figure 2.7). Data of this type are generated in both the laboratory and the field. Using fiber optic measurements, they are applied to a geosynthetic by weaving or knitting. Within the fiber, markers are set at distances of decimeters to meters whereby the elongation and sometimes the temperature between any two markers is measured. Specifically aimed at geosynthetics, two systems are available. Fiber optic sensors are initially applied to the geosynthetic itself or to an external carrier textile (Figure 2.7) (Schneider-Glöetzl et al., 2010 and (Lostumbo and Artieres, 2011). These systems can measure strain and monitor movement or distortion of the structure. The strips are optimally placed before construction directly on the foundation soil and then incrementally higher in the structure as it is being built. The accuracy of strain measurement is within 0.2% for the GeoDetect® system.

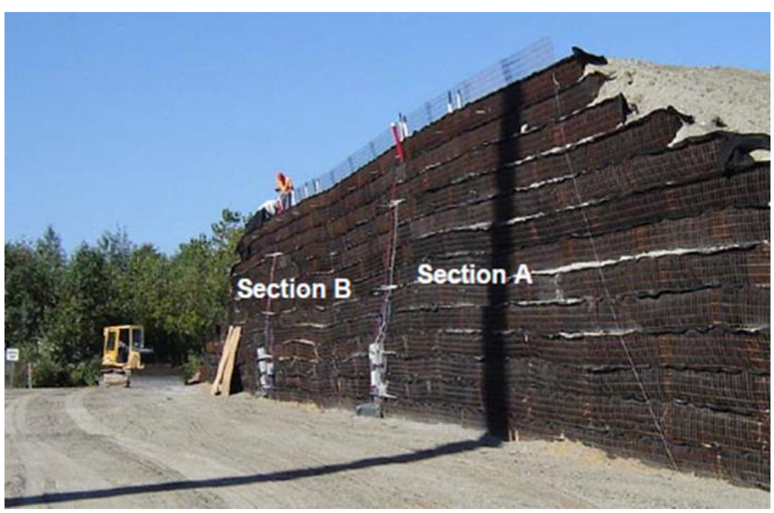

Figure 2.7 Monitoring fiber-optic in a geotextile reinforced wall

In the field of structural monitoring, inclinometers, wire-strain gauges, and optical-fiber sensors likely will replace traditional sensors due to some inherent advantages. They are lightweight, small, passive, low-power, and resistant to electromagnetic interference (Ansari, 2005 and Inaudi and Glisic, 2008). On the other hand, their major drawbacks are high cost and unfamiliarity to the end-users. Fiber optical sensors can measure strain and monitor movement or distortion of the structure and are initially applied to the geosynthetic itself or to an external carrier textile (see Figure 2.7) (Schneider-Glöetzl et al., 2010 and Lostumbo and Artieres, 2011). The strips are optimally placed, prior to construction, directly on the foundation soil and then incrementally higher in the structure as it is being built. These two instruments (the inclinometer and optical-fiber sensor) are mainly used in the geotechnical field to monitor deformation in MSE walls.

Pei *et al.* (2012) proposed a monitoring approach in which in-place inclinometers are used for monitoring lateral displacements of a retaining wall. During data collection, the inclinometer is cast inside a tube around the region of interest. To measure the relative displacement between two points, sensors are glued/taped to the in-place inclinometer. Each sensor provides a strain value. Then, these two strain values are multiplied by two calibration coefficients (C_1, C_2), which are obtained from a linear relationship between a measured strain. Finally, the two values of the sensor strains are multiplied by C_1, C_2 to obtain the vertical displacement and a rotational angle, respectively. Monitoring the deformation is conducted by comparing the acquired data at different times. Brown et al. (2011) produced a retaining wall displacement measurement technique that utilizes different sensors such as optical strain gauges, inclinometers, and moisture sensors. In their study, three locations of a test wall were instrumented. In each of these locations, there were 30 fiber optic strain gauges and one inclinometer casing. During construction, the optical cables were protected within a slotted PVC pipe. During data collection, observations were taken at least once per day for several weeks; later, the measures for monitoring were identified and separated from the strains. Eventually, these measures over a long time period could be evaluated.

Mohamad *et al.* (2011) used an optical fiber strain-sensing and inclinometer technique to monitor the performance of a Secant-Pile Wall. Sensors were attached along the two opposing sides of the reinforcement soil area by first fixing the cable with two clips, and a steel pipe installed at the top of pile was used to protect the fibers. By measuring the strain along two fibers placed symmetrically with respect to the axis, it was possible to monitor the full behavior of a wall. The measured strains (ε_a and $\varepsilon_{b)}$ at two locations were used to derive the amount of vertical and lateral displacement. They conducted comparisons between these instruments and reported their assessment of the wall over a period of time. Kuang et al. (2002) used an intensity-based plastic optical fiber sensor for curvature and strain measurements in samples subjected to flexural and tensile loading conditions, respectively. Their test results showed that it was possible to use the sensor for monitoring the strains on both the tensile and compressive regions of a beam. Yang *et al.* (2009) monitored a cast-in-situ concrete-rigid facing geogrid-reinforced soil retaining wall during construction. The monitoring included the vertical foundation pressure and lateral earth pressure of the reinforced soil wall facing, the tensile strain in the reinforcement, and the horizontal deformation of the facing. Batten *et al.* (1999) utilized a wire strain gauge approach to monitor a constructed deep retaining wall with a type of cast-in-situ concrete-rigid. In the construction stage, wire strain gauges were installed facing a geogrid-reinforced soil retaining wall. Unlike previous studies, the loads from the wire strain gauges were derived, and then the deformations in the vertical and horizontal direction were indirectly obtained.

2.3.1.3 Surveying Devices

In recent years, research has been conducted to develop new types of deformation structural monitoring instruments that can effectively monitor displacement in the horizontal and vertical directions of structures based on optical surveying sensors. These instruments include the level, total station, TLS, digital camera sensors, and GNSS (Gordon *et al.*, 2007; Scaioni *et al.*, *2010*; Wang *et al.*, 2010). TLS has been proposed as a tool to monitor the deformations of MSE walls (Lin *et al.*, 2019; McGuire et al., 2016, 2017; Oskouie et al., 2014, 2016; Olsen et al., 2009; Laefer and Lennon, 2008).

Overview of Light Detection and Ranging (LiDAR)

LiDAR systems onboard static and mobile platforms have emerged as a prominent tool for the direct derivation of accurate point clouds along object surfaces with high density points. A schematic of laser ranging scanning is shown in Figure 2.8.

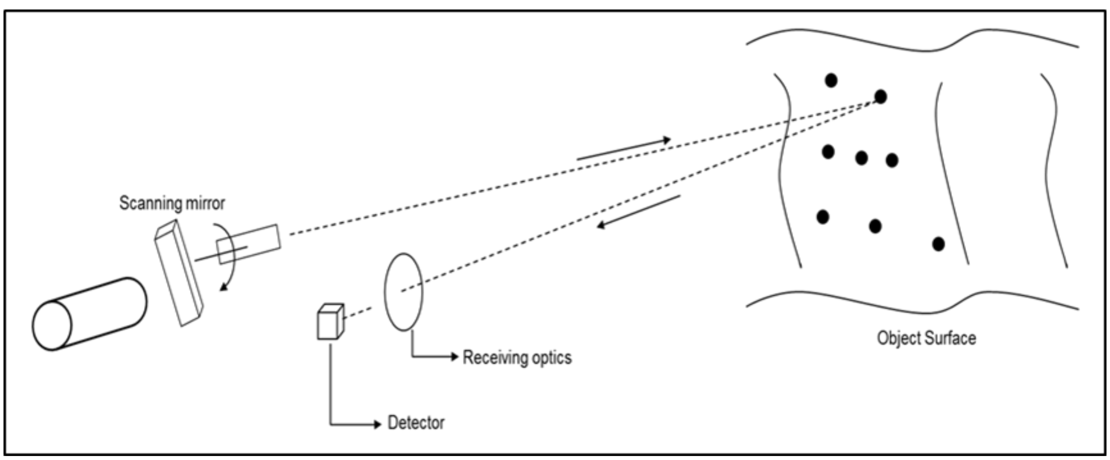

Figure 2.8. Schematic of a laser scanner

The main components of the LiDAR system are the laser, the scanning mechanism and projection optics, the receiver optics, and the platform navigation sensors. LiDAR is used for a variety of applications such as topographic, cultural heritage documentation, industrial site modeling, biomedical applications, and infrastructure monitoring. LiDAR typically operates in the visible or infrared region of the electromagnetic spectrum with respect to wavelengths (Mikhail *et al.*, 2001 and Lin *et al.*, 2019). The main idea behind measuring the distance between the laser beam firing point and its footprint is that the scanner emits a brief pulse of laser light which, after reflection by the object being measured, is sensed by a photodetector. The range (ρ) is derived (in Equation 2.1) from the two-way flight time of the pulse (Δt) (i.e., the time delay between the emitted and received laser pulses) commonly applied in terrestrial LiDAR systems (Habib *et al.*, 2017), where *C* is the velocity of the light.

$$\rho = \frac{C\Delta t}{2} \tag{2.1}$$

The estimated ranges are then combined with the pointing direction of the laser beam - which is derived by built-in mirror steering encoders - to determine the coordinates of the laser beam footprint relative to a local coordinate system associated with the scanner location. The spacing between neighboring points along the scanned surface depends on the horizontal and vertical angular increments for α and β, as well as the distance between the TLS unit and the laser beam footprints. The horizontal and vertical angular increments are set by the user before the scanning process while considering the required resolution as well as the time constraints for the data acquisition process. Finer angular increments can lead to higher resolution but would require longer scan time. TLS technology has matured to the point where most surveying firms have access to scanning units which can produce point clouds with a spatial accuracy in the millimeter to centimeter range (California Department of Transportation, 2011). Derivation of the mathematical relationship between the sensor measurements and the object coordinates of the point cloud equation is shown in Equation 2.2.

$$r_A^{lu} = R_{lb}^{lu}(\alpha, \beta)\, r_A^{lb} = \begin{bmatrix} \rho\, cos\beta\, cos\alpha \\ \rho\, cos\beta\, sin\alpha \\ \rho\, sin\beta \end{bmatrix} \qquad 2.2$$

where,

r_A^{lb} is the range vector.

lb is laser beam point coordinate system (cs).

lu is laser unit coordinate system (cs).

β is the vertical angle.

α is the horizontal angle.

Regarding scanning systems, the laser beam is steered by a mirror that either rotates in a single direction (i.e., linear laser scanners) or in two directions (e.g., elliptical laser scanners). The steering mirror, when coupled either with the internal rotation of the scanning unit or the motion of the carrying platform, would allow for the generation of a dense point cloud along the surrounding objects. The former mechanism is used for static scanning while the latter is used for mobile systems. Multi-beam laser scanners, such as Riegl-VUX-1HA, have several laser beams that point in different directions. A rotational mechanism allows for 360^{o} coverage across the axis of rotation. The field of view along the rotational axis is controlled by the set-up of the laser beams. Modern laser systems are capable of providing up to a million pulses per second. This capability allows for the derivation of highly dense point clouds.

Mathematical Model: LiDAR Point Positioning

For the derivation of the mathematical relationship between the sensor measurements and the object coordinates of the point cloud, it can be started by establishing the different coordinate systems associated with a LiDAR unit. The vector and matrix notations used in this dissertation are as follows:

r_a^b denotes the coordinates of point 'a' relative to point 'b' in the coordinate system associated with point 'b'.

R_a^b denotes the rotation matrix that transforms a vector-defined relative to the coordinate system 'a' into a vector-defined relative to the coordinate system 'b'.

For coordinate systems associated with a single LiDAR unit, the rotation matrix relating the different components is denoted as the boresight matrix, while the spatial offset relating them is denoted as the lever arm. One should note that, for a GNSS/INS-assisted mobile LiDAR unit, the coordinates of a given point *I* relative to the mapping reference frame can be derived through a vector summation process as in Equation 2.3 (Habib *et al.*, 2010, 2018) and displayed in Figure 2.10. In this equation, r_I^m is defined as the ground coordinates of the laser beam footprint relative to the mapping frame while r_b^m(t) & R_b^m(t) are defined as the interpolated position and orientation of the Inertial Measurement Unit (IMU) body frame relative to the mapping frame. Also, r_b^{lu} and R_b^{lu} are defined as the laser unit location and boresight matrix relative to the body frame while R_{lb}^{lu}(t) is defined as the rotation matrix relating the laser beam to the laser unit. In addition, r_I^{lb}(t) represents the position of point *I* with respect to the laser beam coordinate system, as a function of the measured range (ρ), together with the evaluated horizontal and vertical angles (α and β, respectively) by the steering mirror (See
Figure 2.9).

$$r_I^m(t) = r_b^m(t) + R_b^m(t)r_{lu}^b + R_b^m(t)R_{lu}^b R_{lb}^{lu}(t)r_I^{lb}(t) \qquad (2.3)$$

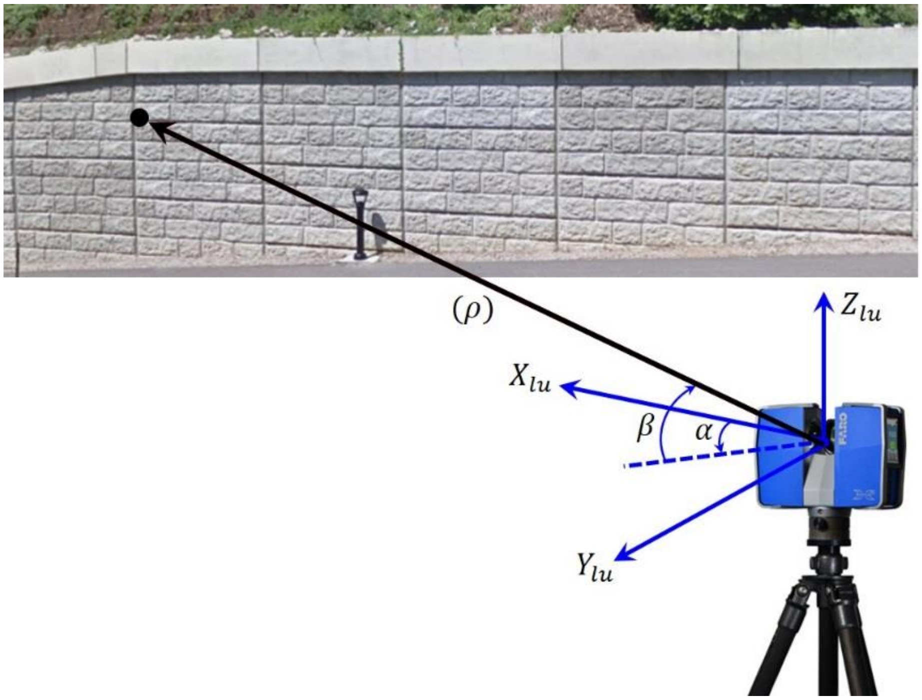

Figure 2.9. Principle of point positioning using a TLS

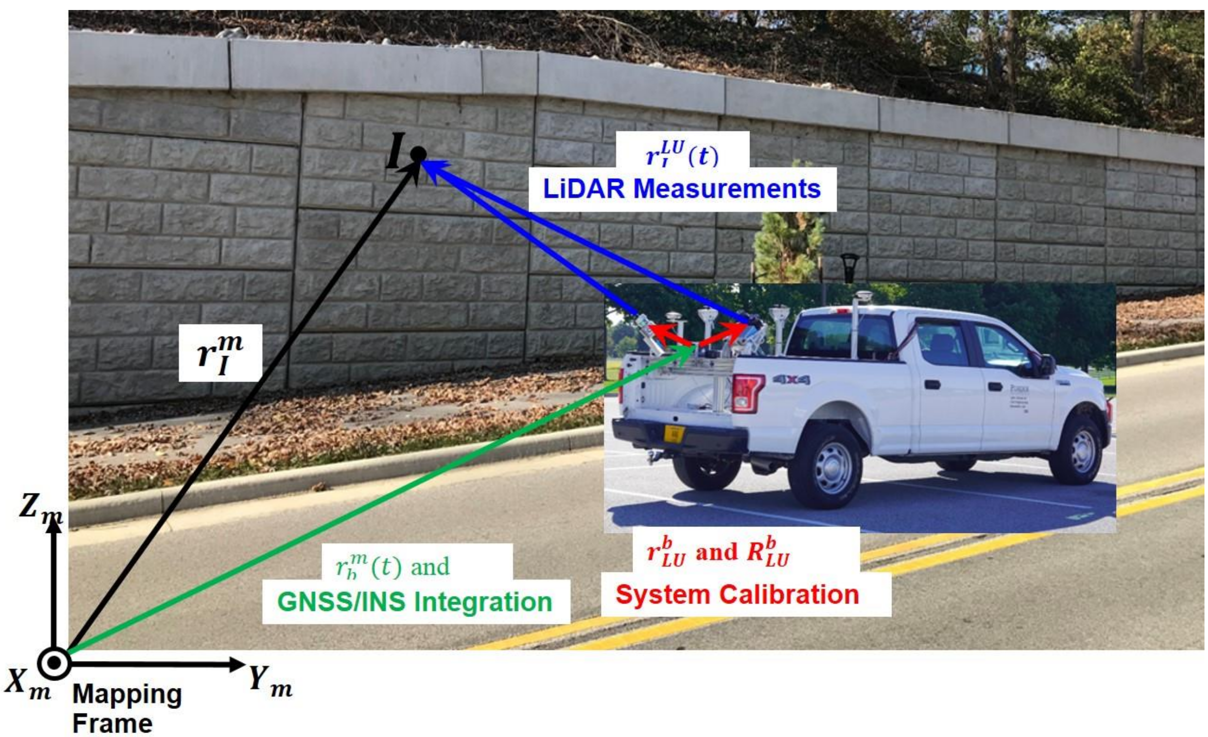

Figure 2.10 Vector Summation in LiDAR Equation

Laefer and Lennon (2008) proposed an approach in which TLS is used to monitor retaining walls. During data collection, fiducial markers (i.e., an artificial target strategically placed within the retaining wall site) are placed. Each scan is required to have common reference targets. These targets are not subjected to any kind of movement and must be exactly positioned in the same place for each scanning mission. The scan locations are derived and used for target-based registration. Once data (collected from different times) was registered to the same reference frame, they evaluated the movement of the vertically stacked panels within the retaining wall. Two major disadvantages of their processing are the time needed to set up the equipment in each location and the time required to scan the reference targets from each scanner location. Their study recommended that the reference targets be left in-situ for the duration of the monitoring course (see Figure 2.11).

Figure 2.11. Spherical target left in the site project for the duration of monitoring a retaining wall

Olsen *et al.* (2009) utilized laser scanners to monitor the deformation of MSE walls and compared the acquired scans at different times. Their study did not report any significant movements for the scanned MSE walls and recommended that such scans be completed on a semiannual or annual basis. Oskouie *et al.* (2014) presented a data processing strategy for MSE wall characterization during the construction phase. Because point clouds collected during construction could include unwanted objects such as temporary steel, wooden brackets, fence, or workers, they removed such objects using the RANSAC algorithm (Fischler and Bolles, 1981). They used manual processing for isolating the column walls (columns of pre-cast concrete) (see Figure 2.12) using the vertical joints. In addition, in order to evaluate the accuracy of RANSAC in removing the outliers and noise from the data, the point clouds for different numbers of columns in the wall were manually cleaned and used as ground truth.

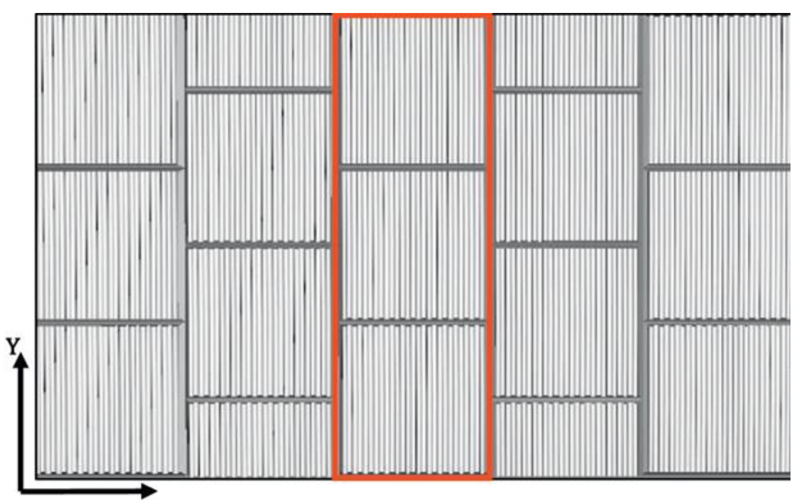

Figure 2.12. Columns of pre-cast concrete along the vertical direction

TopoDoT, a commercial software package that provides semi-automated processing capabilities, can be used to monitor MSE wall settlement and deformation (Knaak, 2012). Before using the package, it is necessary for the user to register multiple datasets to the same reference frame. Then, profiles are manually selected and used for automated joint identification. Then, the distance between the joints from two profiles collected at different times is finally derived. McGuire et al. (2016) used TLS to monitor the vertical and lateral settlement of MSE walls and segmental retaining walls (SRW). Like Laefer and Lennon (2008) in their proposed technique for monitoring MSE walls, McGuire et al. (2016) used multiple tie points (e.g., reference points for registration purposes) with a unique design during their data collection. These tie points are placed and remain untouchable within the MSE wall site during the monitoring program. Each scan is required to have common reference targets, which are carefully installed in the field by excavating a hole (approximately 20 cm in diameter) and concreting the pole while checking to ensure there is proper vertical alignment. The scan locations are derived and used for target-based registration; and the MSE wall profiles extracted from the scanned dataset are used to assess its vertical alignments. The extracted profiles of the same wall at different dates are then used to obtain relative vertical settlements and lateral deflections. To evaluate the accuracy of their proposed method, the vertical and horizontal wall alignments were compared to each other or compared to the construction drawings and specifications. McGuire et al. (2017) utilized both TLS and digital cameras to monitor vertical settlement of segmental retaining walls (SRWs). Similar to the previous studies mentioned above, McGuire et al. (2017) used permanent reference markers (e.g., outlet headwalls, inlet boxes, and raised manhole rims) to register different scans in a common reference frame. For the photogrammetric data, four 8-inch diameter aluminum disks with painted crosshair targets were used as known reference points within the LiDAR data. The profile extracted from the point clouds (which were generated from both TLS and cameras using a structure from motion, or SfM), was used to obtain the vertical settlement of the wall. SRW movements can be evaluated by comparing the alignment at different times. They relied on measuring the natural reference targets in each mission, which could be inconsistent as a result of human error; therefore, their approach may lead to inaccurate registration, resulting in less-reliable estimation of vertical settlements and lateral deformations. Also, their use of artificial reference points in processing photogrammetric data can result in more complicated - and sometimes unreliable - matching procedures. Oskouie et al. (2016) proposed a retaining wall displacement measurement technique utilizing TLS to acquire point clouds to derive some performance measures for monitoring a retaining walls. In their study, the horizontal joints between highway retaining wall panels, extracted from laser scanning data using a feature extraction algorithm (e.g., a RANSAC-based strategy), were used as benchmarks to measure the displacement of panels. The accuracy in their method depends upon the accuracy of the registration technique. The registration technique is based on multiple common reference points. These points should not be removed or occluded during the operation; however, this may not be guaranteed (and may even be unavoidable) because of construction conditions. In the second operation, again, the reference points must be placed on the same position; however, this may not be possible due to human error. Finally, the gap distance between the joints (from two profiles collected at different times) is reported. Furthermore, for the validation of the proposed method, simulated scan datasets were generated for 540 scenarios through a simulation environment. Their simulation results showed that wall displacements could be measured with an average error of 0.9 mm. Lin et al. (2019) utilized TLS to derive the standard longitudinal and transversal angular distortions. They also derived new measures which represent the out-of-plane displacements and angular tilts of panels relative to the individual faces of an MSE wall. For derivation of the standard and new performance measures, they further defined coordinate systems for the individual faces and panels, which are denoted as the leveled face (LF_{cs}) and panel (P_{cs}) coordinate systems, respectively. More specifically, LF_{cs} is defined with its X-axis aligned along the MSE wall and parallel to the local horizontal plane of the MSE wall location. The Y-axis is aligned along the local plumb-line. Finally, the Z-axis defines a right-handed coordinate system. The P_{cs}, on the other hand, is defined through the panel segmentation and minimum bounding rectangle (MBR) procedures. More specifically, the individual panels are derived through a region segmentation procedure where the normal distance between the points along the face (from the best fitting plane through these points) is used as the segmentation criterion. The lower and left sides of the MBR (enclosing the segmented panels and the panels' surfaces) normally are used to define the Pcs. In Lin et al. (2019), their approach was limited to smooth MSE walls and has not been tested for different kind of MSE walls such textured MSE walls. Lienhart et al. (2018) presented a practical approach for large-scale monitoring of retaining walls along Austrian highways using a Mobile Mapping System (MMS) as shown in Figure 2.13. The measurement platform consisted of two laser scan profilers, inertial measurement unit (IMU), differential Global Navigation Satellite System (GNSS) receiver, and multiple cameras. The cameras are utilized to provide true colors for the point clouds. The aligned point clouds from different sensors were used to generate vertical profiles every 5 cm along the retaining wall by intersecting the wall surface model with planes orthogonal to the vehicle's trajectory (see Figure 2.14). A fitted regression along the vertical profile is then used to derive the tilt angle. They found that it is possible to determine the tilt angle with an accuracy better than 0.1°. However, their approach is limited to evaluating the transversal out-of-plane angle of the retaining wall, which is identical to the AASHTO-based transversal angular distortion (α_T).

Figure 2.13 Mobile mapping system configuration (Lienhart et al. (2018))

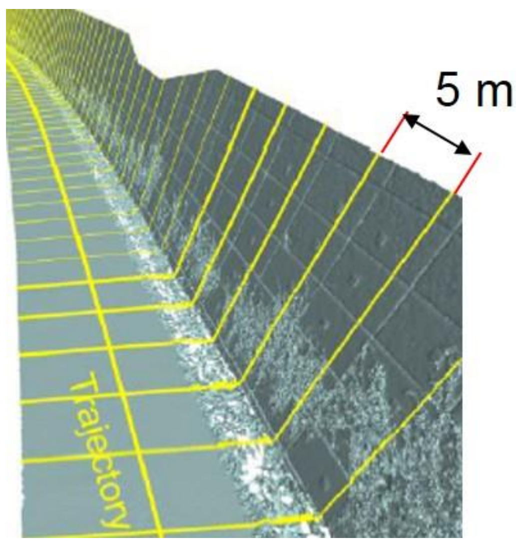

Figure 2.14 The car trajectory and the vertical profiles every 5 meter are indicated as yellow lines (Lienhart et al. (2018))

Photogrammetric (Digital Camera Sensor) Method

In addition to non-contact sensors, recent advancements in lower-cost optical cameras, image processing, and 3D modeling have enabled photogrammetry to three-dimensionally reconstruct objects from digital images for civil engineering applications (Jiang et al. 2015; Cleveland, 2006; and Wartman, 2006). Photogrammetry provides the ability to obtain quantitative measurements from 3D models created from quality easily documented two-dimensional (2D) images and has been used for assessing the condition of transportation assets. Research has been documented where photogrammetry or Structure from Motion (SfM) techniques were applied for 3D reconstruction for civil infrastructure systems (Scaioni et al., 2014 and Wei, et al., 2013). Detchev et al. (2013) demonstrated a digital photogrammetric system for both static and dynamic load test measurement, for which their experiments were conducted concurrently. The low acquisition rate of their cameras limited the loading frequency that could be measured to 1 Hz, whereas 3 Hz is normally required. Oats et al. (2019) utilized photogrammetry point cloud data to measure the failure mode behavior of a retaining wall model, emphasizing further robust spatial testing. They compared two commonly used photogrammetry software packages to assess the computing performance of their method and the significance of the control points in their approach. Their measure was the displacement changes along the surface of a retaining wall. Fourteen reference control points were placed in the test setup to infer ground location for georeferencing (see Figure 2.15). Ten of these control points were placed on the individual retaining wall panels (five on each panel), and the remaining four were placed on neighboring stationary objects positioned at different elevations and depths from the wall model. The stationary control points, those placed on static surfaces, assisted in the co-registration of the point clouds in a common coordinate system for the different scenarios. The displacements were calculated by comparing the positions of the control points along the surfaces of the retaining wall over time.

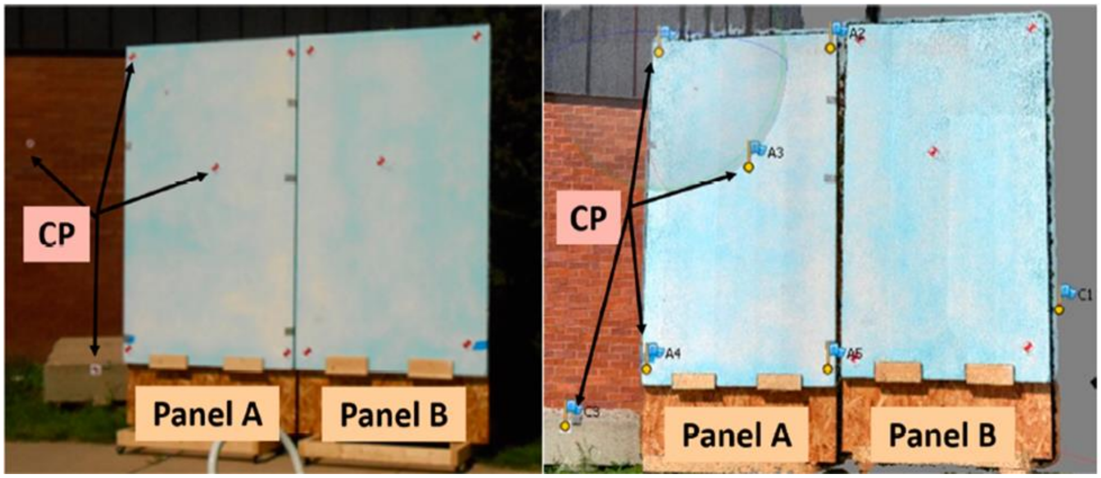

Figure 2.15. Configuration of the data collection and reconstruction point cloud (Oats et al. (2019))

2.4 Shortcomings/Drawbacks of Reviewed Literature

As shown in the literature review, most of the existing approaches for deformation measurement and monitoring rely on an extensive number of physical targets. Some approaches use natural features. The difficulty in measuring displacement is finding a spatial measurement technique that possesses desirable properties such as precision, reliability, low cost, and ease of use. Some advantages can be seen in a number of methods, but it is difficult to find a method that offers all of them. Also apparent from the reviewed literature is that TLS is frequently the preferred sensor for infrastructure monitoring. In processing data, TLS relies on commercial software to evaluate vertical settlement as well as lateral deformation of MSE walls. Such commercial software usually increases the costs substantially (a few thousand dollars or more). There are shortcomings and drawbacks identified within the reviewed literature for each approach, which are briefly explained in the next two paragraphs.

Geotechnical Devices: Although geotechnical instrumentation is accurate in determining MSE wall deformation (movement in lateral and/or vertical directions) and can collect samples at very high frequency, it is usually installed and affixed on-site, requiring additional effort. The accuracy and reliability of the measured position or displacement profile is dependent on the quality of the casing, probe, cable, readout, and accessories selected. A poorly engineered probe, stretchy cable, faulty readout, or inferior casing will result in poor quality data and an unhappy user. The stability of geotechnical instruments is subject to external movements due to site conditions; and its stability must be verified throughout the data collection time in order to avoid erroneous measurements. Moreover, instruments used to measure MSE wall deformation are usually installed in specific locations of a construction site. These locations are determined, based on the site conditions, to avoid potential conflicts; therefore, the collected data are limited to those selected sections of the project. Another downside of these instruments is that they can only perform measurements in one direction capably (e.g., one dimension) with high geometric precision and reliability. If simultaneous 2D or 3D measurement at several locations is required, the instrumental effort becomes rather large. The techniques generally are not suited for tasks requiring large numbers of measurement points distributed over an object surface or for complete surface measurements.

Another practical disadvantage of these instruments is the possibility of damage to the sensors themselves because they are fragile and are installed on - or in very close proximity to - the structures being monitored (e.g., contact sensors). Other disadvantages include electromagnetic interference, signal loss over long distances during transmission, gravity dependence, and poor durability. These factors can act as obstacles during horizontal and vertical deformation monitoring when using transitional sensors.

Surveying Devices: On the other hand, optical surveying of point targets using total stations is labor-intensive and time-consuming, and the data are limited to the surveyed targets. Therefore, the process is not optimal for data collection of a wall of large length and height as scanning all the points on a wall is not practical. For TLS, the previous research in the literature focused on deriving standard measures. It uses reference points to register multiple scans in a common reference frame. This approach may lead to inaccurate registration, resulting in less-reliable estimation of vertical settlements and lateral deformations in such approaches. Moreover, manual processes are embedded in the work in order to extract a portion of the data. As far as camera sensors, their ability to cover a large-scale object requires more effort. In addition, the need of for control points is time-consuming to place them on the object and risky to perform. Collecting the images using a photogrammetric system outdoors in harsh conditions also is not practical. Besides the previous disadvantages, the point cloud after 3D reconstruction from the photogrammetric system can be sparse, which can prevent extracting useful information.

In order to mitigate the limitations of traditional instruments such as those mentioned above, photogrammetric and LiDAR-based (e.g., static-based and/or mobile-based) remote sensing techniques can be conducted for MSE wall monitoring purposes. These techniques are capable of directly reconstructing entire 3D surfaces without the need to access the monitored object(s). This capability can be used for performing displacement measurements (e.g., vertical and/or lateral displacements). In addition, a permanent visual record is established for each observed epoch. This permanent record can be used to identify and characterize the positions of each panel of the MSE wall over time. Therefore, accurate study and prediction of deformation behavior require data points throughout MSE walls. There is a need for a high-speed and comprehensive collection of data as well as a method for measuring the displacements of MSE walls with an improved accuracy compared to the conventional methods.

2.5 Chapter summary

This chapter provided an extensive review of the literature on traditional and remote sensing techniques for infrastructural monitoring. In addition, the traditional surveying and remote sensing methods for deformation measurements also were reviewed as well as the drawbacks of the various methods. Chapter 3 and chapter 4 present the system design as well as the methodologies for deriving both standard and new-available performance measures. These methodologies then are used to monitor infrastructure components, specifically textured and smooth MSE walls.

In summary, the monitoring strategy should also consider factors that would affect the practical implementation and scalability of such an approach. Total station, geotechnical field instrumentations, and/or TLS are the most commonly used data acquisition systems for the derivation of the serviceability measures. However, such instruments require access to the MSE wall site and this could subject the inspectors to risky conditions as a result of incoming traffic. In addition, field data collection is time consuming; thus, making the monitoring process non-scalable. The third challenge, which should be addressed by a monitoring strategy, is its capability to deal with both smooth and textured MSE walls that could be straight or curved (i.e., the MSE wall is comprised of a set of individual planar faces). Prior research (e.g., Lin *et al.,* 2019) has mainly dealt with planar MSE walls with smooth panels.

3. SCALABLE MONITORING OF MSE WALLS WITH SMOOTH PRECAST CONCRETE PANELS USING MOBILE LIDAR

This chapter was originally submitted in the journal of surveying engineering: Aldosari, M., Al-Rawabdeh, A., Bullock, D., & Habib, A. (2020). Scalable monitoring of MSE walls with smooth precast concrete panels using mobile LiDAR.

3.1 Abstract

Mechanically stabilized earth (MSE) walls rely on self-weight to resist the destabilizing earth forces acting at the back of the reinforced soil area. MSE walls are a common infrastructure along transportation corridors within the U.S. as well as other countries since they are low-cost and have easy-to-install precast concrete panels. The usability of such transportation corridors depends on the safety and condition of the MSE wall system. Consequently, MSE walls need to be periodically monitored according to prevailing transportation asset management criteria during the construction and serviceability life stages to ensure that their expected performance measures are met. To date, MSE walls are monitored using qualitative approaches (e.g., visual inspection or examination), which provide limited information. Aside from being time-consuming, visual inspection are susceptible to bias due to human subjectivity. Current alternative monitoring approaches are based on using a total station, geotechnical field instrumentation, and/or static terrestrial laser scanning (TLS). These instruments can provide highly accurate and reliable performance measures; however, their underlying data acquisition and processing strategies are also time-consuming and not scalable. This paper presents a study that aimed to develop a comprehensive strategy using a mobile LiDAR mapping system (MLS) for the acquisition and processing of point clouds covering the MSE wall. The proposed strategy provides several global and local serviceability measures for MSE walls with smooth panels. Also, to efficiently obtain reliable data conducive to the development of these serviceability measures, an ultra-high-accuracy wheel-based LiDAR data acquisition system was developed for that purpose. A case study was conducted to illustrate the feasibility of the proposed acquisition/processing strategy while focusing on the comparative performance of TLS and MLS in terms of the agreement of the derived serviceability measures. The results of that comparison show that the MLS-based serviceability measures were within 1 cm and 0.3° of those obtained using TLS and thus confirmed the potential for using MLS to efficiently acquire point clouds, while facilitating economical, scalable, and reliable monitoring of MSE walls.

Keywords: Smooth MSE walls; mobile LiDAR mapping systems (MLS); static terrestrial laser scanning (TLS); performance/serviceability measures; civil infrastructure; segmentation; characterization.

3.2 Introduction

Mechanically stabilized earth (MSE) walls are used extensively to resist destabilizing earth forces acting at the back of the reinforced soil area (Oskouie et al., 2016). MSE walls are low-cost and have easy-to-install precast concrete panels. MSE walls are a common infrastructure along transportation corridors within the U.S. as well as other countries due to these characteristics. For example, there are roughly 1,200 to 1,500 MSE walls in the state of Indiana, USA, excluding those on local public agency (LPA) routes (Rearick and Khan, 2017). An MSE wall is composed of several parts, including a façade made of precast concrete panels, which are supported by many compacted backfill layers strengthened with geosynthetic or metallic reinforcement (Passe, 2000). Modular facing blocks, which can be smooth or textured (i.e., with several architectural and aesthetically pleasing finishes) constitute the façade of an MSE wall (McGuire et al. 2017; Lin et al. 2019). The key function of these facing panels is to prevent backfill soil material from leaking out of the panel joints while allowing excess water to seep through them. Failure of an MSE wall can result not only in infrastructure damage, which is associated with a high price tag, but can also result in the tragic loss of life. Therefore, an accurate yet scalable inspection methodology is important.

The long-term performance of an MSE wall relies on a well-designed and constructed system that meets the specifications provided by regulatory organizations, such as the U.S. Department of Transportation (DOT). The longitudinal angular distortion (α_L) and the transversal angular distortion (α_T), which have been proposed by the American Association of State Highway and Transportation Officials (AASHTO), is a commonly accepted set of serviceability measures (AASHTO, 2014). The longitudinal angular distortion (α_L) is defined as the ratio of the differential settlement between two points along the length of the MSE wall to the horizontal distance between them. The transversal angular distortion (α_T) is the lateral deflection (i.e., out of the wall plane) of the MSE wall divided by its height. These angular distortions can be calculated at any time during an MSE wall's service life.

Table 1 provides the tolerable α_L values for MSE walls constructed of incremental precast concrete panels with different joint widths. During the construction of an MSE wall with incremental precast concrete panels, the tolerable α_T values, when measured with a 3.048 m (10 ft) straight edge should be less than 1/160. At the end of the MSE wall construction process, α_T should be less than 1/240 when measured using a plumb line dropped from the top of the constructed wall (AASHTO, 2014). In addition to the angular distortions, the U.S. Federal Highway Administration (FHWA) also provides guidelines for tolerable out-of-plane offsets between neighboring panels (FHWA, 2009). According to these guidelines, the out-of-plane offset at any joint should be less than 9.53 mm (3/8 in) during wall construction. The standard serviceability measures, excluding the out-of-plane offset, are global measures that focus on the vertical settlement and lateral deflection of an MSE wall. However, most MSE wall failures are related to local deformations, such as a relative angular tilt and displacement among neighboring panels, as shown in Figure 3.1. Therefore, reliable monitoring should be capable of providing measures that evaluate the deformation behavior of the individual panels within an MSE wall. Examples of such measures include those proposed by Lin et al. (2019).

Table 3.1 Tolerable longitudinal angular distortion (α_L) values for MSE walls constructed with incremental precast concrete panels (modified from (AASHTO, 2014))

Joint width w_J	**Panel area ≤ 2.8 m² (30 ft²)**	**2.8 m² (30 ft²) < Panel area ≤ 7 m² (75ft²)**
19 mm (0.75 inch)	$\alpha_{L,tol}$ = 1/100 = 0.01	$\alpha_{L,tol}$ = 1/200 = 0.005
13 mm (0.50 inch)	$\alpha_{L,tol}$ = 1/200 = 0.005	$\alpha_{L,tol}$ = 1/300 = 0.003
6 mm (0.25 inch)	$\alpha_{L,tol}$ = 1/300 = 0.003	$\alpha_{L,tol}$ = 1/600 = 0.002

(a)

(b)

Figure 3.1. An example of (a) an MSE wall failure that could have started with (b) an excessive angular deformation (bulging) between neighboring panels

The monitoring approach should also consider the factors that would affect the practical implementation and scalability of the strategy. The most commonly used data acquisition systems for the derivation of serviceability measures are traditional surveying instruments, such as a total station; geotechnical field instrumentation, such as an inclinometer; and/or static terrestrial laser scanning (TLS). The use of such instruments is time-consuming and requires access to the MSE wall site. Moreover, adopting such technologies can expose inspectors to dangerous conditions as a result of continuous traffic flow. A reliable monitoring strategy needs to address these concerns and also should be able to handle MSE walls that are straight or curved (i.e., an MSE wall is composed of a set of individual planar faces as shown in Figure 3.2(a) or a single curved façade, which could be considered as piece-wise planar, as shown in Figure 3.2(b)). Previous research (e.g., Lin et al., 2019) addressed only planar MSE walls with smooth panels (Figure 3.2 (a)); so, the development of a methodology that addresses all types of MSE walls would be an innovative contribution as well. In response to the abovementioned challenges for monitoring MSE walls, the study presented in this paper aims to achieve the following three objectives:

1. Develop a monitoring strategy that could be used for the delivery of both standard and recently available serviceability measures.
2. Provide a reliable, scalable monitoring strategy using mobile LiDAR.
3. Introduce a methodology that can support MSE walls with smooth precast concrete panels along either planar or piece-wise planar façades.

The remainder of this paper will proceed as follows. Section 3.3 briefly discusses the existing MSE wall monitoring strategies with an emphasis on those utilizing LiDAR point clouds. Section 3.4 introduces the mobile LiDAR mapping system (MLS) data acquisition unit specifically developed in this study to address the research objectives. In addition, Section 3.4 describes the data acquisition for the case study conducted to illustrate the comparative performance of MLS and TLS. The proposed methodology in then presented in Section 3.5. Section 3.6 discusses the results from the data processing strategy for the case study. Finally, Section 3.7 presents the conclusions and recommendations for future work.

(a)

(b)

Figure 3.2.Two types of MSE walls: (a) Multi-face planar MSE wall and (b) Curved MSE wall with a piece-wise planar face

3.3 Related Work

Visual inspections/examinations using a variety of instruments, such as measuring tapes and plumb lines, are commonly used as MSE wall monitoring techniques. However, these techniques can lead to inconsistencies due to human subjectivity (Oats et al., 2017). Other methods for evaluating some serviceability measures for MSE walls with precast concrete panels include the use of a total station or TLS. Laefer and Lennon (2008) proposed an approach for monitoring retaining walls using TLS whereby multiple temporal scans are collected and processed to detect any movements of the vertically stacked panels within the MSE wall. Each scan must include a minimum of three spherical static targets, which then are used as reference points for the registration/alignment of the captured scans. The authors recommended that the targets remain on-site for the duration of the monitoring process. Oskouie et al. (2016) utilized TLS to acquire point clouds and derive performance measures for MSE walls. In their research, the point cloud data first was cleaned by eliminating unwanted objects, such as temporary steel and wooden brackets. Then, a planar model was fitted through the wall using the random sample consensus (RANSAC) algorithm (Fischler and Bolles 1981). The authors considered the vertical/horizontal joints as outliers when inspecting the normal distances relative to the fitted wall-plane surface and the joint distances are reported as a serviceability measure. Lienhart et al. (2018) presented a practical approach for large-scale monitoring of retaining walls along Austrian highways using a mobile mapping system (MMS) with a measurement platform composed of two laser scan profilers, an inertial measurement unit (IMU), a differential global navigation satellite system (GNSS) receiver, and multiple cameras that provided true colors for the acquired point clouds. The point clouds captured by the two sensors were used to generate vertical profiles every 5 cm along the retaining wall by intersecting the wall surface model with planes orthogonal to the vehicle's trajectory. They then used fitted regression along the vertical profile to derive the tilt angle of the MSE wall façade and found that it was possible to determine the tilt angle with an accuracy better than 0.1°. Their approach was limited to evaluating the transversal out-of-plane angle of the retaining wall, which is similar to the AASHTO-based transversal angular distortion (α_T). Lin et al. (2019) utilized TLS to derive the standard measures (i.e., longitudinal and transversal angular distortions) of MSE walls with smooth panels. In their work, they also derived new measures that represent the out-of-plane angular tilts and displacements of the panels relative to the individual MSE wall faces. For derivation of the standard and new performance measures, Lin et al. (2019) defined two coordinate systems for the individual faces and panels, denoted as the Levelled Face (LF_{cs}) and Panel (P_{cs}) coordinate systems, respectively. The LF_{cs} was derived using a plane fitting through a manually cropped face of an MSE wall and considering the local horizontal/vertical directions within the site. The P_{cs}, however, began with the identification of the individual panels through a region segmentation procedure where the local point spacing and normal distances between the points along the face and the best fitting plane through these points were used as the segmentation criteria. Following the panel segmentation, P_{cs} was defined through its bounding box (i.e., the minimum bounding rectangle –MBR (Freeman and Shapira, 1975). The new serviceability measures developed in their work were based on the spatial and rotational relationships between the LF_{cs} and P_{cs}.

Although TLS is an effective tool for monitoring MSE walls that has been shown to provide highly accurate and reliable serviceability measures, it is a time-consuming process that affects traffic flow during data acquisition, and it also has not been fully tested on large MSE walls. The monitoring strategy proposed in this paper therefore is based on the use of an MLS, which collects highly accurate, high-resolution point clouds while driving along the transportation corridor.

3.4 Acquisition System Specification and Configuration of the Case Study

The essential objective of this study was to demonstrate the feasibility of using a wheel-based MLS for point cloud acquisition to obtain a wide range of MSE wall serviceability measures. An in-house-developed MLS, which is shown in Figure 3.3, was used for the case study conducted. The MLS has two high-grade laser scanners (Riegl VUX-1HA and ZF Profiler 9012) as well as two rear-facing FLIR Flea2 5.0MP cameras. Each laser scanner has a single laser beam and delivers a 360^{o} horizontal field of view. The Riegl VUX-1HA and ZF Profiler 9012 can capture roughly one million points per second each and operate within a range of 150 m (at an accuracy of ±5 mm) and 120 m (at an accuracy of ±2 mm), respectively (Riegl, 2018; ZF, 2018). Derivation of the ranging data requires geo-referencing the mapping platform, which entails determination of the position and orientation of the individual sensors relative to a user-defined coordinate system. The MLS onboard sensors are directly geo-referenced by a NovAtel ProPak6 GNSS receiver and ISA-100C near-navigation grade IMU. The Inertial Explorer Differential GNSS Inertial post-processing software from NovAtel is used for the integration of the raw GNSS/INS data. The accuracy of the derived GNSS/INS attitude after post-processing is 0.003° for the pitch/roll and 0.004° for the heading (yaw), and the range of the positional accuracy is 0.01 to 0.02 m (NovAtel, 2019). A rigorous system calibration procedure (Ravi et al., 2018) was used for the estimation of the spatial and rotational offsets (i.e., the mounting parameters) between the GNSS/INS and laser scanning units. The the system calibration parameters were estimated by minimizing the discrepancies between conjugate points, linear features, and planar features captured from different scanners in different drive runs.

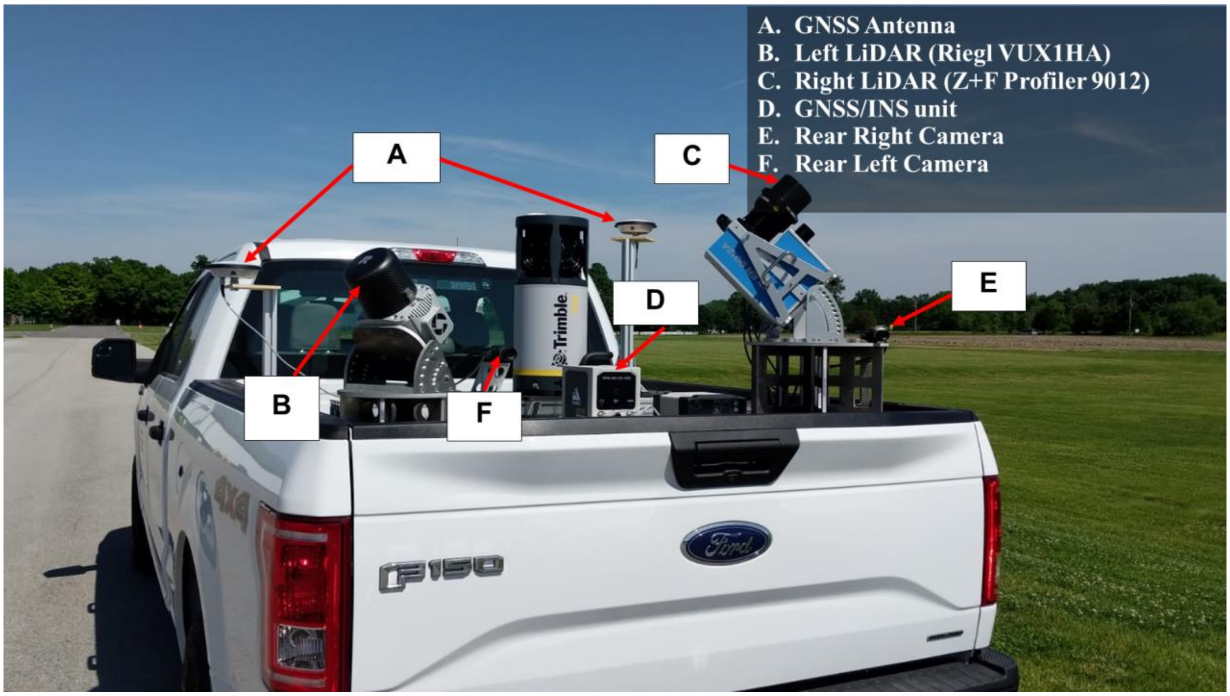

Figure 3.3. Configuration of the wheel-based mobile LiDAR mapping system used for the acquisition of point clouds along MSE walls

A smooth MSE wall in the U.S. state of Indiana was selected for a case study to illustrate the capability of the developed MLS and proposed processing strategy for deriving both standard (longitudinal and transversal angular distortions) and recently available performance measures introduced by Lin et al. (2019). The case study was conducted to evaluate the overall capability of mobile LiDAR in examining the MSE wall by comparing its derived measures to those based on TLS. For the TLS data acquisition process, a Faro Focus x330 with a range accuracy of ±2 mm at an object distance of 25 m was used (FARO, 2013). This scanner has a maximum range of 330 m while emitting close to one million pulses per second and provided color-coded point clouds using a built-in camera. At a given location, the TLS performed two consecutive scans, with the first scan dedicated to acquiring the 3D point cloud while the second one captured successive images that were used for colorizing the individual points. Figure 3.4 depicts a portion of the MSE wall that had piece-wise planar façades (i.e., the façades cannot be modeled as a single planar surface).

The MSE wall at the site was built in 2014 and consists of 11 piece-wise planar faces along six façades (see Figure 3.5). The total length of the MSE wall is approximately 345 m (along the six façades) with an average height of 7 m. This study focuses on approximately 160 panels (i.e., fully covered and not occluded) of the MSE wall that constitute façades 1,2, and 5 (façades 3,4, and 6 are excluded as they are out of the range of the LiDAR units). The panels dimension are approximately 1.5 m by 3 m in size. The width of the joints for the size of the facing panels used in this wall is 19 mm (0.75 in.), as prescribed in the Indiana Department of Transportation standard specifications (Indiana Department of Transportation Standard Specifications 2016). To obtain complete coverage of the MSE wall and to mitigate any occlusions caused by vegetation and/or road features (e.g., light poles and signs), three TLS scans were collected. The MLS system conducted four drive runs in opposite directions at an average driving speed of 15 mph, as shown in Figure 3.5. Each drive run was finished in less than 30 seconds. A sample of the collected MLS point cloud is shown in Figure 3.6.

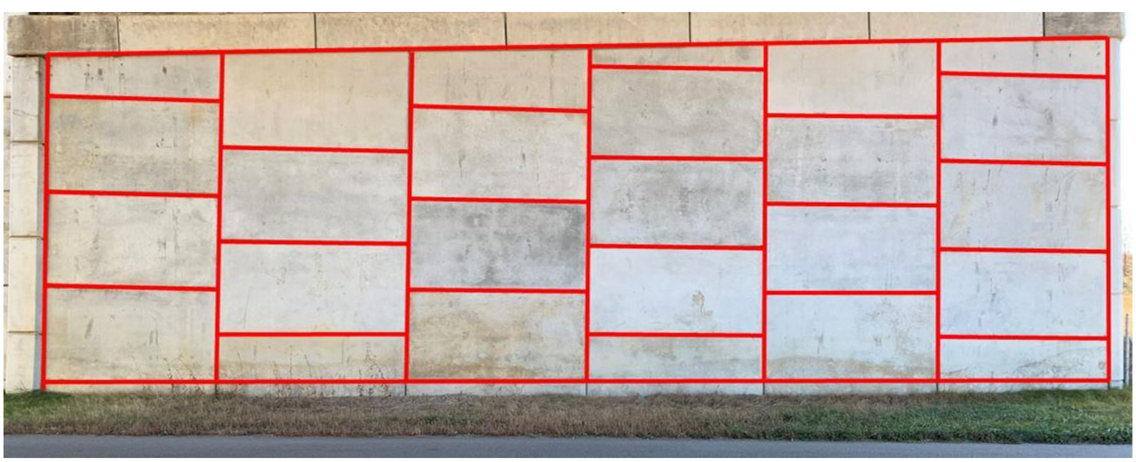

Figure 3.4. Sample photo of a portion of the MSE wall with smooth panels (the different tiles are highlighted by the red rectangles)

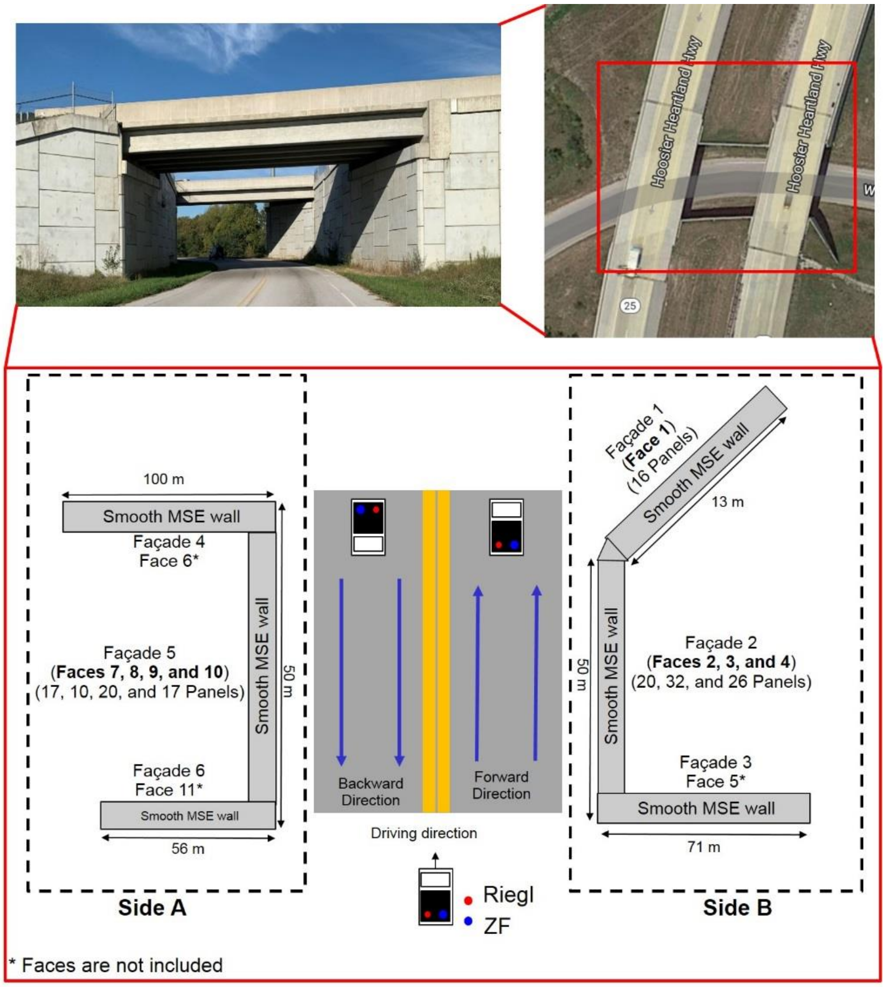

Figure 3.5 Location and drive runs configuration for the dataset collection at the site

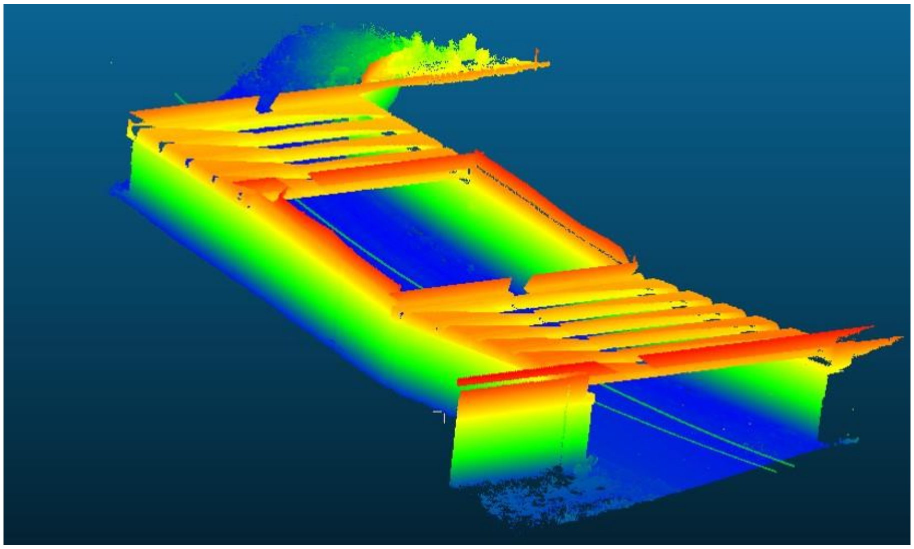

Figure 3.6 Point cloud at the MSE wall site location collected by the MLS (colored by height)

3.5 Methodology

3.5.1 Conceptual basis of the proposed methodology

A flowchart of the proposed procedure – which is comprised of data acquisition, data processing, and estimation of the performance/serviceability measures – for the scalable, systematic approach developed in this study is shown in Figure 3.7. The standard serviceability measures, as specified by AASHTO (2014), evaluate the longitudinal and transversal angular distortions of a given MSE wall face. The newly developed serviceability measures by Lin et al. (2019) provided the relative displacement and rotation of the individual panels relative to a Levelled Face coordinate system (LF_{cs}).

In order to derive the serviceability measures, the point clouds captured from the different MLS drive runs should be registered to a common reference frame even though, theoretically, registration is not necessary for point clouds acquired by an MLS since they are directly georeferenced through the onboard GNSS/INS unit. The GNSS/INS trajectory, when combined with the system calibration parameters, produces the position and orientation of the laser scanners relative to the mapping frame (e.g., the UTM coordinate system with the WGS84 as the datum for the horizontal coordinates and the National American Vertical Datum of 1988 – NAVD 88 – for the vertical coordinates). Therefore, the collected point clouds from the different drive runs should be properly aligned, provided there is reliable trajectory data and accurate system calibration parameters are available. However, issues related to canopy cover, obstructions (e.g., tunnels and/or overhead bridges), GNSS-signal multipath interference from neighboring traffic, and platform speed can compromise the GNSS/INS trajectory, which can lead to alignment discrepancies between overlapping point clouds from neighboring drive runs. To take advantage of the available/complementary point cloud data from multiple drive runs, alignment must be ensured. In general, registration strategies can be categorized into coarse and fine approaches (Al-Durgham and Habib, 2013; Al-Rawabdeh et al., 2017). Since this study primarily utilized MLS point cloud data, which is aligned to a high degree by the onboard GNSS/INS unit, its focus was fine registration. The point cloud fine registration strategy adopted in this study is discussed in more detail in Section 3.5.2.

The identification of individual planar segments of the wall (denoted hereafter as faces) is derived once the point clouds of the MSE wall have been accurately registered. If an MSE wall is multi-face with individual planar faces, as shown in Figure 3.2(a), or a piece-wise planar façade, as shown in Figure 3.2(b), it needs to be partitioned into sections that are believed to be perfectly planar. In this study, the MSE wall faces were manually identified and partitioned. The criterion for the fine-tuning of the partitioning process was based on the root mean square error (RMSE) of the normal distances between the constituent points from the corresponding best-fitting plane for the MSE wall face.

The next step is to define the coordinate systems associated with the MSE wall face (LF_{cs}) as well as the individual panels (P_{cs}). These coordinate systems are essential for determining the standard and new serviceability measures. The LF_{cs} is defined by the local horizontal/vertical directions at the MSE wall site as well as the best-fitting plane through the face in question, as depicted inFigure 3.8. The Y-axis of the LF_{cs} is defined in a way that it belongs to the MSE wall face (as defined by the fitted plane parameters) and is parallel to the horizontal plane, as described by the XY-plane of the defined mapping coordinate system at the site location. The Z-axis of the LF_{cs} is aligned along the plumb line at the MSE wall site. Finally, the X-axis of the LF_{cs} is derived to define a right-handed coordinate system. To facilitate the definition of the LF_{cs}, the geo-referencing parameters from the MLS are established in a local mapping coordinate system wherein the Z-axis points in the local level (plumb line) direction at the MSE wall site location. The P_{cs} is essential for evaluating the relative displacement between the panels as well as the relative displacement/rotation between the panels and the LF_{cs}. As shown inFigure 3.8, the panel coordinate system is defined with Y and Z axes aligned along the bottom and left sides of the bounding rectangle enclosing the panel. The X-axis of the panel coordinate system is derived to define a right-handed coordinate system (i.e., it is defined by the normal to the panel surface). A key component for reliable derivation of the serviceability measures is ensuring that the P_{cs} is defined in an identical manner for all the panels in a given face. To isolate the points making up the individual panels and to define the panel coordinate systems, this study adopted a region-growing segmentation procedure, which utilizes the local point spacing (LPS) and normal distance (n_d) from the best-fitting plane to the MSE wall face as the similarity criteria. The underlying assumption for such segmentation is that excessive normal distances from the best-fitting plane correspond to the joints separating the individual panels. Finally, after the coordinate systems are established and the individual panels are extracted, the performance measures can be derived. The definition and derivation of the standard and recently available performance measures for smooth MSE walls are presented in Section 3.5.4.

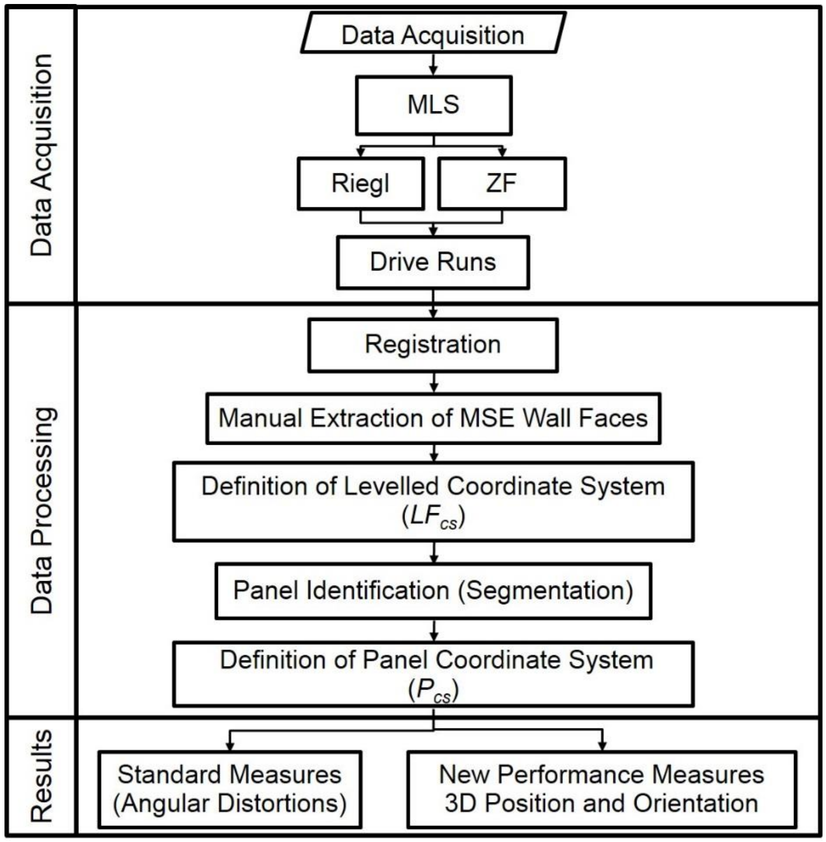

Figure 3.7. Flowchart of the proposed methodology

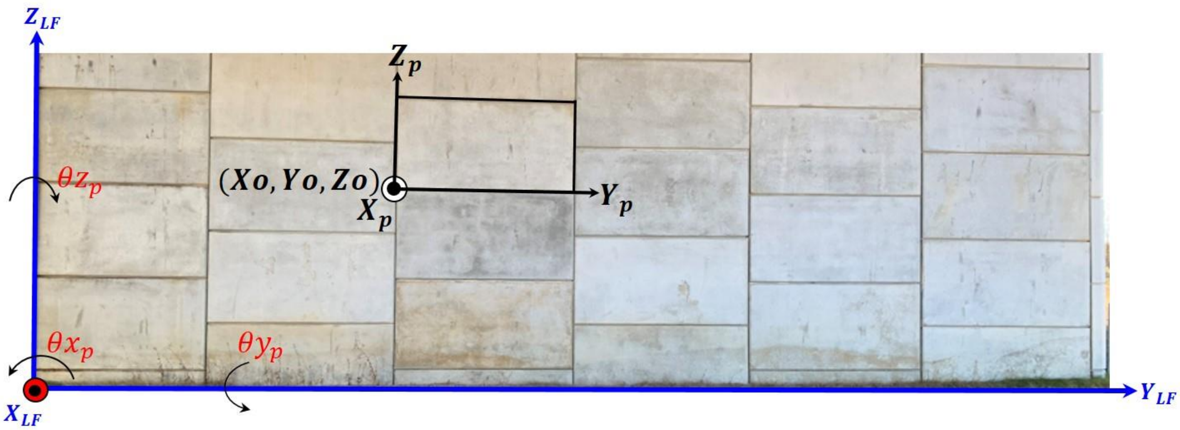

Figure 3.8. Illustration of the Levelled Face coordinate system (LF_{cs}) and Panel coordinate system (P_{cs})

3.5.2 Registration of point clouds from different MLS drive runs and TLS scans

A wide range of point cloud registration procedures have been proposed in the past few years to ensure accurate registration of LiDAR point clouds captured from different MLS drive runs. According to Habib and Al-Ruzouq (2004), a comprehensive registration paradigm should address four criteria: (1) the transformation parameters relating the reference frames of the involved datasets, (2) the registration primitives used for the estimation of the transformation parameters, (3) the mathematical constraints describing the similarity metric between conjugate primitives after registration, and (4) the matching strategy for the automated identification of conjugate primitives. Due to the short acquisition duration of the point cloud data from different drive runs (less than 30 seconds), a six-parameter transformation (three shifts and three rotation angles denoted as X_T , Y_T , Z_T , Ω , Φ , and K, respectively) would be sufficient for relating the reference frames of the point clouds from the different drive runs. For fine registration, point primitives are recommended due to the huge redundancy supplied by the size of the point cloud, which would ensure the highest accuracy possible for the estimated transformation parameters even though a point-to-point correspondence cannot be guaranteed in the data from different drive runs. The similarity metric is based on constraining the distance between a point in one drive run and its corresponding point in another drive run (the latter is established by the matching strategy after the application of the transformation parameters) to be zero. Addressing the matching strategy is the final task in the alignment process. The well-known iterative closest point (ICP) algorithm (Besl and McKay, 1992) establishes matches through the iterative minimization of the squared sum of the point-to-point distances in the overlapping area between the different drive runs. An alternative strategy was proposed by Grant et al. (2012) to avoid the underlying assumption of the ICP– i.e., point-to-point correspondence in overlapping point clouds–, where the estimation of the transformation parameters is based on a point-to-plane minimization metric. The key limitation of this strategy is its computational inefficiency. The iterative closest patch (ICPatch) algorithm (Habib et al. 2010), which is a variant of ICP, is a better matching strategy because it avoids the underlying assumption of having point-to-point correspondences. Within ICPatch, the points in a drive run are matched to triangular patches in another drive run, which are derived through a triangular irregular network (TIN) procedure. The matching strategy identifies point-patch pairs through the iterative minimization of the squared sum of the normal distances between such pairs. To avoid the TIN generation procedure, which can handle only surfaces with predominantly mild slopes, the iterative closest projected point (ICPP) algorithm was developed (Al-Durgham and Habib 2013). In this case, the patch is defined by the closest three points in the second drive run to a transformed point from the first one using the current estimate of the transformation parameters.

In the study presented in this paper, a modified matching strategy, which is a hybrid implementation of ICPatch and ICPP, was utilized. An approximate estimate of the transformation parameters between the captured point clouds from different drive runs is established. Given that these point clouds are aligned to a high degree through the onboard GNSS/INS, zero shifts and zero rotation angles can be used as the initial values for the transformation parameters. These parameters are used to transform a point from one drive run, which will be denoted as the source surface, to the reference frame of the other drive run, which will be denoted as the reference surface. The transformed point (P_t) is then used to identify the three closest points in the reference surface. The closest three points are accepted as a possible match if (P_t) belongs to a bipyramid formed by these points and two vertices that belong to the orthogonal to the triangle, which is defined by these three points through their centroid given a predefined normal distance threshold (Figure 3.9). The normal distance threshold (n) is selected based on the noise level within the data. Rather than minimizing the squared sum of the distances between the transformed point and its projection onto the corresponding triangle (which is implemented in ICPP), this study utilized the modified weigh function proposed by ICPatch for the estimation process. For more details regarding the modified weight function, interested readers can refer to (Habib et al. 2010).

Compared to the original ICPatch and ICPP, the advantages of the hybrid approach include a higher computational efficiency, less sensitivity to the existence of erroneous points (i.e., outliers), and capability of registering vertical surfaces, which cannot be effectively handled in the original ICPatch. An example of the outcomes from the point cloud registration are shown in Figure 3.9, where three TLS scans are registered together with the MLS point clouds from different drive runs.

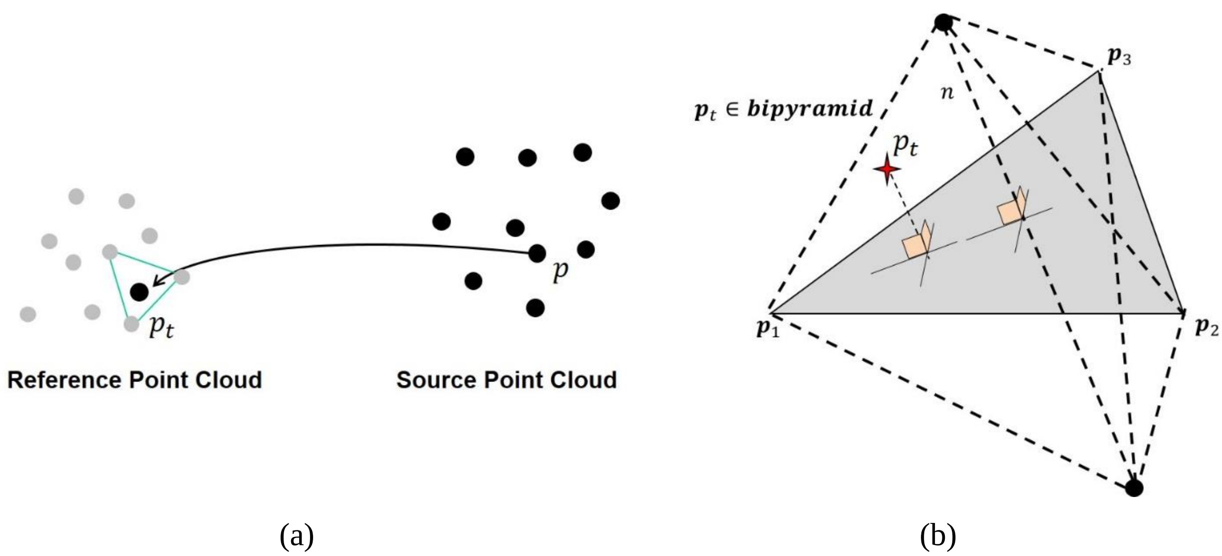

Figure 3.9. (a) Transformation from source point cloud to reference point cloud, and (b) conditions to accept the point-to-patch correspondence between the two point clouds.

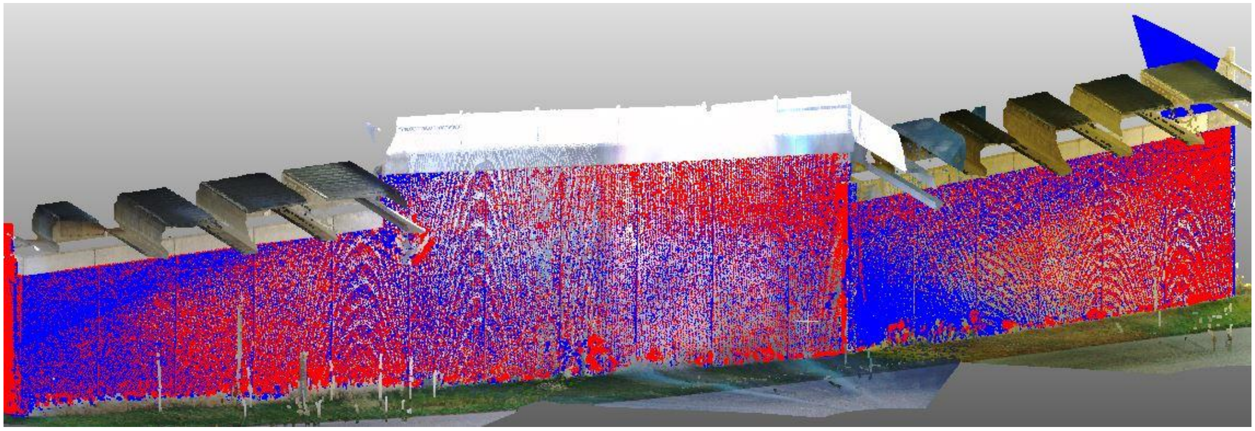

Figure 3.10. Point cloud registration of TLS dataset at the site (colored by the RGB values from the TLS camera) and the MLS dataset (colored by drive runs)

3.5.3 MSE wall face and panel identification

A semi-automated procedure is developed in this study to extract the faces and the panels of the MSE wall. First, the MSE wall is partitioned into individual faces that can be considered planar segments (Figure 3.11). The sectioning process is conducted manually, and the planarity of each individual MSE wall face is examined by applying a plane fitting to the constituent points. A section/partition is accepted if the RMSE of the normal distance of the points from the best-fitting plane through this section is below a threshold that depends on the noise level in the data. Once the individual faces are established, the LF_{cs} is defined, as explained in Section 4.1. Then, a region-growing segmentation technique is applied to segment the points comprising the individual panels, as described by Habib and Lin (2016). The similarity criteria for the region growing process include the local point spacing (LPS) and the normal distance (n_d) between the points and the fitted plane through the face. The results of the segmentation for one face are shown in Figure 3.12. Following the panel segmentation technique, the P_{cs} for each of the segmented panels is simply defined by identifying the MBR enclosing the segmented panels, as proposed by Lin et al. (2019). More specifically, the X-axis of the P_{cs} is aligned along the normal to the panel's best-fitting plane through the point clouds along that panel. The Y-axis and Z-axis of the P_{cs} are aligned along the bottom and left sides of the panel in question, as can be seen in Figure 3.8. Having defined the LF_{cs} and P_{cs}, the serviceability measures can be obtained.

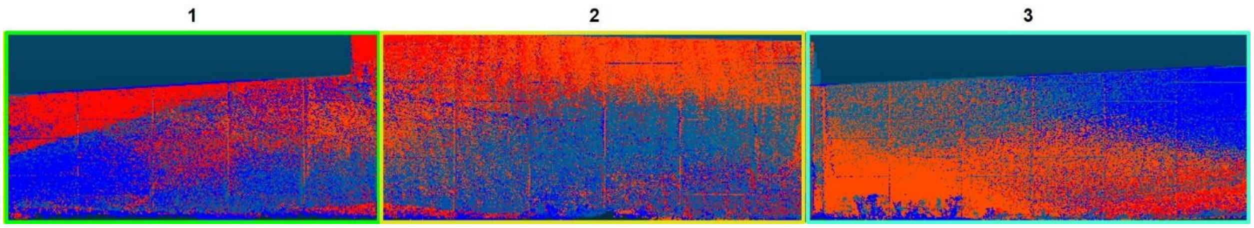

Figure 3.11. An example of manual extraction of the faces along an MSE wall with piece-wise planar façade (different colors along the MSE wall represent the different registered scans)

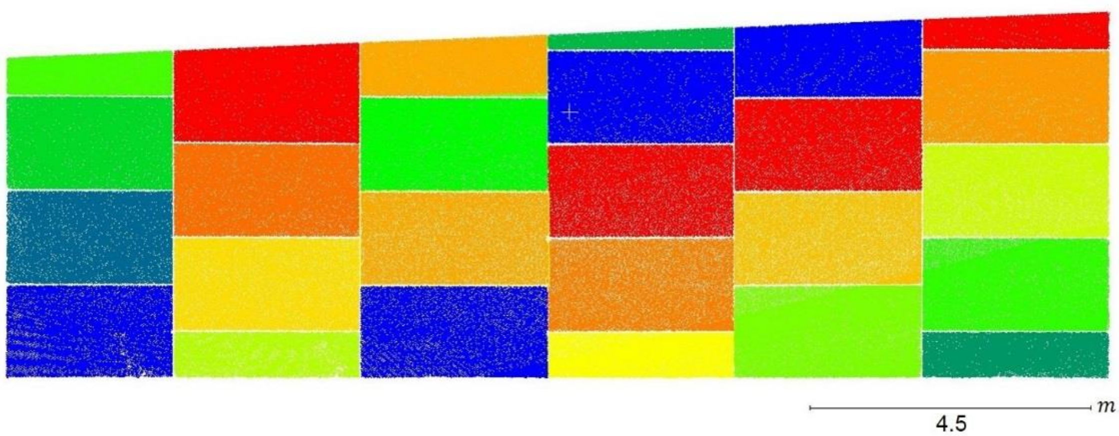

Figure 3.12. An example of segmented smooth MSE wall panels (different colors represent different segmented panels)

3.5.4 Derivation of standard and new serviceability measures

The standard serviceability measures include the longitudinal angular distortion (α_L) and the transversal angular distortion (α_T). The derivation of such measures is based on establishing longitudinal and transversal lines along the MSE wall face in question. Longitudinal lines are established by applying a line-fitting technique using the corners of the horizontal edges of all the panels adjacent to these lines. Once the line parameters (i.e., the directional vector of the 3D line) are estimated, a dot product between the directional line parameters and the Y-axis components of the LF_{cs} is used to obtain the longitudinal angular distortion (α_L). The transversal lines for the columns of panels are derived using the midpoints of the horizontal edges of the uppermost and lowermost panels of a given column. Then, to obtain the transversal angular distortion (α_T), a dot product of a vector connecting the midpoints of the uppermost and lowermost panel edges and the Z-axis components of the LF_{cs} is performed. An example of the longitudinal and transversal lines used for a planar face of the MSE wall is illustrated in Figure 3.13.

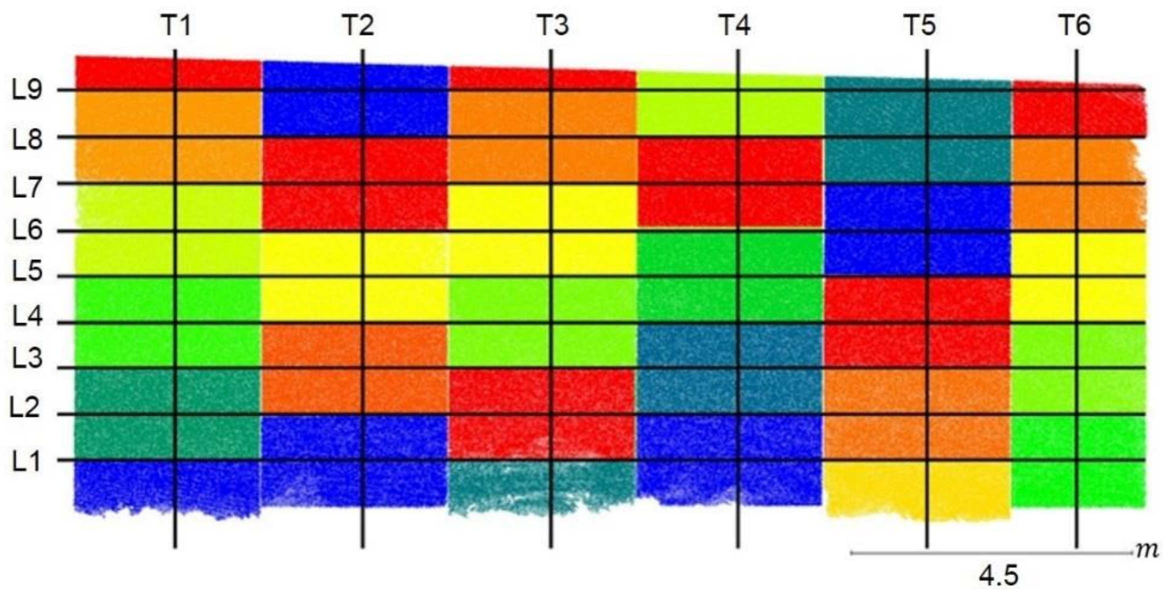

Figure 3.13 Longitudinal and transversal lines used to define the angular distortions for a planar face of the MSE wall

The recently developed serviceability measures by Lin et al. (2019) were used to evaluate the relative displacement and rotations of a panel relative to the LF_{cs}. The spatial and rotational relationships between the LF_{cs} and P_{cs}, as seen in Figure 3.8, are utilized to derive these serviceability measures. The location of the origin of the P_{cs} relative to the LF_{cs} (denoted as X_o, Y_o, and Z_o) defines the panel position. The rotation angles (denoted as θ_{xp}, θ_{y_P}, and θ_{z_P}) that need to be applied to the LF_{cs} to make it parallel to the P_{cs} are utilized to define the panel orientation. The final measure is the normal distances between the corners of each panel and the fitted planes through neighboring panels. These normal distances are derived using the derived corners from the MBR, as shown in Figure 3.14. In this figure, eight normal distances (denoted by the black lines) from the four corners of Panel 4 to the neighboring panels can be estimated.

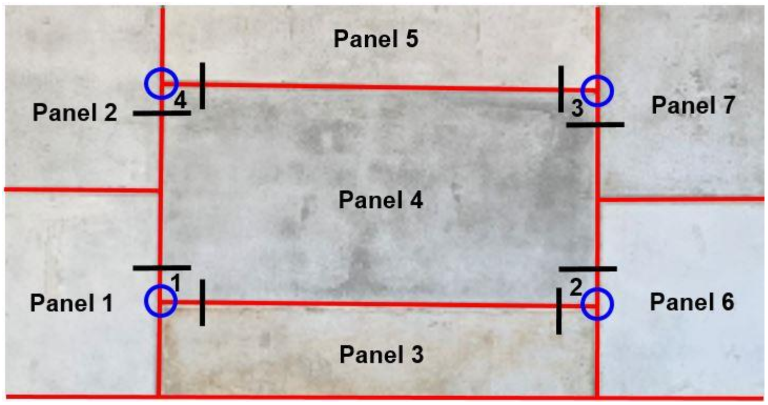

Figure 3.14 Evaluation of panel-to-panel out of-plane displacement

3.6 Experimental Results

To assess the capability of the developed MLS in monitoring large MSE walls with smooth precast concrete panels, a case study was conducted in the state of Indiana, USA, by comparing its results to those derived from a TLS dataset.

3.6.1 LiDAR point cloud alignment

Point cloud registration first was performed to register 1) the MLS point clouds from the two scanners onboard the MLS in a given drive run, 2) the MLS point clouds from two drive runs, 3) the TLS point clouds from the three scan stations, and 4) the MLS and TLS point clouds. The estimated transformation parameters relating the derived point clouds from the two MLS scanners in a given drive run were used to evaluate the quality of the system calibration procedure (i.e., significant deviations from zero shifts and zero rotation are indications of residual artifacts in the system calibration parameters). The estimated transformation parameters between the point clouds from different drive runs were used to quantitatively evaluate the quality of the GNSS/INS trajectory (i.e., significant deviations from zero shifts and zero rotation is an indication of the inferior quality of the GNSS/INS trajectory). The registration of the TLS and MLS point clouds was performed to ensure that there were uniquely defined local vertical and horizontal directions within the study site. To evaluate the comparative performance of TLS-based and MLS-based inspection strategies , the results for three faces (with a total of 78 panels) along façade 2 of the MSE wall (i.e., faces 2, 3, and 4) are examined. Two MLS drive runs in opposite directions covering the MSE wall were used for this comparative test. A total of six registration steps were conducted. The first and second steps involved the registration of the Riegl and ZF scans in each drive run. The third step performed the alignment between the combined/registered scans from the two drive runs. Three TLS scans were registered, in two sequential steps, to a unified coordinate system. Finally, the TLS and MLS point clouds were registered to a common reference frame defined by the latter. Figure 3.15 through Figure 3.18 qualitatively illustrate the point-cloud alignment of the derived point clouds from the two scanners (i.e., Riegl and ZF) in a given drive run, point clouds from two drive runs in opposite directions, point clouds from the TLS scan stations, and point clouds from the TLS and MLS units. In each of these figures, four vertical profiles were manually extracted to illustrate the alignment quality. These profiles exhibited a good overall alignment between the point clouds from the scanners in a given drive run, point clouds in two drive runs, point clouds in three TLS scans, and point clouds in the TLS/MLS units.

Table 3.2 through Table 3.5 report the respective transformation parameters along with the square root of a-posteriori variance factor ($\hat{\sigma}_{\circ}$) and average RMSE of the normal distances between the registered point clouds in Figure 3.15 through Figure 3.18. Close inspection of Figure 3.15 through Figure 3.18 and Table 3.2 through Table 3.5 reveals the following:

1. The estimated magnitudes of the transformation parameters necessary for the alignment of the Riegl and ZF scanner point clouds confirmed the high quality of the system calibration, as indicated by the small values of these parameters in Table 3.2 (the estimated parameters were in the range of 2 cm and 0.1°).
2. The estimated transformation parameters necessary for the alignment of the MLS point clouds from different drive runs indicated the presence of some discrepancies between these point clouds in the ranges of 2 to 10 cm and -0.1° to 0.06° as shown in Table 3.3. These discrepancies were mainly caused by the impact of environmental factors on the GNSS/INS trajectory derivation.
3. The reported square root of a-posteriori variance factor ($\hat{\sigma}_\circ$) and average RMSE of the normal distances between conjugate primitives for the different point clouds indicated the alignment quality following the registration process (i.e., in the range of 1 to 4 mm as can be seen in Table 3.2 through Table 3.5, these are well within the specifications of the used systems).

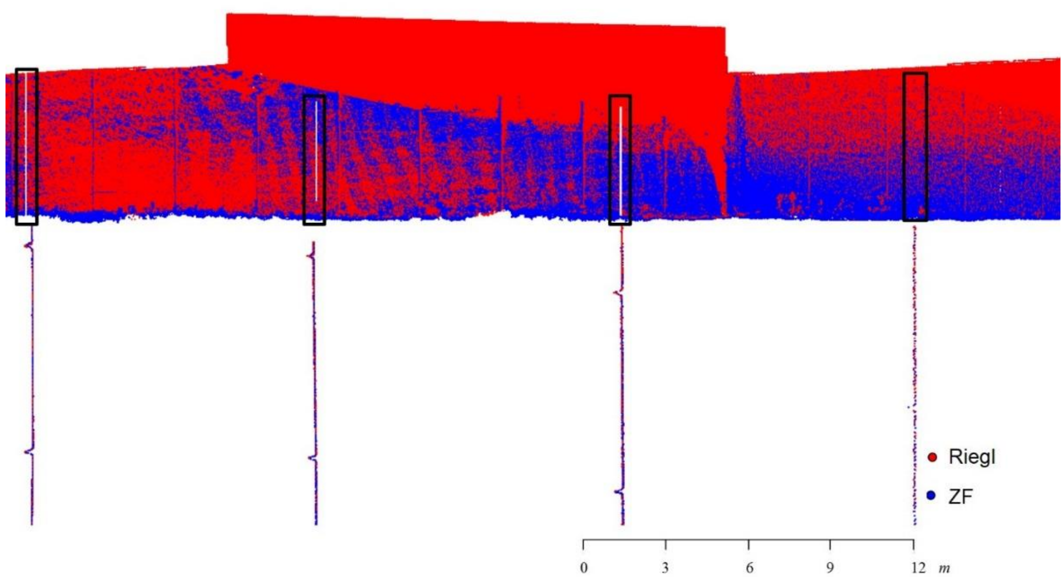

Figure 3.15. Cross sections illustrating the alignment quality of registered Riegl and ZF scans from a given drive run covering faces 1, 2, 3, and 4 along façades 1 and 2 of the MSE wall

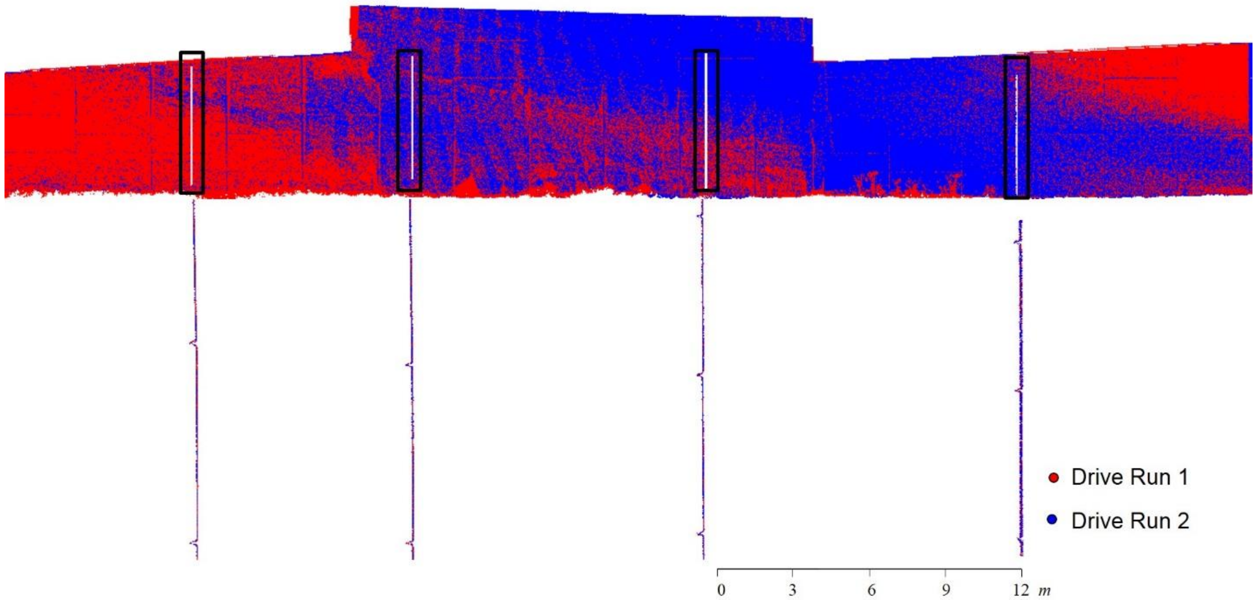

Figure 3.16. Cross sections illustrating the alignment quality of registered point clouds from the two MLS drive runs for covering faces 1, 2, 3, and 4 along façades 1 and 2 of the MSE wall

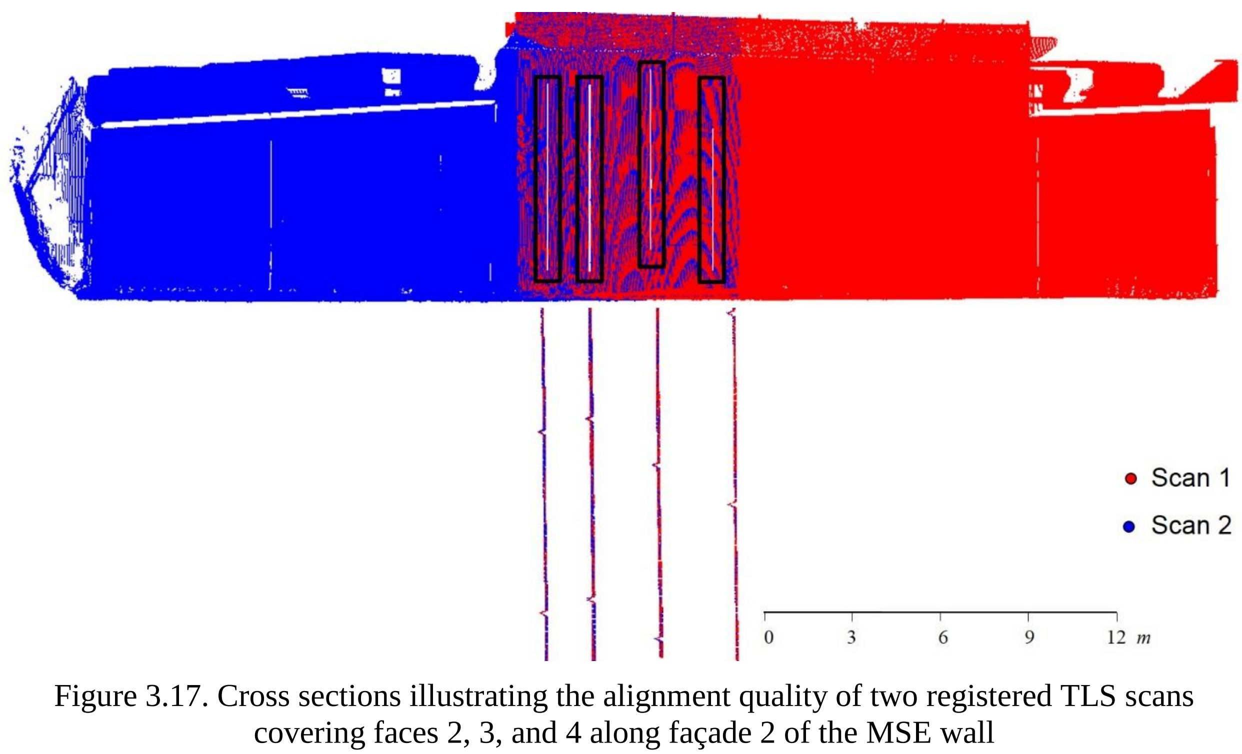

Figure 3.17. Cross sections illustrating the alignment quality of two registered TLS scans covering faces 2, 3, and 4 along façade 2 of the MSE wall

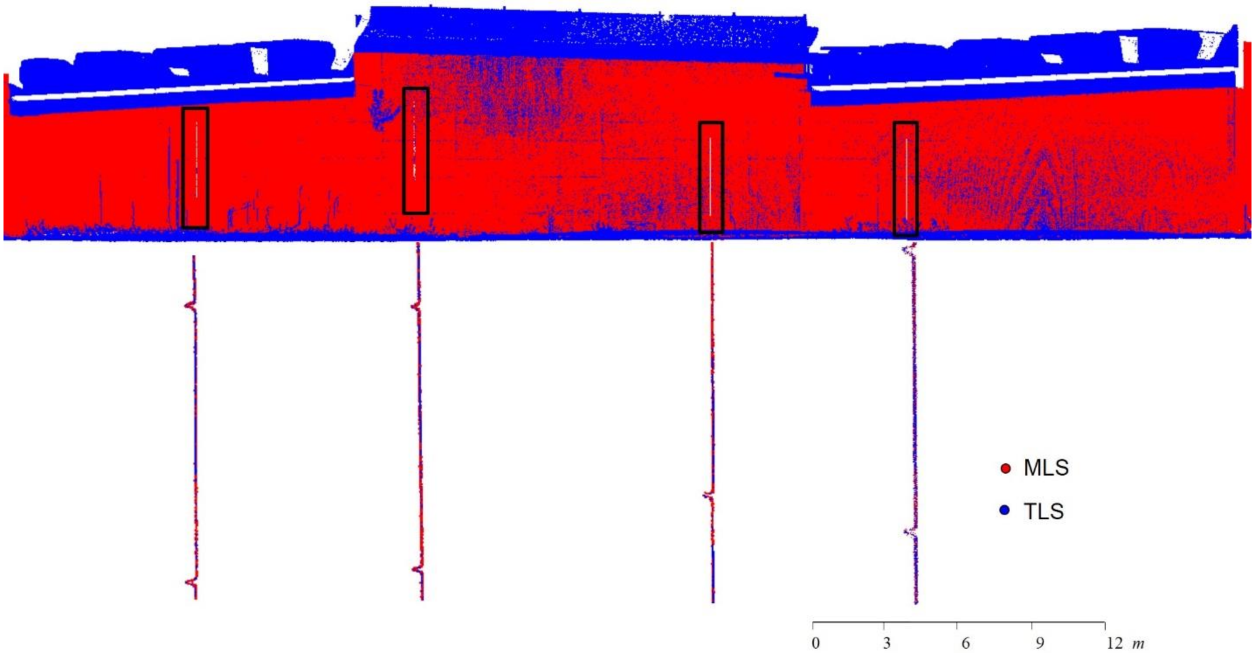

Figure 3.18. Cross sections illustrating the alignment quality of registered TLS and MLS point clouds covering faces 2, 3, and 4 of the MSE wall

Table 3.2. Estimated transformation parameters and quality measures (square root of a-posteriori variance factor, average normal distance among point-patch pairs, and RMSE of the normal distances) following the registration of the Riegl and ZF scans in a given drive run

X_T (m±mm)	Y_T (m±mm)	Z_T (m±mm)	Ω (deg±sec)	Φ (deg±sec)	Κ (deg±sec)	$\hat{\sigma}_\circ$ (m)	Average Normal Dist. (m)	RMSE (m)
-0.003	**0.023**	**0.002**	**-0.104**	**-0.008**	**0.014**	**0.0016**	**0.0012**	**0.0018**
±0.02	±0.01	±0.02	±0.01	~ ±0.00	~ ±0.00			

Table 3.3. Estimated transformation parameters and quality measures (square root of a-posteriori variance factor, average normal distance among point-patch pairs, and RMSE of the normal distances) following the registration of the MLS point clouds from different drive runs

X_T (m±mm)	Y_T (m±mm)	Z_T (m±mm)	Ω (deg±sec)	Φ (deg±sec)	Κ (deg±sec)	$\hat{\sigma}_\circ$ (m)	Average Normal Dist. (m)	RMSE (m)
0.028	**-0.108**	**0.012**	**0.064**	**-0.039**	**0.018**	**0.0034**	**0.0023**	**0.0037**
±0.01	~ ±0.00	±0.01	±0.01	~ ±0.00	~ ±0.00			

Table 3.4. Estimated transformation parameters and quality measures (square root of a-posteriori variance factor, average normal distance among point-patch pairs, and RMSE of the normal distances) following the registration of two TLS scans

X_T (m±mm)	Y_T (m±mm)	Z_T (m±mm)	Ω (deg±sec)	Φ (deg±sec)	K (deg±sec)	$\hat{\sigma}_\circ$ (m)	Average Normal Dist. (m)	RMSE (m)
6.73	18.98	-2.44	-0.005	-0.018	14.25	**0.0005**	**0.0006**	**0.0016**
±0.01	±0.01	±0.02	~ ±0.00	~ ±0.00	~ ±0.00			

Table 3.5. Estimated transformation parameters and quality measures (square root of a-posteriori variance factor, average normal distance among point-patch pairs, and RMSE of the normal distances) following the registration of the MLS and TLS point clouds

X_T (m±mm)	Y_T (m±mm)	Z_T (m±mm)	Ω (deg±sec)	Φ (deg±sec)	K (deg±sec)	$\hat{\sigma}_\circ$ (m)	Average Normal Dist. (m)	RMSE (m)
-4.33	16.01	2.26	0.07	0.01	-69.61	**0.0012**	**0.0009**	**0.002**
~ ±0.00	~ ±0.00	±0.01	~ ±0.00	~ ±0.00	~ ±0.00			

3.6.2 Serviceability measures

The longitudinal and transversal angular distortions for the MSE wall planar face (TLS in green and MLS in blue) as well as the recommended tolerable angular distortions (denoted by the red lines) are illustrated in Figure 3.19. These angular distortions were evaluated using the longitudinal and transversal line in Figure 3.13 (i.e., L1 to L9 and T1 to T6 for longitudinal and transversal angular distortions, respectively). The horizontal line in Figure 3.19(a) represents the tolerable longitudinal distortions for a joint width of 19 mm (0.75 in.). The horizontal line in Figure 3.19(b) represents the post-construction tolerable transversal angular distortions, as prescribed in AASHTO (2014). Figure 3.19 reveals that the angular distortions (both longitudinal and transversal) obtained from the MLS closely resembled those derived using the TLS, which confirmed the capability of mobile LiDAR to achieve a high-quality assessment of the standard serviceability measures. As far as the MSE wall evaluation is concerned, Figure 3.19(a) and Figure 3.19(b) show that this wall satisfied the longitudinal angular distortion criterion for a joint width of 19 mm (0.75 in). However, it failed to meet the tolerable transversal angular distortion criterion of 1/240.

(a)

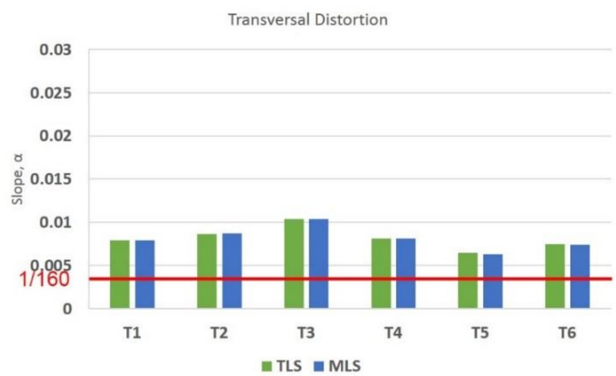

(b)

Figure 3.19. Angular distortion for the smooth MSE wall (i.e., face 3 along façade 2): (a) longitudinal angular distortion along lines L1-L9, and (b) transversal angular distortion along lines T1-T6 (the horizontal lines represent the tolerable angular distortions) L1-L9 and T1-T6 are illustrated in Figure 3.13

Recently-available serviceability measures, including the estimated values (i.e., the position of the most lower left corner of each panel (X_o, Y_o, and Z_o) and the angular orientation of each panel (θ_{x_P}, θ_{y_P}, and θ_{z_P}) relating the P_{cs} and LF_{cs} coordinate systems), are listed in Table 3.6 for TLS and MLS, respectively. For a perfectly constructed MSE wall, the X-coordinate of the origin of the P_{cs} relative to the LF_{cs}, denoted as X_o, should be close to zero. Moreover, the YZ-coordinates of the origin of the P_{cs}, denoted as Y_o and Z_o, should reflect the dimensions of the panels as well as the gap between the panels along the width and height directions, respectively.

The position of the panel can be used to detect the potential relative movements among the panels in a given face. Such movement can be identified and quantified through repetitive scans over time. The second set of measures are the angular rotations representing the relationship between the LF_{cs} and P_{cs}. As mentioned earlier, the rotation angles θ_{x_P}, θ_{y_P}, and θ_{z_P} represent the rotations that need to be applied to the LF_{cs} until it is parallel to the P_{cs}. Moreover, θ_{y_P} and θ_{z_P} can be viewed as rotations of the panel out of the LF_{cs}, while θ_{x_P} represents a rotation in the plane of the panel. For a perfectly constructed MSE wall, these rotation angles should be as close to zero as possible. Table 3.6 shows a sample of the calculated values of the recently-available performance measures (for the 32 panels of face 3 in façade 2).The derived dimensions of the complete panels can be used as an additional quality control measure for the proposed methodology by evaluating their closeness to the known panel size. For example, panels 3, 4, 5, and 7 had an estimated width and height varying from 2.95 to 2.97 m and from 1.46 to 1.48 m, respectively, as presented in Table 3.6. A graphical summary of Table 3.6 is provided in Figure 3.20 which shows the cumulative distribution functions (CDFs) for the three angular values (θ_{x_P}, θ_{y_P}, and θ_{z_P}) and the panel-to-panel normal distance of the TLS and MLS datasets.

The summary statistics for the proposed serviceability measures for the investigated 78 MSE wall panels within faces 2, 3, and 4 in façade 2 using the TLS and MLS point clouds are provided in Table 3.7. The results Table 3.7 show how TLS-derived measures (i.e., angular orientations and panel-to-panel displacements) quite resemble the performance measures derived using MLS, which validates the capability of using the MLS system to obtain the serviceability measures for MSE walls. For the TLS/MLS comparative evaluation, Table 3.8 shows the statistics of the differences between the TLS-based and the MLS-based serviceability measures, as well as the width and the height of the panels that can be also used as an additional quality control measure for the proposed methodology. For this comparison, two panels were excluded as they were not covered completely by either TLS or MLS point clouds. It can be concluded that the MLS-based similarity measures were within 1 cm and 0.3° for the recently available serviceability measures and within the 0.3/1000 for the standard measures (i.e., longitudinal and transversal angular distortions) when compared to those from TLS. In addition, the measures for the width and the height of the panels that are complete in size, were similar compared to those derived from a TLS dataset, and RMSE of the differences between the width and the height of the panels were between 1 and 2 cm.

Table 3.6. TLS-based and MLS-based panel parametrization (position, angular tilts, width and height) for face 3 along façade 2 of the MSE wall

ID	X_o (m) TLS	X_o (m) MLS	Y_o (m) TLS	Y_o (m) MLS	Z_o (m) TLS	Z_o (m) MLS	θ_{xp} (deg) TLS	θ_{xp} (deg) MLS	θ_{yp} (deg) TLS	θ_{yp} (deg) MLS	θ_{zp} (deg) TLS	θ_{zp} (deg) MLS	W (m) TLS	H (m) MLS	W (m) TLS	H (m) MLS
1	0.00	0.00	0.00	0.01	-0.08	-0.06	-0.07	-0.06	-1.61	-1.49	0.13	0.14	2.99	2.97	0.96	0.95
2	-0.02	-0.02	0.01	0.01	0.91	0.92	-0.20	-0.11	-0.33	-0.33	0.05	0.06	2.96	2.96	1.46	1.46
3	-0.03	-0.03	0.02	0.01	2.40	2.40	0.14	0.07	-0.69	-0.73	0.06	0.07	2.96	2.96	1.46	1.47
4	-0.05	-0.05	0.03	0.02	3.90	3.89	-0.07	0.05	-0.79	-0.79	0.03	0.05	2.95	2.96	1.46	1.47
5	-0.07	-0.07	0.02	0.01	5.39	5.40	-0.03	-0.24	0.12	0.11	0.03	0.03	2.96	2.96	1.46	1.46
6	-0.07	-0.06	0.01	0.02	6.91	6.89	-0.99	-0.36	0.37	0.22	-0.12	-0.09	2.96	2.95	0.51	0.49
7	-0.01	-0.01	3.01	3.01	0.14	0.14	0.24	0.19	-0.85	-0.85	-0.13	-0.12	2.96	2.97	1.47	1.48
8	-0.03	-0.03	3.01	3.01	1.65	1.64	-0.06	0.15	-1.09	-1.09	-0.03	-0.02	2.96	2.96	1.45	1.46
9	-0.05	-0.05	3.01	3.01	3.14	3.14	0.31	0.14	-0.51	-0.59	0.26	0.25	2.23	2.96	1.45	1.46
10	-0.06	-0.06	3.01	3.01	4.64	4.63	0.20	0.12	-0.38	-0.36	0.18	0.19	2.95	2.96	1.45	1.47
11	-0.06	-0.06	3.00	3.00	6.14	6.13	-0.07	-0.02	-0.03	-0.06	0.37	0.38	2.96	2.97	1.20	1.21
12	0.00	0.00	6.00	6.01	-0.08	-0.02	0.32	0.20	-1.08	-0.97	-0.07	-0.07	2.97	2.98	0.95	0.90
13	-0.02	-0.02	6.01	6.00	0.91	0.91	0.30	0.28	-0.64	-0.64	-0.32	-0.33	2.96	2.99	1.45	1.46
14	-0.04	-0.04	6.00	6.00	2.40	2.40	0.34	0.24	-0.42	-0.44	-0.53	-0.52	2.97	2.99	1.46	1.47
15	-0.05	-0.05	6.01	6.00	3.90	3.90	0.35	0.10	-1.00	-0.99	-0.55	-0.57	2.96	2.99	1.46	1.47
16	-0.07	-0.07	6.00	6.00	5.40	5.39	0.09	0.18	-0.66	-0.69	-0.44	-0.45	2.96	2.99	1.47	1.47
17	-0.08	-0.08	6.00	6.00	6.90	6.90	-0.08	0.15	0.68	0.63	-0.15	-0.16	2.96	2.99	0.36	0.37
18	0.00	0.00	9.01	9.01	0.17	0.18	-0.01	0.03	-0.58	-0.59	0.36	0.36	2.97	2.96	1.46	1.46
19	-0.01	-0.01	9.01	9.01	1.67	1.67	0.02	-0.04	-0.36	-0.35	0.31	0.31	2.97	2.96	1.45	1.46
20	-0.02	-0.03	9.02	9.00	3.17	3.16	-0.27	0.05	-0.46	-0.45	0.13	0.11	2.97	2.96	1.47	1.47
21	-0.03	-0.03	9.00	9.00	4.66	4.65	-0.02	-0.01	-0.84	-0.82	0.19	0.17	2.96	2.97	1.46	1.47
22	-0.06	-0.06	8.99	8.99	6.17	6.15	-1.14	-0.19	-0.20	-0.25	0.04	0.03	2.97	2.97	1.03	1.04
23	-0.01	-0.01	12.02	12.01	-0.07	-0.07	-0.03	0.03	-0.80	-0.80	0.16	0.15	2.96	2.97	0.96	0.96
24	-0.03	-0.03	12.02	12.00	0.92	0.93	-0.01	-0.04	-0.45	-0.44	-0.13	-0.15	2.96	2.97	1.46	1.46
25	-0.03	-0.03	12.01	12.00	2.42	2.43	-0.05	-0.20	-0.23	-0.22	0.03	0.01	2.96	2.97	1.47	1.47
26	-0.04	-0.04	12.00	12.00	3.93	3.92	-0.15	-0.19	-0.28	-0.23	-0.17	-0.19	2.96	2.97	1.46	1.47
27	-0.05	-0.05	11.99	11.99	5.43	5.42	-0.30	-0.41	-0.82	-0.85	-0.23	-0.24	2.97	2.98	1.69	1.69
28	-0.02	-0.02	15.02	15.00	0.16	0.15	0.29	-0.01	-0.29	-0.27	0.85	0.84	2.13	2.14	1.47	1.48
29	-0.03	-0.03	15.01	15.00	1.66	1.67	0.34	0.18	-0.57	-0.57	0.97	0.97	2.14	2.14	1.46	1.46
30	-0.04	-0.04	15.01	15.00	3.15	3.16	0.44	0.05	-0.04	-0.01	1.19	1.19	2.15	2.15	1.46	1.46
31	-0.03	-0.03	15.00	15.00	4.66	4.66	0.09	-0.10	-0.96	-0.93	1.43	1.44	2.14	2.14	1.47	1.47
32	-0.06	-0.06	15.01	15.00	6.16	6.15	-0.24	0.29	-0.40	-0.42	1.30	1.28	2.14	2.14	0.88	0.89

Table 3.7 TLS-based and MLS-based summary statistics of the derived serviceability measures for 78 panels (faces 2, 3, and 4 in façade 2) of the MSE wall

	θ_{xp} (deg.)		θ_{yp} (deg.)		θ_{zp} (deg.)		Panel-to-Panel Displacement (mm)	Panel-to-Panel Displacement (mm)
	TLS	MLS	TLS	MLS	TLS	MLS	TLS	MLS
Sample Size	78	78	78	78	78	78	454	454
Minimum Value	-1.14	-0.48	-1.61	-1.49	-0.77	-0.77	-14.10	-16.00
Maximum Value	0.47	0.38	0.68	0.63	1.43	1.44	13.50	18.10
Range	1.60	0.86	2.29	2.11	2.21	2.21	27.60	34.10
Average	-0.03	0.00	-0.46	-0.45	0.06	0.07	-0.30	-0.21
Standard Deviation	0.26	0.19	0.4	0.39	0.48	0.48	4.97	5.19
5th Percentile	-0.39	-0.39	-1.12	-1.09	-0.61	-0.58	-8.80	-9.00
25th Percentile	-0.11	-0.12	-0.72	-0.73	-0.20	-0.22	-3.70	-3.70
50th Percentile (median)	-0.03	0.00	-0.45	-0.44	0.01	0.01	-0.20	-0.20
75th Percentile	0.09	0.14	-0.21	-0.20	0.18	0.18	3.10	3.20
95th Percentile	0.34	0.28	0.12	0.14	1.19	1.19	7.70	8.40
Interquartile Range (IQR)	0.20	0.26	0.52	0.53	0.39	0.40	6.80	6.90

Table 3.8 RMSE of the differences between the TLS-based and MLS-based serviceability measures for complete panels (i.e., 76 panels) within faces 2, 3, and 4 along façade 2 of the MSE wall

	New-available serviceability measures						Standard serviceability measures			Quality control	
	X_o (m)	Y_o (m)	Z_o (m)	θ_{xp} (deg.)	θ_{yp} (deg.)	θ_{zp} (deg.)	α_L (10^{-3})	α_T (10^{-3})	Panel-to-Panel disp. (m)	W (m)	H (m)
RMSE	0.001	0.0027	0.019	0.23	0.30	0.048	0.34	0.37	0.0039	0.0101	0.022

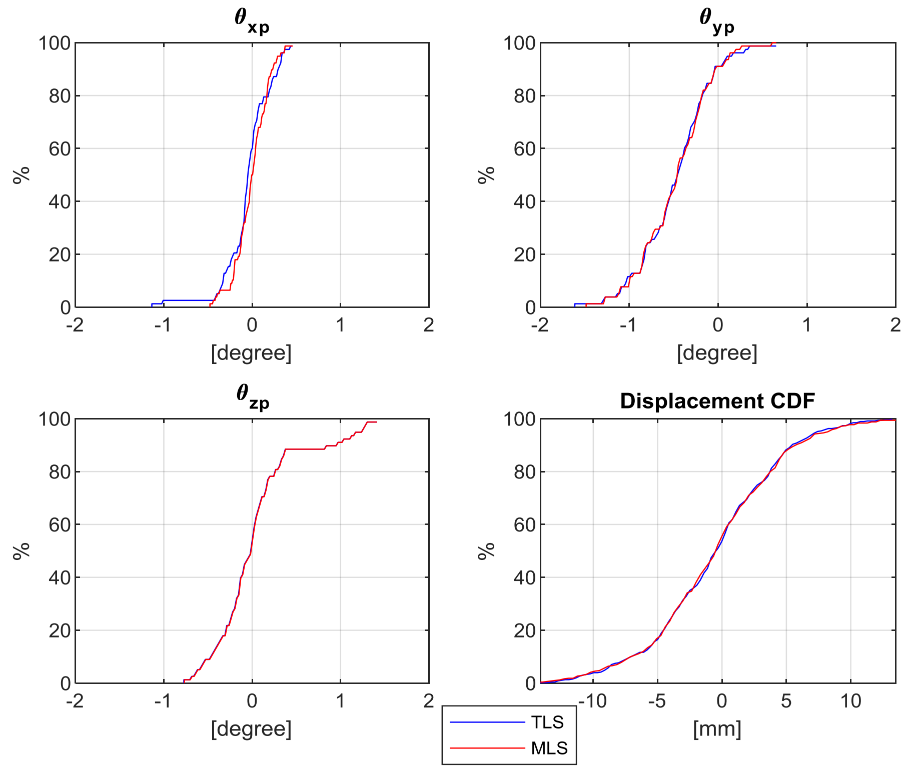

Figure 3.20. Cumulative Distribution Functions (CDF) for panel3D orientation and panel-to-panel displacement using TLS (in blue) and MLS (in red) point clouds (for 78 panels constituting three faces along façade 2)

One of the basic assumptions of MSE walls is that the joints (i.e., gaps) between neighboring panels are within a tolerable range where panels are sufficiently close to each other and have minimal offsets along the X-axis of the P_{cs}. To assess the accuracy of the automatically derived panel-to-panel normal distance between neighboring panels, such distances were compared to interactively measured distances in the TLS point cloud, MLS point cloud, and profiler gauge measurements at locations i, ii, and iii, as indicated in Figure 3.21.

Figure 3.22 shows the independent checks of the panel-to-panel normal distance – where

Figure 3.22(a) shows the interactive measurements from the point cloud, and

Figure 3.22(b) shows the use of the profiler gauge. The profiler gauge measurements are an independent evaluation of the absolute accuracy of derived normal distances. The estimated values for panel-to-panel normal distances derived from approaches are shown in in Figure 3.23. The results in Figure 3.23 indicate that the panel-to-panel normal distances at locations i, ii, and iii obtained from the TLS, MLS data, (automated or interactive measurements from point cloud data), and the profile gauge were in good agreement (i.e., the reported numbers in Figure 3.23 are within the range of ±0.5 cm).

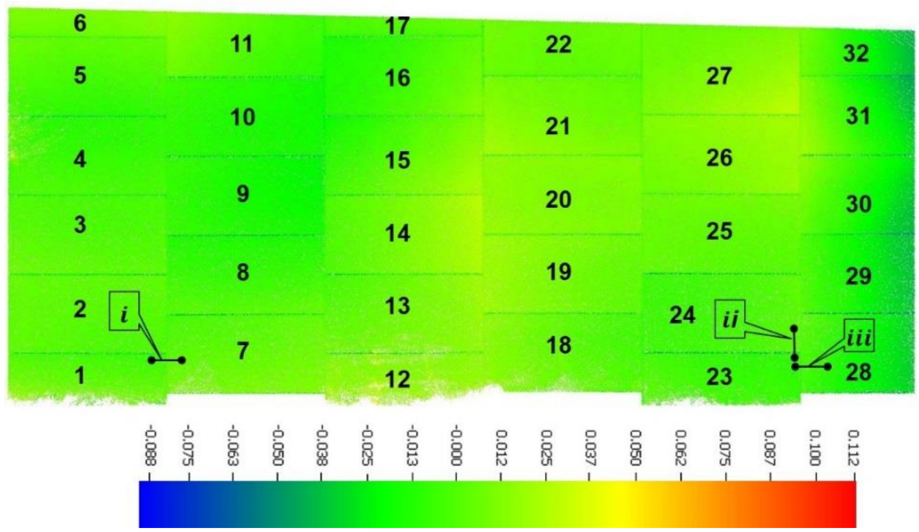

Figure 3.21 Overall out-of-plane displacement map for a façade of the MSE wall face (units for the values along the scale bar are in meters)

(a) (b)

Figure 3.22 Validation of panel-to-panel normal distance measurement: (a) interactive measurement from point cloud, (b) on-site profiler gauge approach

	Automated Measurement		Interactive Point Cloud Measurement		Independent Quality Control Measurements
Location	Normal distance of **TLS** derived from the proposed approach	Normal distance of **MLS** derived from the proposed approach	Profile view of **TLS** data measurement	Profile view of **MLS** data measurement	Profiler gauge measurement
i	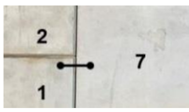 North-East Corner of Panel 1 Relative to Panel 7 **1.1 cm**	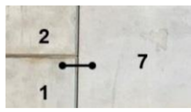 North-East Corner of Panel 1 Relative to Panel 7 **0.97 cm**	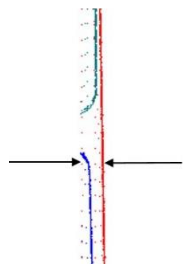 **1.07 cm**	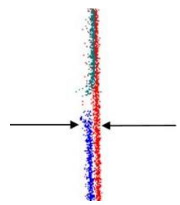 **1.01**	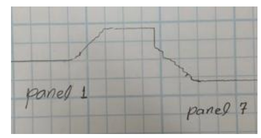 **0.85 cm**
ii	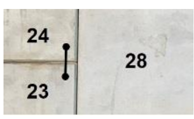 North-East Corner of Panel 23 Relative to Panel 24 **1.20 cm**	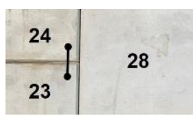 North-East Corner of Panel 23 Relative to Panel 24 **1.22 cm**	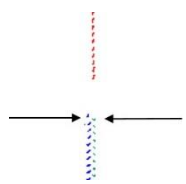 **1.06 cm**	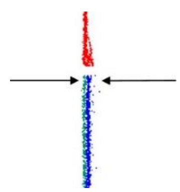 **1.14 cm**	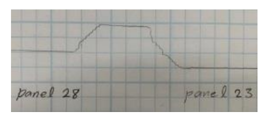 **0.9 cm**
iii	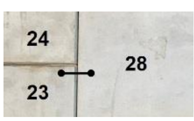 North-East Corner of Panel 23 Relative to Panel 28 **1.12 cm**	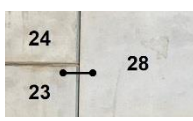 North-East Corner of Panel 23 Relative to Panel 28 **1.08 cm**	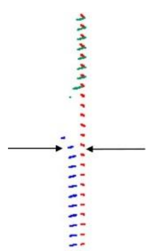 **0.96 cm**	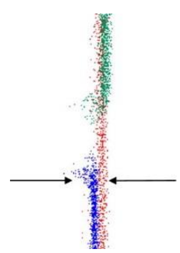 **0.98 cm**	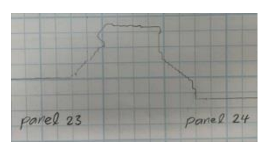 **1.00 cm**

Figure 3.23 Validation of panel-to-panel out of-plane displacement (different color in the interactive point cloud measurements columns represent different panels)

Regarding the whole MLS dataset, Table 3.9 provides statistics about the proposed serviceability measures, derived using the MLS point clouds, for all the complete/non-occluded panels of the smooth MSE wall (160 panels). Figure 3.24 shows the CDFs for the three angular values (θ_{x_P}, θ_{y_P}, and θ_{z_P}) and the panel-to-panel normal distance of the MLS dataset at the case study site. The graphical summary shown in Figure 3.24 is much easier to use for identifying trends and outliers than examining the values of each individual panel of the MSE wall. As can see in Table 3.9 that the angular deviation values were less than 1° for all the tilts around the X-axis, Y-axis, and Z-axis. Table 3.9 also shows that 95% of the panels had an offset of less than 1.00 cm, which indicated that the wall meets the tolerable out-plane offset prescribed by FHWA (2009).

Table 3.9 MLS-based summary statistics of the serviceability measures for 160 panels constituting eight faces along façades 1, 2, and 5 of the MSE wall

	θ_{xp} (deg.)	θ_{yp} (deg.)	θ_{zp} (deg.)	Panel-to-Panel Displacement (mm)
Sample Size	160	160	160	911
Minimum Value	-2.68	-1.43	-1.09	-32.30
Maximum Value	1.14	1.45	1.97	30.50
Range	3.82	2.88	3.05	62.80
Average	-0.35	0.01	0.05	-0.10
Standard Deviation	0.50	0.50	0.36	6.73
5th Percentile	-1.15	-0.82	-0.50	-10.70
25th Percentile	-0.60	-0.26	-0.12	-3.80
50th Percentile (median)	-0.33	0.00	0.00	-0.10
75th Percentile	-0.04	0.20	0.22	3.60
95th Percentile	0.33	0.98	0.63	9.80
Interquartile Range (IQR)	0.57	0.46	0.34	7.40

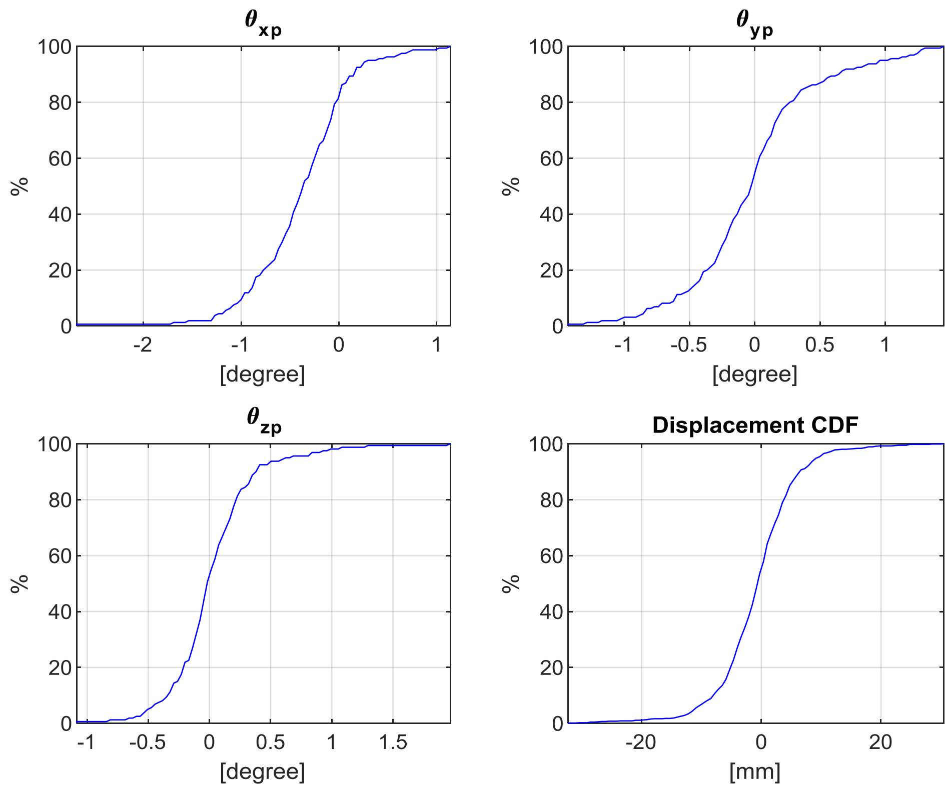

Figure 3.24 Cumulative Distribution Functions (CDF) for the MLS-based panel 3D orientation and panel-to-panel displacement (for 160 panels constituting eight faces along façades 1, 2, and 5)

3.7 Conclusions and Recommendations for Future Work

MSE walls are a commonly used civil infrastructure due to their low-cost, ease of construction, and accommodation of tight right-of-way constraints. Periodically monitoring MSE walls is necessary to ensure that they perform in accordance with a wide range of serviceability measures that describe both global and local deformations within the wall. The current techniques for MSE wall monitoring are time consuming, limit access to transportation corridors, and expose inspectors and/or instrument operators to incoming traffic risks. Prior research has shown that TLS is a promising tool for deriving both standard global and new local serviceability measures, but the time-consuming nature of scanner set-up and data collection makes it an impractical approach that is not be scalable. Therefore, the study presented in this paper proposed the use of MLS for data acquisition and introduced a processing framework that could evaluate all types of serviceability measures.

The research objectives were tested using a case study in the state of Indiana that evaluated the comparative performance of the TLS and MLS data acquisition modalities. The key findings/contributions of the proposed acquisition/processing strategy can be summarized as follows:

1. The study illustrated the potential of mobile LiDAR in collecting point clouds with sufficient point density to derive global and local serviceability measures.
2. The study introduced a framework for point-cloud processing, which includes registration, segmentation, panel isolation, and serviceability measures evaluation, more specifically:
    a. A hybrid approach for the fine registration of scans from different sensors in a given drive run and scans from different drive runs.
    b. A process that ultimately uses the extracted panels to derive both global and local serviceability measures.
3. With an accurate system calibration and a high-quality GNSS/INS onboard an MLS, the point clouds from different sensors and different drive runs can be used to enhance the level of detail in the collected point clouds.
4. The potential of MLS was evaluated through comparative evaluation with TLS, and the derived serviceability measures from TLS and MLS were in close agreement agreement within the range of 0.3/1000 for the standard measures (i.e., longitudinal and transversal angular distortions) and 1 cm and 0.3° for the recently-available serviceability measures.
5. The derived panel-to-panel distance measure from TLS and MLS were quite similar (within the range of 0.5 cm) providing additional validation for the potential of MLS.

6. Extensive testing with large real dataset demonstrated the feasibility of the different components of the proposed processing strategy. To the best of the authors' knowledge, this is the first study of its kind (i.e., the first study that has verified the ability of mobile LiDAR in the acquisition and generation of a wide range of serviceability measures for MSE walls with smooth precast concrete panels).

The proposed methodology can be used to establish acceptance criteria for new projects, derive measures for monitoring the long-term serviceability of existing MSE walls, and/or propose criteria to assess the serviceability of MSE walls in regions susceptible to natural disasters. Employing the proposed methodology and data acquisition strategy can reduce cost that would otherwise be associated with infrastructure management and can improve the overall quality of the infrastructure by enhancing maintenance operations.

Future extensions of the work will focus on the following actions:

1. Developing a fully automated partitioning process for MSE walls with piece-wise planar façades.
2. Incorporating the reported discrepancies among the point clouds from multiple scans onboard the MLS or different drive runs to improve the system calibration and GNSS/INS trajectory.
3. Investigating the impact of environmental parameters (neighboring traffic) as well as technical factors (driving speed) of the derived serviceability measures.
4. Expanding the processing strategy to handle MSE walls with non-identical, textured panels.
5. Investigating the potential use of lower grade MLS to generate reliable serviceability measures.

4. MOBILE LIDAR FOR MSE WALL WITH TEXURED PRECAST CONCRETE PANELS

This chapter was originally published in the remote sensing journal: Aldosari, M., Al-Rawabdeh, A., Bullock, D., & Habib, A. (2020). A Mobile LiDAR for Monitoring Mechanically Stabilized Earth Walls with Textured Precast Concrete Panels. Remote Sensing, 12(2), 306.

4.1 Abstract

Mechanically Stabilized Earth (MSE) walls retain soil on steep, unstable slopes with crest loads. Over the last decade, they are becoming quite popular due to their low cost-to-benefit ratio, design flexibility, and ease of construction. Like any civil infrastructure, Mechanically Stabilized Earth (MSE) walls need to be continuously monitored according to transportation asset management criteria during and after the construction stage to ensure that their expected serviceability measures are met and to detect design and/or construction issues, which could lead to structural failure. Current approaches for monitoring MSE walls are mostly qualitative (e.g., visual inspection or examination). Besides being time consuming, visual inspection might have inconsistencies due to human subjectivity. This research focuses on a comprehensive strategy using a Mobile LiDAR mapping System (MLS) for the acquisition and processing of point clouds covering the MSE wall. The processing strategy delivers a set of global and local performance measure for MSE walls. Moreover, it is also capable of handling MSE walls with smooth or textured panels with the latter being the focus of this research due to its more challenging nature. For this study, an ultra-high-accuracy wheel-based MLS has been developed to efficiently acquire reliable data conducive to the development of the serviceability measures. To illustrate the feasibility of the proposed acquisition/processing strategy, two case studies in this research have been conducted with the first one focusing on the comparative performance of static and mobile LiDAR in terms of the agreement of the derived serviceability measures. The second case study

aims at illustrating the feasibility of the proposed strategy in handling large textured MSE walls. Results from both case studies confirm the potential of using MLS for efficient, economic, and reliable monitoring of MSE walls.

Keywords: Textured MSE walls; Mobile LiDAR Mapping Systems (MLS); static Terrestrial Laser Scanning (TLS); Performance/Serviceability Measures; Civil Infrastructure; Segmentation; Characterization

4.2 Introduction

Mechanically Stabilized Earth (MSE) walls have been widely used to stabilize steep, unstable slopes that are subjected to crest loads (Oskouie et al., (2016)). Low-cost construction and ease of installation have made MSE walls with precast concrete panels a common infrastructure along transportation corridors within the United States as well as other countries. For instance, in the state of Indiana, USA, there are roughly 1,200 to 1,500 MSE walls excluding those on Local Public Agency (LPA) routes (Rearick and Khan, 2017). An MSE wall is comprised of several components including a façade of precast concrete panels supporting many compacted backfill layers strengthened with geosynthetic or metallic reinforcement (Passe, 2000). A typical cross-section of the components of an MSE wall is shown in Figure 4.1. Modular facing blocks, which could be smooth or textured – i.e., with several architectural and aesthetically pleasing finishes, constitute the façade of the MSE wall (Lin et al., 2019 and McGuire et al., 2017). The key function of these facing panels is preventing backfill soil material from leaking out of the joints. The joints between the panels permit excessive water to seep through them. Failure of an MSE wall can lead to loss of life and/or property damage. Therefore, a monitoring strategy that can quickly, economically, and reliably detect any anomalies in an MSE wall is of high importance.

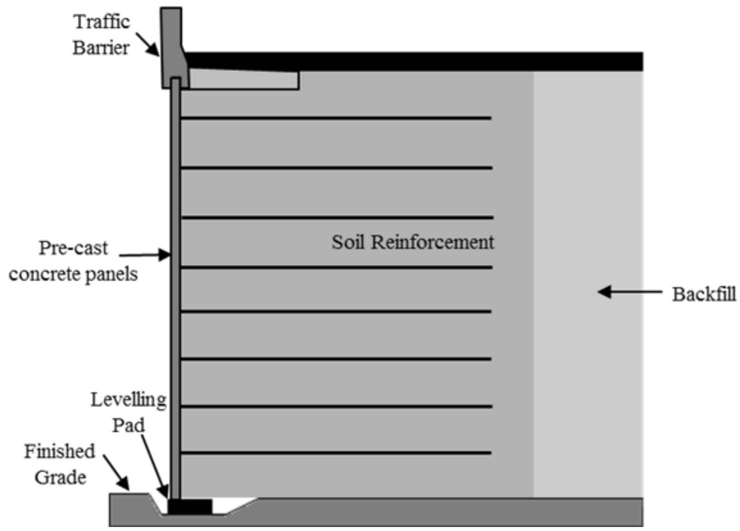

Figure 4.1. Typical cross-section profile of an MSE wall (modified after (Passe, 2000))

The long-term performance of an MSE wall relies on a well-designed and constructed system that meets the specifications provided by regulatory organizations such as the U.S. Departments of Transportation (DOTs). Internal and external inspections are regularly conducted to ensure the prevention of reinforcement rupture and pullout from the facing panels. A commonly accepted set of serviceability measures include the longitudinal angular distortion (α_L) and the transversal angular distortion (α_T), which have been proposed by the American Association of State Highway and Transportation Officials (AASHTO, 2014). The longitudinal angular distortion (α_L) is defined as the ratio of the differential settlement between two points along the length of the MSE wall to the horizontal distance between them as illustrated in Figure 4.2(a). The transversal angular distortion (α_T) is defined as the lateral deflection (i.e., out of the wall plane) of the MSE wall divided by its height, as illustrated in Figure 4.2(b).

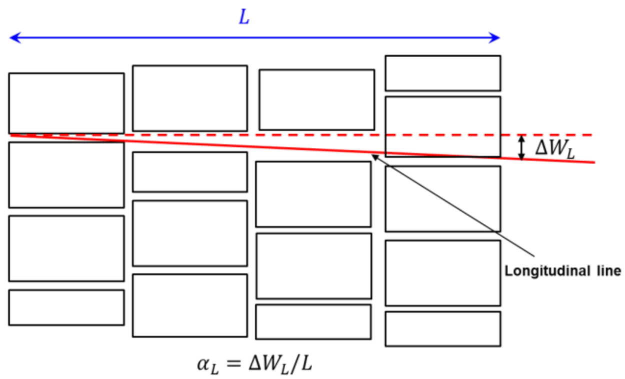

(a)

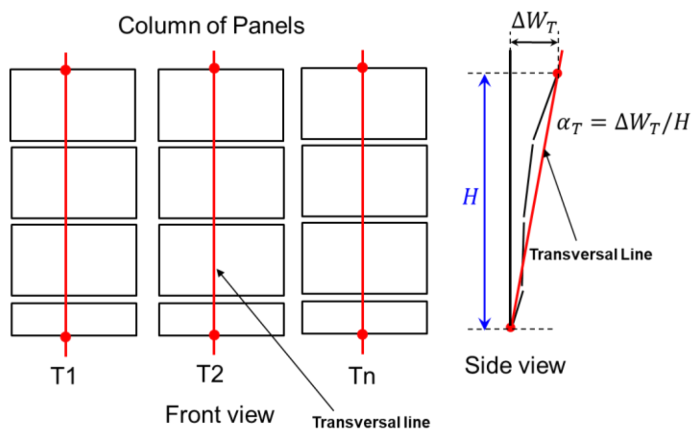

(b)

Figure 4.2. Definition of (a) longitudinal and (b) Transversal angular distortions

Table 4.1 provides the tolerable α_L values for MSE walls that are constructed using incremental precast concrete panels with different joint widths. For the transversal angular distortion, during the construction of an MSE wall with incremental precast concrete panels, the tolerable α_T values when measured with a 3.048 m (10 ft) long straight edge should be less than 1/160. At the end of wall construction, α_T should be less than 1/240 when measured using a plumb line dropped from the top to the bottom of the constructed wall (AASHTO, 2014). In addition to the angular distortions, the U.S. Federal Highway Administration provided guidelines for tolerable out-of-plane offset between neighboring panels (FHWA, (2009)). According to such guidelines, the out-of-plane offset at any joint should be less than 9.53 mm (3/8 in) during wall construction. The standard serviceability measures, with the exception of the out-of-plane offset, are global measures focusing on the vertical settlement and lateral deflection of an MSE wall. However, most MSE wall failures are closely related to local deformations, such as relative angular tilt and displacement among neighboring panels, as shown in Figure 4.3. Therefore, a reliable monitoring should be capable of providing measures that evaluate the deformation behavior of the individual panels within an MSE wall. Examples of such measures are those proposed by Lin et al., 2019.

Table 4.1.Tolerable longitudinal angular distortion (α_L) values for MSE walls constructed with incremental precast concrete panels (modified from (AASHTO, 2014)).

Joint width w_J	**Panel area ≤ 2.8 m^2 (30 ft^2)**	**2.8 m^2 (30 ft^2) < Panel area ≤ 7 m^2 (75ft^2)**
19 mm (0.75 inch)	$\alpha_{L,tol}$ = 1/100 = 0.01	$\alpha_{L,tol}$ = 1/200 = 0.005
13 mm (0.50 inch)	$\alpha_{L,tol}$ = 1/200 = 0.005	$\alpha_{L,tol}$ = 1/300 = 0.003
6 mm (0.25 inch)	$\alpha_{L,tol}$ = 1/300 = 0.003	$\alpha_{L,tol}$ = 1/600 = 0.002

(a) (b)

Figure 4.3. An example of (a) an MSE wall failure that started with (b) an excessive angular deformation (bulging) between neighboring panels

Other than the serviceability measure type, the monitoring strategy should also consider factors that would affect the practical implementation and scalability of such an approach. Total station, geotechnical field instrumentations, and/or static Terrestrial Laser Scanning (TLS) are the most commonly used data acquisition systems for the derivation of the serviceability measures. However, such instruments require access to the MSE wall site and this could subject the inspectors to hazardous conditions as a result of incoming traffic. In addition, field data collection is time consuming; thus, making the monitoring process non-scalable. The third challenge, which should be addressed by a monitoring strategy, is its ability to deal with both smooth and textured MSE walls that could be straight or curved (i.e., the MSE wall is comprised of a set of individual planar faces – Figure 4.4(a) – or a single curved façade which could be considered piece-wise planar – Figure 4.4(b)). Prior research (e.g., Lin et al., 2019) has mainly dealt with planar MSE walls with smooth panels (i.e., the one in Figure 4.4(a). Therefore, the development of a methodology that could deal with any type of MSE walls would be valuable. In response to existing challenges for monitoring MSE walls, this research is focusing on addressing the following three objectives:

1. Development of a monitoring strategy that could be used for the delivery of both standard and recently-available serviceability measures,
2. The monitoring strategy is based on reliable, scalable data acquisition procedure – more specifically, point clouds captured by a Mobile LiDAR mapping System (MLS) will be used for serviceability measures derivation, and
3. The strategy could handle MSE walls with smooth or textured precast concrete panels along either planar or piece-wise planar façades.

In this paper, Section 4.3 starts with an overview of existing MSE wall monitoring strategies with an emphasis on those utilizing LiDAR point clouds. Then, the developed MLS data acquisition system and two case studies used in this paper are presented in section 4.4. The first one focused on illustrating the fact that an MLS can provide similar performance measures to those derived from TLS. The second case study, on the other hand, aims to illustrate that the data acquisition modality and processing strategy are capable of monitoring large MSE walls along a transportation corridor. The MSE walls considered in both case studies have piece-wise planar façades and are comprised of textured panels. The study then proceeds with the coverage of the proposed methodology in section 4.5 and experimental results for the two case studies are discussed in section 4.6. Finally, in section 4.7, it concludes with the main findings of this study and the recommendations for future research.

(a)

(b)

Figure 4.4.Two types of MSE walls: (a) Multi-face planar MSE wall and (b) Curved MSE wall with a piece-wise planar face

4.3 Related Work

Commonly used MSE wall monitoring techniques are based on visual inspection/examination using a variety of instruments, such as measuring tapes and plumb lines. However, such techniques may have inconsistencies due to human subjectivity that vary over time (Oats et al., 2017). Other methods for evaluating some serviceability measures for MSE walls with precast concrete panels include the use of a Total Station or TLS. Laefer et al., (2008) proposed an approach for monitoring retaining walls using TLS. For the data collection, multiple temporal scans are required to detect any movements of the vertically stacked panels within an MSE wall. Each scan must include at least three spherical targets, which are used as reference points for registration/alignment and monitoring purposes. The spherical targets should be placed at the same location for each scanning operation. The study recommended that the targets are left on-site for the duration of the monitoring course. Oskouie et al., (2016) utilized TLS to acquire point clouds to derive some performance measures for MSE walls. In their research and before starting any data processing, they first cleaned the data from unwanted objects, such as temporary steel and wooden brackets. Then, a planar model is fitted through the wall using the random sample consensus (RANSAC) algorithm (Fischler and Bolles, 1981). Based on the distance between the fitted plane surface and the vertical/horizontal joints separating neighboring panels, joint distances are reported. More specifically, vertical/horizontal joints are considered as outliers when inspecting their normal distances relative to the fitted wall plane surface. Lienhart et al., (2018) presented a practical approach for large-scale monitoring of retaining walls along Austrian highways using a Mobile Mapping System (MMS). The measurement platform consisted of two laser scan profilers, inertial measurement unit (IMU), differential Global Navigation Satellite System (GNSS) receiver, and multiple cameras. The cameras are utilized to provide true colors for the point clouds. The aligned point clouds from different sensors were used to generate vertical profiles every 5 cm along the retaining wall by intersecting the wall surface model with planes orthogonal to the vehicle's trajectory. A fitted regression along the vertical profile is then used to derive the tilt angle. They found that it is possible to determine the tilt angle with an accuracy better than 0.1°. However, their approach is limited to evaluating the transversal out-of-plane angle of the retaining wall, which is similar to the AASHTO-based transversal angular distortion (α_T). Lin et al., (2019) utilized TLS to derive the standard longitudinal and transversal angular distortions of MSE walls with smooth panels. In their work, they also derived new measures that describe out-of-plane angular tilts and displacements of the panels relative to the individual MSE wall faces. For the derivation of the standard and new performance measures, Lin et al. (2019) defined coordinate systems for the individual faces and panels, denoted as the Levelled Face (LF_{cs}) and Panel (P_{cs}) coordinate systems, respectively. LF_{cs} was derived by using a plane fitting through a manually-cropped face of an MSE wall and considering the local horizontal/vertical directions within the site. The definition of the P_{cs} started with the identification of the individual panels through a region segmentation procedure where the normal distance between the points along the face and the best fitting plane through these points was used as the segmentation criterion. Following the panel segmentation, its bounding box – i.e., Minimum Bounding Rectangle (MBR) (Freeman and Shapira, 1975) – was used to define the P_{cs}. The new serviceability measures developed in their work were based on the spatial and rotational relationships between the (LF_{cs}) and (P_{cs}).

The above literature has already shown the potential of using TLS for MSE wall monitoring while providing high accuracy, reliable serviceability measures. However, the TLS monitoring strategy is time-consuming, limit traffic accessibility, and has not been fully tested when dealing with large MSE walls with either smooth or textured panels. Due to the large number of existing MSE walls, the limited monetary resources, and the time-critical needs, the frequency of scheduled inspections is not always sufficient to detect problems in a timely manner. In order to verify MSE walls integrity more efficiently, the presented research in this study proposes a monitoring strategy that is based on an MLS. Such systems collects high accuracy, high resolution point clouds in a short time while driving along the transportation corridor. The system description together with the involved case studies are presented next, in section 4.4.

4.4 Acquisition System Specifications and Configuration of the Case Studies

The main objective of this research is illustrating the feasibility of using a wheel-based MLS for the acquisition of point clouds that could be used for the derivation of standard as well as recently- available MSE wall serviceability measures for textured MSE walls. An in-house developed MLS, shown in Figure 4.5, has been used for the involved case studies. The system is comprised of two high-grade laser scanners (Riegl VUX-1HA and ZF Profiler 9012) and two rear-looking cameras (two FLIR Flea2 5.0MP cameras). Each of the laser scanners has a single laser beam and delivers a 360^{o} horizontal field of view. The Riegl VUX-1HA and ZF Profiler 9012 can capture roughly one million points per second each with a range of 150 m (at an accuracy of ± 5 mm) and 120 m (at an accuracy of ± 2 mm), respectively (Riegl, 2019, ZF,2019). The sensors onboard the MLS are directly georeferenced by a NovAtel ProPak6 GNSS receiver and ISA-100C near-navigation grade IMU. The accuracy of derived GNSS/INS attitude after post-processing is 0.003° for the pitch/roll angles and 0.004° for the heading (yaw). The positional accuracy, on the other hand, is in the range of 0.01 to 0.02 m (Novatel, 2019). A rigorous system calibration procedure (Ravi et al, 2018) is used for the estimation of the mounting parameters – spatial and rotational offsets – between the GNSS/INS and laser scanning units. The system calibration parameters are estimated through minimizing the discrepancies between conjugate points, linear features, and planar features captured from different drive-runs.

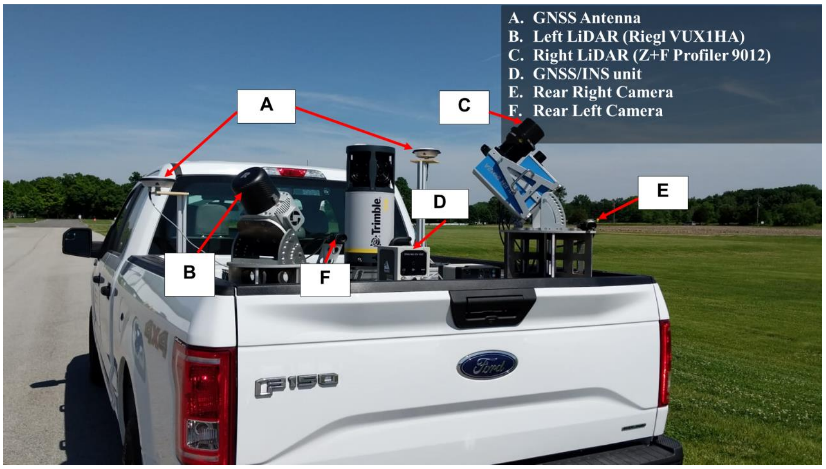

Figure 4.5. Configuration of the wheel-based mobile LiDAR mapping system used for the acquisition of point clouds along MSE walls

Two textured MSE walls in the state of Indiana were selected to illustrate the feasibility of the developed MLS and proposed processing strategy for deriving both standard (longitudinal and transversal angular distortions) and new performance measures introduced by Lin et al., (2019). Site-1 was selected to evaluate the capability of mobile LiDAR in inspecting an MSE wall by comparing the derived measures to those based on TLS. More specifically, TLS and MLS data were acquired for Site-1. A Faro Focus x330 TLS unit, which has a range accuracy of ± 2 mm at 25 m object distance, has been used for the data acquisition at Site-1 (Faro, 2013). It has a maximum range of 330 m while emitting close to one million pulses per second. This scanner provides color-coded point clouds using a built-in camera. More specifically, at a given location, the TLS performs two consecutive scans with the first one dedicated to acquiring the 3D point cloud, while the second scan captures successive images that are used for colorizing the individual points. For Site-2, the dataset, which is only captured by the MLS, is used to evaluate the performance of mobile LiDAR when dealing with large MSE walls. Figure 4.6(a) and Figure 4.6(b) show a photo of a portion of the textured MSE walls at Site-1 and Site-2, respectively. As it can be seen in Figure 4.6, both MSE walls have textured panels and are piece-wise planar façades (i.e., the façades cannot be modeled as a single planar surface).

The textured MSE wall at Site-1 was built in 2017 and is comprised of a single side with piece-wise planar façade. The total length along the MSE wall is approximately 175 m with a height of 4.5 m. The MSE wall facing consists of 85 rectangular precast textured concrete panels that are approximately 1.5 m by 3 m in size. The width of the panel joints for the size of the facing panel used in this wall is 19 mm (0.75 in.) as prescribed in the Indiana Department of Transportation standard specifications (INDOT, 2019). Two TLS scans were conducted in order to obtain full coverage of the MSE wall and mitigate any occlusions caused by vegetation and/or road furniture (e.g., light poles and signs). The MLS system drove forward and backward, as shown in Figure 4.7(a). The MLS dataset contains point clouds captured in the two drive runs at an average driving speed of 15 mph collected over almost 30 seconds. A sample of the collected point cloud is shown in Figure 4.8(a).

Figure 4.6(b) shows a photo of the MSE wall at Site-2. The wall was built in 2014 and has two sides (denoted hereafter as Side A and Side B) (see Figure 4.7(b)), with a length of 175 m and an average height of 7.5 m. The MSE wall has a total of 296 panels on Side A and 80 panels on Side B. Figure 4.7(b) shows the path of the vehicle travelled during the data collection. The dataset has four drive runs captured at an average driving speed of 25 mph over almost 30 second. The double drive runs in each driving direction as well as the forward and backward drive runs provide a redundancy, which could mitigate potential occlusions from nearby objects and degraded resolution from varying scanner-to-object distance. An example of the MLS point cloud for two drive runs at Site-2 is shown in Figure 4.8(b).

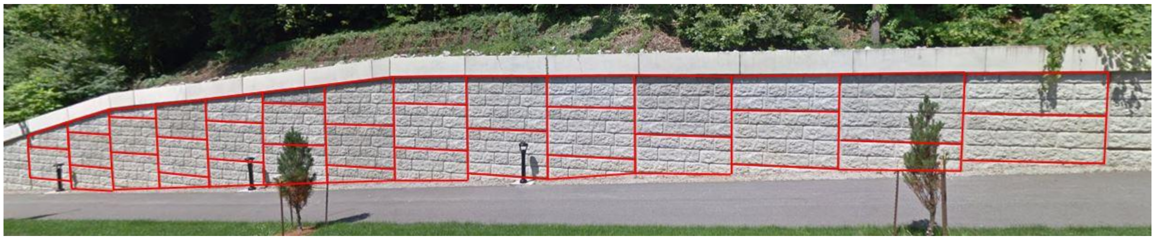

(a)

(b)

Figure 4.6. Sample photos of the textured MSE walls at different sites (a) Site-1 and (b) Site-2 (the different tiles are highlighted by the red rectangles).

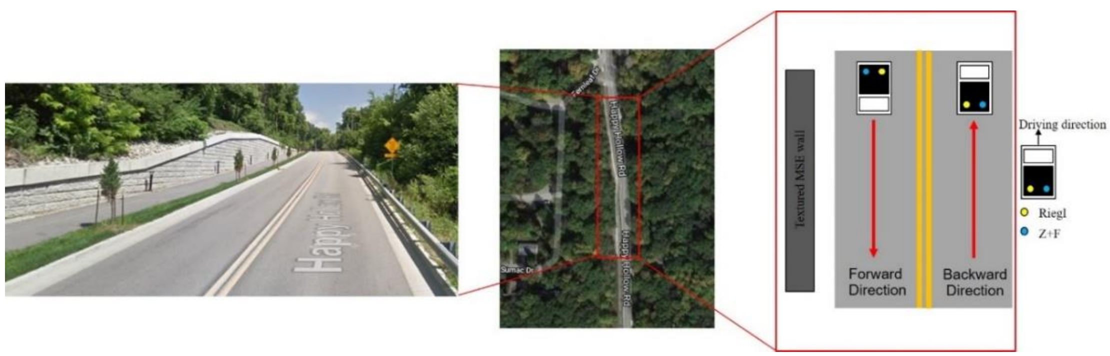

(a)

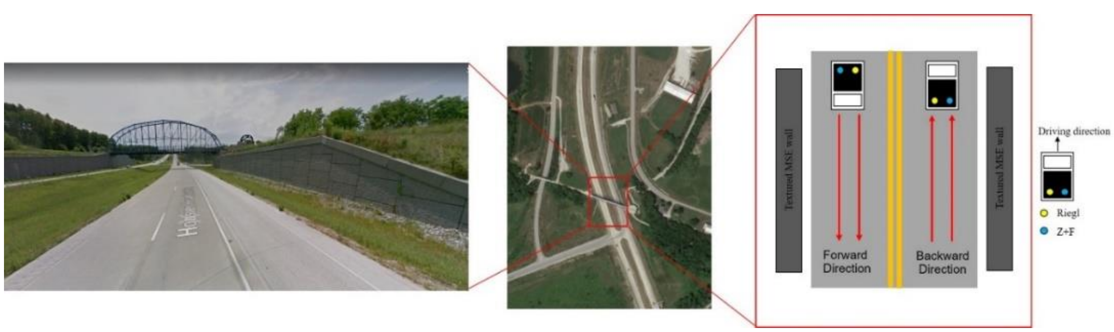

(b)

Figure 4.7. Location and drive-run configuration for the dataset collection in (a) Site-1 and (b) Site-2

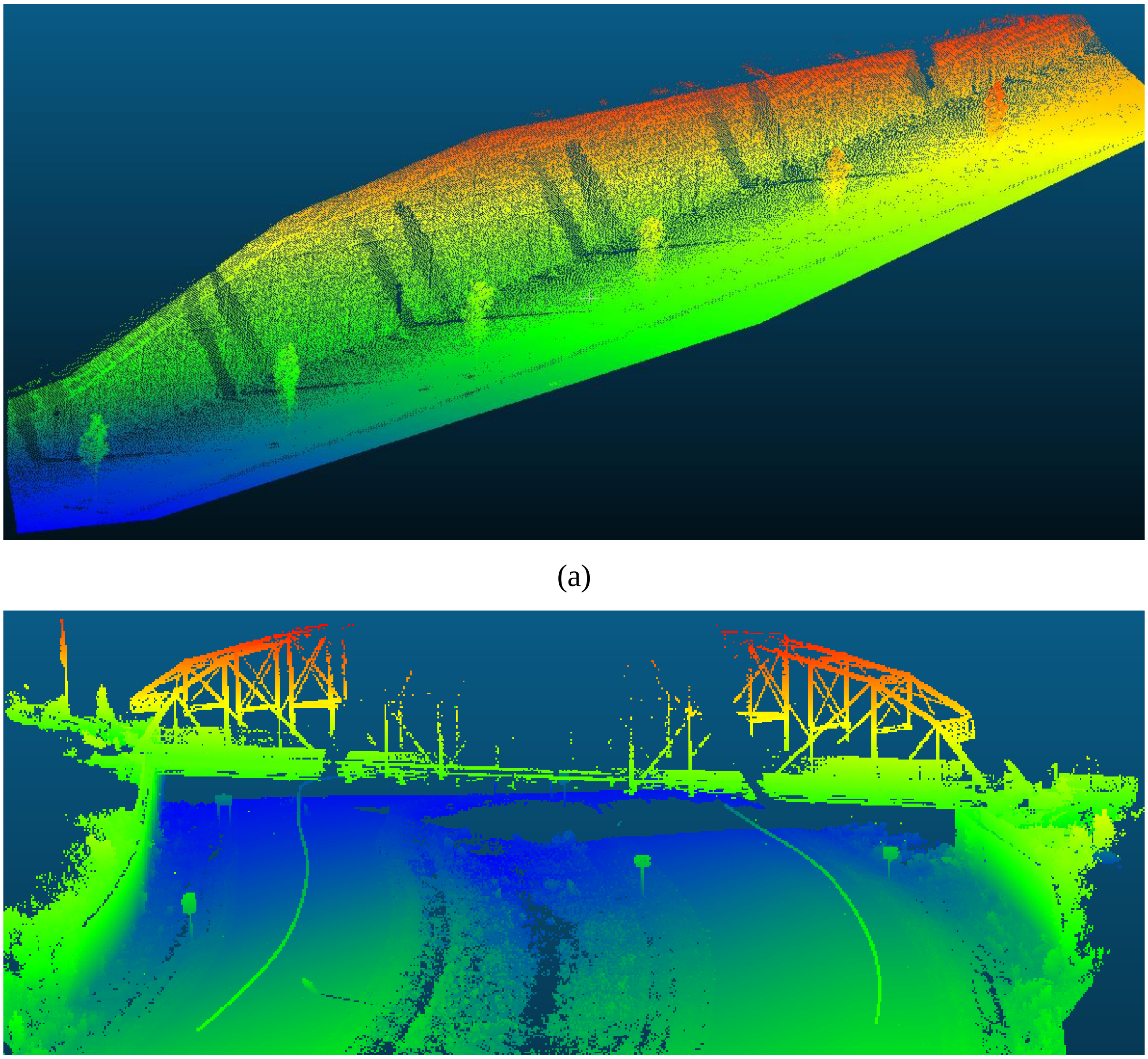

(a)

(b)

Figure 4.8.Textured MSE wall point cloud collected by the MLS dataset at (a) Site-1 and at (b) Site-2

4.5 Methodology

4.5.1 Conceptual basis of the proposed methodology

In this research, a scalable, systematic approach for MLS-based monitoring of large MSE walls with textured precast concrete panels is developed. A flowchart of the proposed procedure, comprising data acquisition, data processing, and estimation of performance/serviceability measures for MSE walls, is shown in

Figure 4.9. As previously mentioned, the standard serviceability measures, as proposed by AASHTO (2014), evaluate the longitudinal and transversal angular distortions of a given MSE wall face. The newly developed serviceability measures by Lin et al., (2019) provide the relative displacement and rotation of the individual panels relative to a Levelled Face coordinate system (LF_{cs}). The developed strategy is designed to be capable of handling MSE walls that have either smooth or textured precast concrete panels. Moreover, it can handle MSE walls with fully planar or piece-wise planar façades. Finally, the input point clouds to the processing methodology could be either from MLS or TLS data acquisition systems.

In order to derive the performance measures, the point clouds captured from different MLS drive runs or TLS scans need to be registered to a common reference frame. When using a TLS unit, acquiring several laser scans with significant overlap is a fundamental requirement for guaranteeing full coverage of the site of interest. The outcome from a TLS scan is a 3D point cloud referenced to a local coordinate system associated with the scanner's location and orientation. Hence, a registration process must be performed when dealing with multiple TLS scans in order to align them relative to a common reference frame.

Theoretically, registration is not necessary for point clouds acquired by an MLS since they are directly georeferenced through the onboard GNSS/INS unit. More specifically, the GNSS/INS trajectory, when combined with the system calibration parameters, produces the position and orientation of the laser scanners relative to the mapping frame (e.g., the UTM coordinate system with the WGS84 as the datum for horizontal coordinates and the National American Vertical Datum of 1988 – NAVD 88 – for vertical coordinate). Therefore, collected point clouds from different drive runs should be properly aligned as long as there is reliable trajectory data and access to accurate system calibration parameters. However, issues related to canopy cover, obstructions (e.g., tunnels and/or overhead bridges), GNSS-signal multipath interference from neighboring traffic, and platform speed could compromise the GNSS/INS trajectory would lead to alignment discrepancies between overlapping point clouds from neighboring drive runs. To take advantage of the available/complementary point cloud data from multiple drive runs, fine alignment must be ensured (i.e., a fine registration must be conducted to ensure the alignment of the point clouds from the different drive runs).

Regardless whether point clouds were acquired by TLS or MLS units, alignment must be ensured through a registration procedure. In general, registration strategies can be categorized into coarse and fine approaches (Al-Durgham at al., 2013). Since this research primarily utilizes MLS point cloud data, which is aligned to a high degree by the onboard GNSS/INS unit, we focus on fine registration. The point cloud fine registration strategy adopted in this research is discussed in more detail in Section 4.5.2.

Once the point clouds of the MSE wall in question have been accurately registered, we proceed the identification of individual planar segments of the wall. In other words, if an MSE wall is multi-face with planar individual faces as shown in Figure 4.4(a) or piece-wise planar facade as shown in Figure 4.4 (b), it should be partitioned into sections that are believed to be perfectly planar. Each planar section will be denoted hereafter as an MSE wall face. In this research, the identification/partitioning of MSE wall faces is conducted manually. The criterion for the fine-tuning of the partitioning process is based on the Root Mean Square Error (RMSE) of the normal distances between the constituent points from the corresponding best-fitting plane for the MSE wall face in question.

The next step is to define the coordinate systems associated with the MSE wall face (the Levelled Face coordinate system) as well as the individual panels (the Panel coordinate system). These coordinate systems are essential for determining the standard and new serviceability measures. The Levelled Face coordinate system (LF_{cs}) is defined by the local horizontal/vertical directions at the MSE wall site as well as the best fitting plane through the face in question, as depicted in Figure 4.10. More specifically, the Y-axis of the LF_{cs} is defined in a way that it belongs to the MSE wall face (as defined by the fitted plane parameters) and is parallel to the horizontal plane as described by the XY-plane of the defined mapping coordinate system at the site location. The Z-axis of the LF_{cs} is aligned along the vertical direction, i.e. the plumb line, at the MSE wall site. Finally, the X-axis of the LF_{cs} is derived to define a right-handed coordinate system. To facilitate the definition of the LF_{cs}, the geo-referencing parameters from the MLS have to be defined in a local mapping coordinate system with its Z-axis pointing in the local level (plumb line) direction at the MSE wall site location. The panel coordinate system (P_{cs}) defines the position and the orientation of individual panels, and it is essential for evaluating the relative displacement between the panels as well as the relative displacement/rotation between the panels and the Levelled Face coordinate system, LF_{cs}. As shown in Figure 4.10, the panel coordinate system is defined in such a way that two of its axes are aligned along the bottom and left sides of the bounding rectangle enclosing the panel. The X-axis of the panel coordinate system is derived to define a right-handed coordinate system (i.e., it is defined by the normal to the panel surface). A key component for reliable derivation of the serviceability measures is ensuring that the Panel coordinate system (P_{cs}) is defined in an identical manner for all the panels in a given face. To isolate the points making up the individual panels and define the Panel coordinate systems, Lin et al., (2019) adopted a region-growing segmentation procedure which utilizes the local point spacing and normal distance from the best-fitting plane to the MSE wall face as the similarity criteria. The underlying assumption for such segmentation is that excessive normal distances from the best-fitting plane correspond to the joints separating the individual panels. Nevertheless, such planar segmentation would not accurately isolate the individual panels for a textured wall as the joints among the panels might not be as distinguishable from the wall texture. In this research, a unique panel identification strategy has been developed to cope with the imposed challenge by working with a textured MSE wall. In this strategy, a region-growing segmentation is first applied to obtain an approximation of the individual panels. A template matching procedure is then performed to refine the panel extraction result, assuming that the individual panels are identical (i.e., the same form is used for panel casting). Section 4.5.3 describes the proposed face and panel extraction strategy in detail. Finally, after the coordinate systems are established and the individual panels are extracted, the performance measures can be derived. The derivation of the standard and new performance measures for textured MSE walls are presented in section 4.5.4.

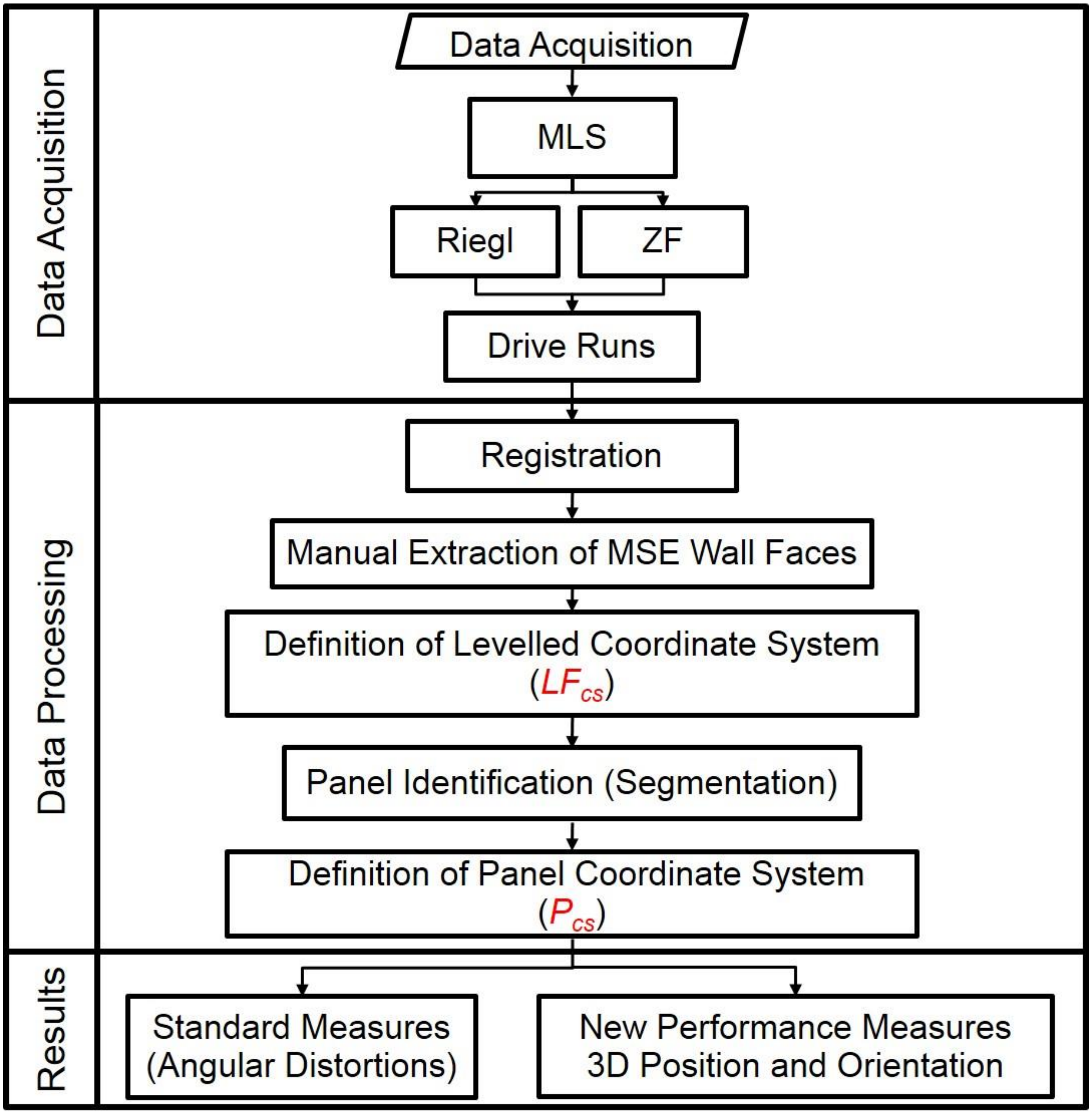

Figure 4.9 Flowchart of the proposed methodology

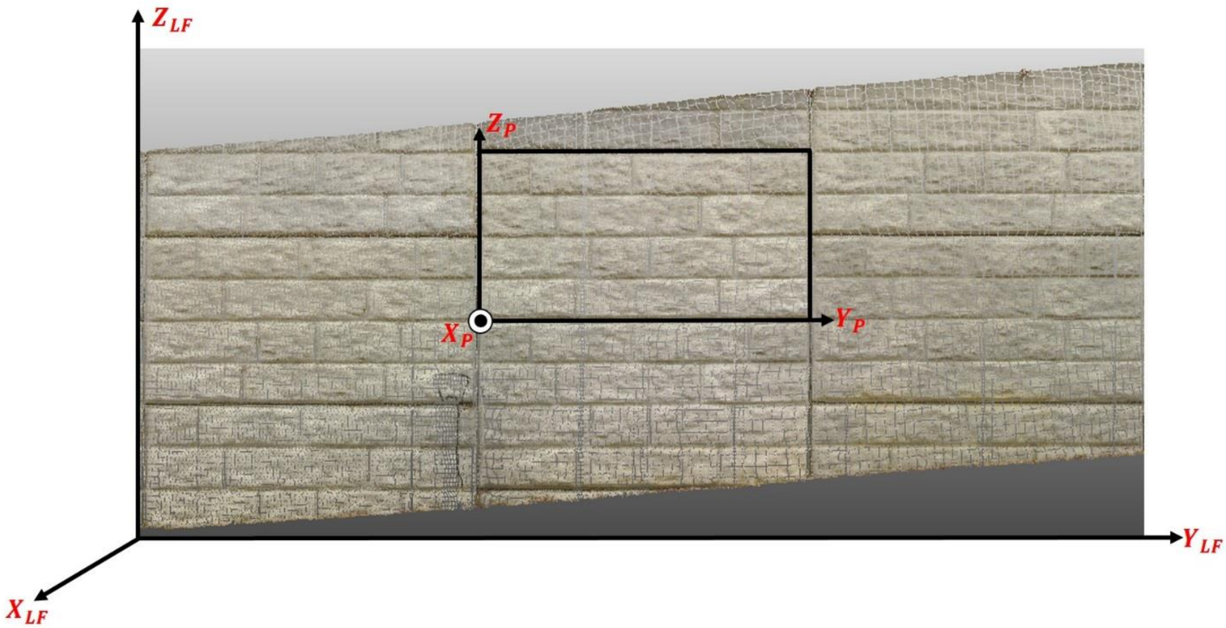

Figure 4.10. Illustration the Levelled Face Coordinate System (LF_{cs}) and Panel Coordinate System (P_{cs})

4.5.2 Registration of Point Clouds from Different MLS Drive Runs and TLS Scans

As mentioned earlier, the first step towards deriving the performance measures for an MSE wall is to ensure an accurate registration of LiDAR point clouds captured from different MLS drive runs or different TLS scans. A wide range of point cloud registration procedures have been proposed in the past few years. According to Habib and Al-Ruzouq (2004), a comprehensive registration paradigm should address four criteria: (1) transformation parameters relating the reference frames of the involved datasets, (2) registration primitives used for the estimation of the a comprehensive registration paradigm should address four criteria: (1) transformation parameters relating the reference frames of the involved datasets, (2) registration primitives used for the estimation of the transformation parameters, (3) mathematical constraints describing the similarity metric between conjugate primitives after registration, and (4) matching strategy controlling the framework for the automated identification of conjugate primitives. Due to the short duration for the acquisition of the point cloud from different MLS drive runs (e.g., less than thirty seconds for the involved case studies), a 6-parameter transformation (i.e., three shifts and three rotation angles – denoted here forth as X_T , Y_T , Z_T , Ω , Φ , and K) would be sufficient. The similarity metric could be based on constraining the distance between a point in one drive run and its corresponding point, which is established by the matching strategy, after the application of the transformation parameters to be zero. For fine registration, point primitives are recommended since the huge redundancy furnished by the size of the point cloud would ensure the highest accuracy possible for the estimated transformation parameters even though a point-to-point correspondence cannot be guaranteed in the data from different drive runs. Moreover, the similarity metric could be modified to handle point primitives without assuming point-to-point correspondence. Addressing the matching strategy is the last task to carry out the alignment process. The well-known Iterative Closest Point (ICP) (Besl and McKay, 1992) can establish the matches through iterative minimization of the squared sum of the point-to-point distances in the overlap area between the different drive runs. A better matching strategy that avoids the underlying assumption of having point-to-point correspondences is the Iterative Closest Patch (ICPatch) (ICPatch) (Habib et al., 2010), which is a variant of the ICP. Within the ICPatch, points in one drive run are matched to triangular patches in another drive run. These triangular patches could be derived through a Triangular Irregular Network (TIN) procedure. In this case, the matching strategy identifies point-patch pairs through the iterative minimization of the squared sum of the normal distances between such pairs. To avoid the TIN generation procedure, which could only handle surfaces with predominantly mild slopes, the Iterative Closest Projected Point (ICPP) was developed (Al-Durgham and Habib, 2013). In this case, the patch is defined by the closest three points in the second drive run to a transformed point from the first one using the current estimate of the transformation parameters. The matching strategy aims at identifying the matches and estimating the transformation parameters through the iterative minimization of the squared sum of the normal distances between the points in one drive run and their corresponding patch defined by the closest three points in the other drive run (Al-Durgham and Habib, 2013).

In this research, a modified matching strategy, which is a hybrid implementation of the ICPatch and ICPP, is used. More specifically, the procedure starts with an approximate estimate of the transformation parameters between the captured point clouds from different drive runs. Given that these point clouds are aligned to a high degree through the onboard GNSS/INS, zero shifts and zero rotation angles could be used as the initial values for the transformation parameters. Such parameters are used to transform a point from one drive run - denoted as the source surface- to the reference frame of the other drive run - denoted as the reference surface. The transformed point (P_t) will be used to identify the three closest points in the reference surface. The closest three points will be accepted as a possible match if (P_t) belongs to a bipyramid formed by these points and two vertices that belong to the orthogonal to the triangle defined by these three points through its centroid given a predefined normal distance threshold (Figure 4.11). The normal distance threshold (n) is selected based on the noise level within the data. Rather than minimizing the squared sum of the distances between the transformed point and its projection onto the corresponding triangle (which is implemented in the ICPP), this research utilized the modified weigh function proposed by the ICPatch for the estimation process. For more details regarding the modified weight function, interested readers can refer to (Habib et al., 2010).

Compared to the original ICPatch and ICPP procedures, the advantages of the hybrid approach include a higher computational efficiency, less sensitivity to the existence of erroneous points (i.e., outliers), and capability of registering vertical surfaces, which cannot be effectively handled in the original ICPatch. An example of the outcome from the point cloud registration is shown in Figure 4.12, where two TLS scans at Site-1 are registered together with the MLS point clouds from different drive runs.

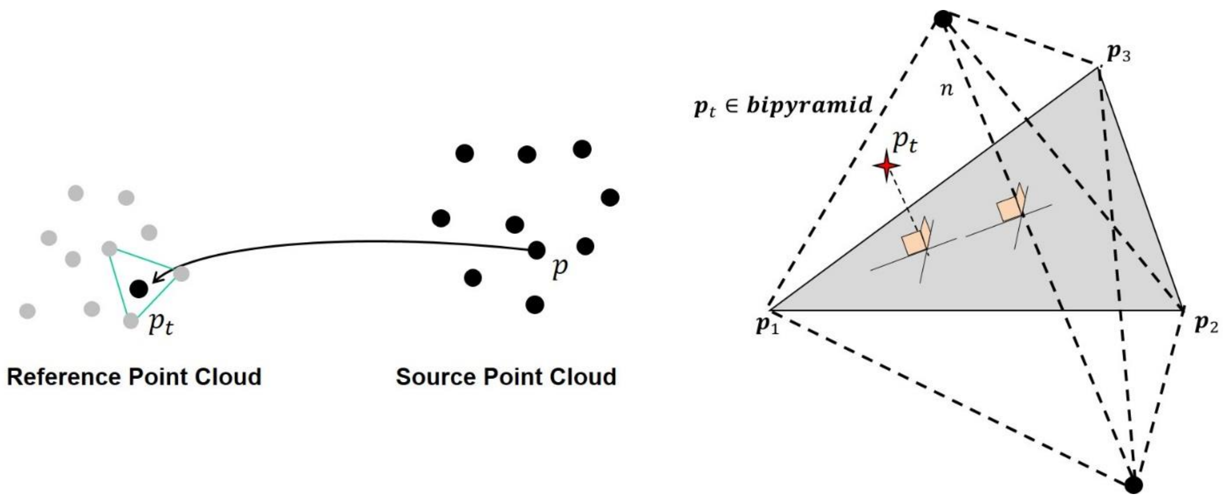

(a) (b)

Figure 4.11. (a) Transformation from source point cloud to reference point cloud, and (b) conditions to accept the point-to-patch correspondence between the two point clouds

Figure 4.12 Point Cloud Registration of TLS dataset (colored by the RGB values from the TLS camera) and the MLS dataset (colored by intensity)

4.5.3 MSE wall face and panel extraction

In this section, a semi-automated procedure is introduced to extract the faces and the panels of the MSE wall. First, the MSE wall needs to be divided into individual faces that can be considered as planar segments (see Figure 4.13). The sectioning process is conducted manually and the planarity of each individual MSE wall face is examined by applying a plane fitting to the constituent points. A sectioning/partitioning would be accepted if the Root Mean Square Error (RMSE) of the normal distance of the points from the best-fitting plane through this section is below a threshold that depends on the noise level in the data and the texturing detail in the panels. Once the individual faces are established, one can proceed with defining the Levelled Face coordinate system (LF_{cs}) as explained in Section 4.3. Then, a region-growing segmentation technique is applied to segment the points comprising the individual panels as described by Habib and Lin (2016). The similarity criteria for the region growing process include the local point spacing and normal distance between the points and the fitted plane through the face. For a smooth MSE wall face, such criteria can effectively segment the individual panels, and the Panel coordinate system (P_{cs}) is simply defined by identifying the Minimum Bounding Rectangle (MBR) enclosing the segmented panels, as proposed Lin *et al*., (2019). Defining the panel coordinate system in a unique manner for textured MSE walls is much more challenging. The planar segmentation technique mentioned above would not isolate the individual panels in a unique way as the joints among the panels could not be easily identified as out of plane features since their normal distances could be within the texture level of the wall (for example see Figure 4.14). Moreover, existing occlusions could also affect the segmentation of the complete panels as shown in Figure 4.15. Therefore, a strategy based on template matching to refine the initial panel segmentation result and uniquely define the Panel coordinate system (P_{cs}) is proposed. The initially segmented panels are used to extract the approximate corners, which represent the enclosing rectangle, of the individual panels through a search procedure starting from virtual points that are defined by the minimum/maximum coordinates of the segmented points. These corners are then utilized to define an approximate P_{cs} for the individual panels and to isolate the point clouds pertaining to the individual panels. Due to the subjectivity of the segmentation procedure and consequently the defined panel corners, one cannot assume that the P_{cs} is defined in a unique manner for the different panels. To resolve this issue, a panel matching procedure is carried out while assuming that the individual panels are identical (i.e., the same form is used for panel casting). More specifically, a master panel is selected and used as a template for a panel matching procedure. The master panel is denoted as the "template panel" with its P_{cs} denoted as $(x_{p_t}, y_{p_t}, z_{p_t})$. The remaining panels are denoted as "matching panels" with their approximate P_{cs} denoted as $(x_{p_{m\_a}}, y_{p_{m\_a}}, z_{p_{m\_a}})$. The template and matching P_{cs} are defined using the corners of the respective panels (i.e., the origin is defined at the lower left corner of the segmented panel; the Y and Z axes are defined by the lines connecting the lower corners and left corners, respectively; and the X-axis defines a right-handed coordinate system). To identify the panels' corners in a unique manner, the points enclosed by the template and matching panels undergo a registration procedure using the modified ICPatch to estimate the shifts and rotations – as seen in equation (1) – relating the template P_{cs} and approximate matching P_{cs}. In this equation, *i* is the index of a point that have been matched in the template and matching panels – denoted by *k*.

$$r_i^{p_{m\_a\_k}} = r_{p_t}^{p_{m\_a\_k}} + R_{p_t}^{p_{m\_a\_k}} r_i^{p_t} \quad (4.1)$$

where:

$r_i^{p_{m\_a\_k}}$: are the coordinates of point *i* relative to the approximate matching P_{cs} for the kth panel.

$r_{p_t}^{p_{m\_a\_k}}$: are the shifts between the template Pcs and the approximate matching P_{cs} for the kth panel.

$R_{p_t}^{p_{m\_a\_k}}$: is the rotation matrix between the template Pcs and approximate matching P_{cs} for the kth panel.

$r_i^{p_t}$: are the coordinates of point i relative to the template P_{cs}.

Following the estimation of the shifts and rotations relating the template P_{cs} and approximate matching P_{cs}, the parameters can be utilized to derive the corners for the matching panels which correspond to those used for defining the template panel as shown in

Figure 4.16. Using these corners, the P_{cs} is defined in a unique manner for all the panels along the MSE wall.

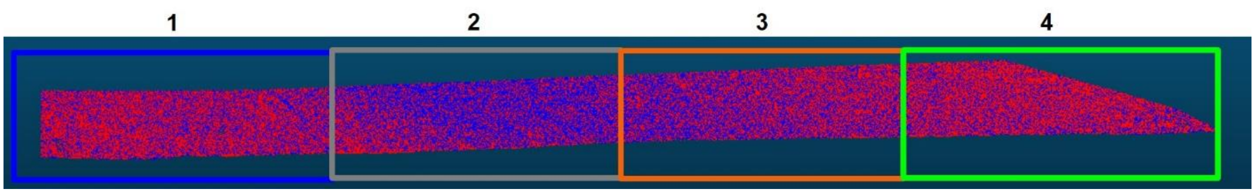

Figure 4.13 An example of manual extraction of the faces along an MSE wall with piece-wise planar façade (different colors along the MSE wall represent the different registered scans)

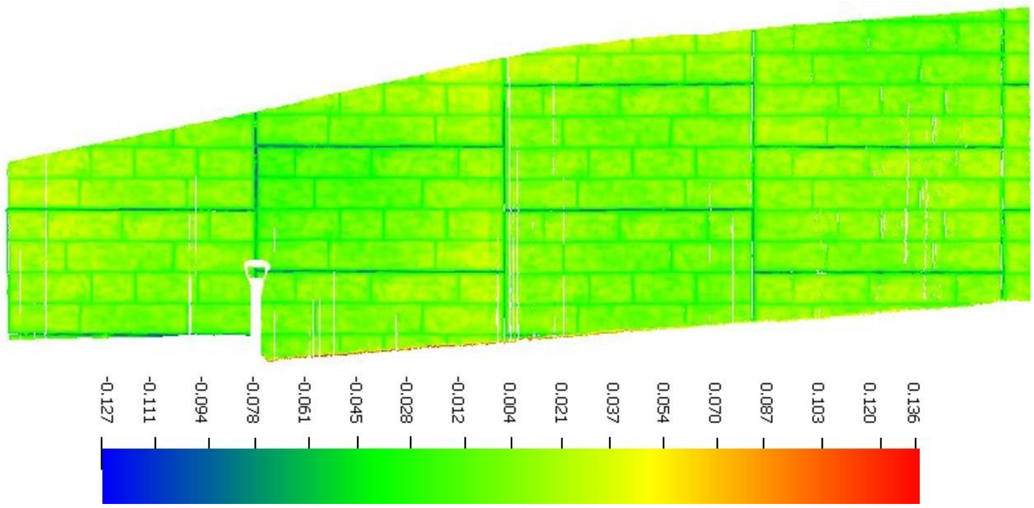

Figure 4.14. Normal distance map for a given face illustrating the fact that joints among the panels could be distinguished through their normal distance from the best fitting plane to that face (units for the values along the scale bar are in meters)

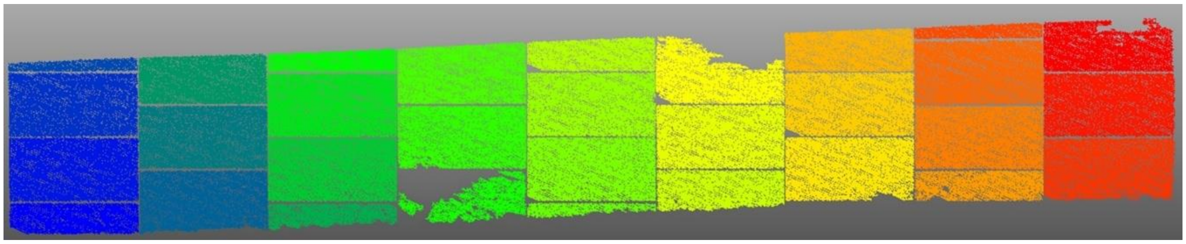

Figure 4.15. An example of segmented textured MSE wall panels (different colors represent different segmented panels)

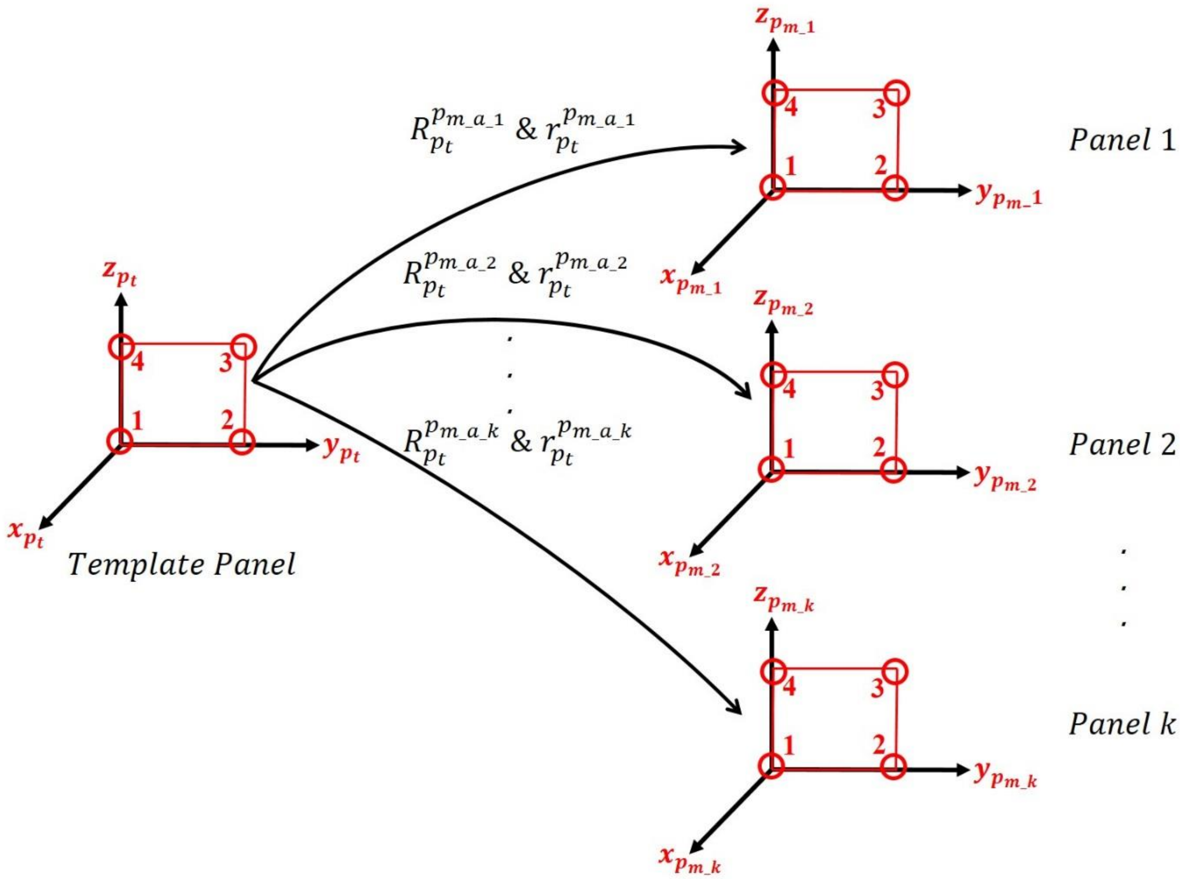

Figure 4.16. Refined panel coordinate system (P_{cs}) through the estimated transformation parameters relating the template and matching panels

4.5.4 MSE Derivation of standard and new serviceability measures

The standard serviceability measures include the longitudinal angular distortions (α_L) and the transversal angular distortions(α_T). The derivation of such measures is based on establishing longitudinal and transversal lines along the MSE wall face in question. The longitudinal lines are established using the corners of the horizontal edges of all the panels adjacent to these lines by applying a line fitting technique. Once the line parameters (i.e., directional vector of the 3D line) are estimated, a dot product between the directional line parameters and Y-axis components of the LF_{cs} is used to obtain the longitudinal angular distortion (α_L). The transversal lines for the columns of panels are derived using the midpoints of the horizontal edges of the uppermost and the lowermost panels of a given column. Then, a dot product of a vector connecting the midpoints of the uppermost and the lowermost panel edges and the Z-axis components of the LF_{cs} is performed to obtain the transversal angular distortion (α_T). An example of the longitudinal and transversal lines used for a planar face of the MSE wall at Site-1 is illustrated in Figure 4.17.

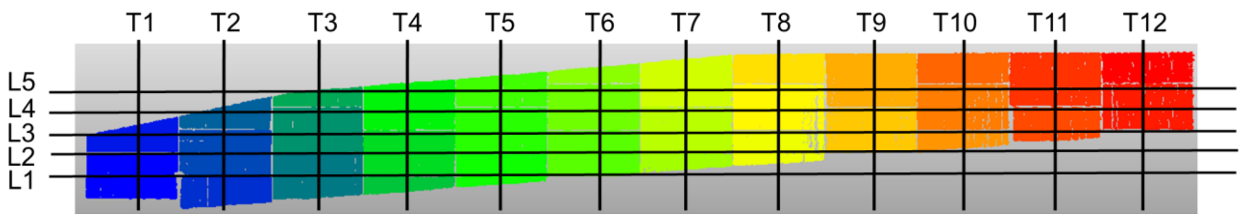

Figure 4.17. Longitudinal and transversal lines used to define the angular distortions for a planar face of the MSE wall at Site-1

The recently developed serviceability measures by Lin *et al*., (2019) evaluate the relative displacement and rotations of a panel relative to the Levelled Face coordinate system (LF_{cs}). To derive these serviceability measures, the spatial and rotational relationships between the LF_{cs} and P_{cs} as seen in Figure 4.18 are utilized. More specifically, the location of the origin of the P_{cs} relative to the LF_{cs} – denoted as X_o, Y_o, and Z_o – defines the panel position. The rotation angles – denoted as θ_{xp}, θ_{y_P}, and θ_{z_P} – that need to be applied to the LF_{cs} to make it parallel to the P_{cs} are used to define the panel orientation. The final measure is the normal distances between the corners of each panel and the fitted planes through the corners of neighboring panels. Using the derived corners from the template matching procedure, one can derive these normal distances as shown in Figure 4.19. In this figure, eight normal distances – denoted by the red lines – from the four corners of panel 4 to neighboring panels can be estimated (i.e., panels 1, 2, 3, 5, 6, and 7). One should note that using the corners enclosing the panels to define the panel position, orientation, and displacement would exclude the panel texture from impacting the derived measures.

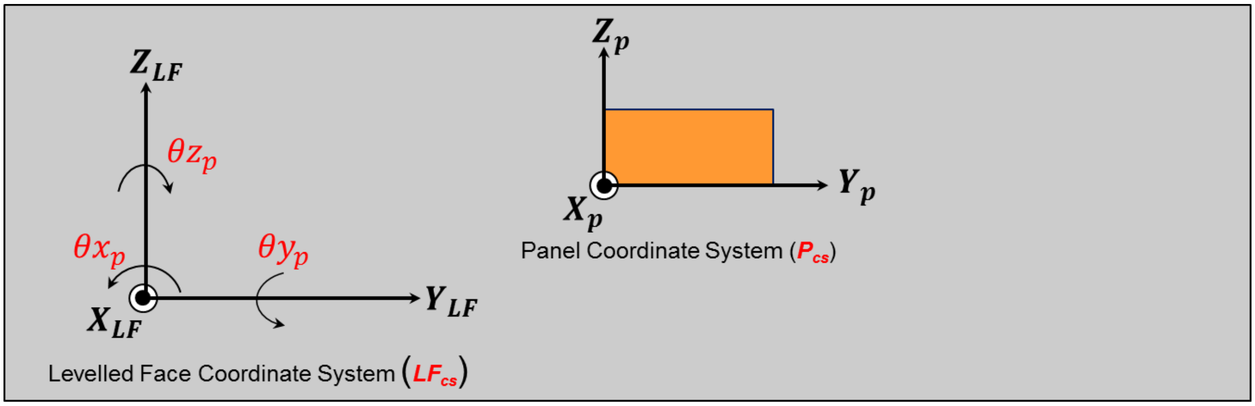

Figure 4.18. Illustration of the relationship between LF_{cs} and P_{cs} for deriving the panel position and orientation serviceability measures

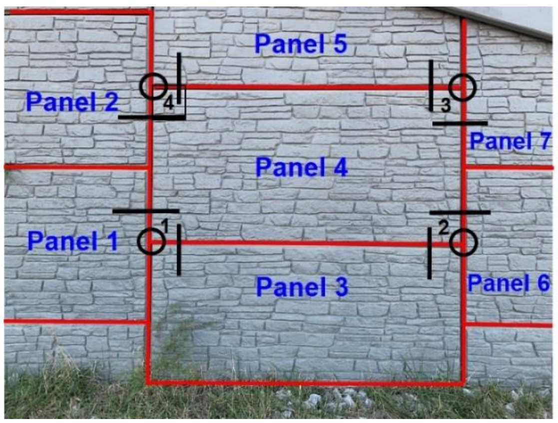

Figure 4.19 Evaluation of panel-to-panel out of-plane displacement

4.6 Experimental Results

Two case studies were carried out to evaluate the capability of the MLS in monitoring MSE walls with textured precast concrete panels. The case study at Site-1 validates the MLS derived measures by comparing them against those derived from TLS dataset. The case study at Site-2 further highlights the capability of the MLS by applying the proposed strategy for inspecting a large textured MSE wall.

4.6.1 Experimental Results for Site-1

LiDAR point cloud alignment

Point cloud registration was performed to register i) MLS point clouds from the two scanners onboard the data acquisition system in a given drive run, ii) the MLS point clouds from two drive runs, iii) the TLS point clouds from two scans, and iv) the MLS and TLS point clouds. The estimated transformation parameters relating the derived point clouds from the two MLS scanners in a given drive run can be used to evaluate the quality of the system calibration procedure (i.e., significant deviations from zero shifts and zero rotation is an indication of residual artifacts in the system calibration parameters). The estimated transformation parameters between the point clouds from different drive runs were used to quantitatively evaluate the quality of the GNSS/INS trajectory (i.e., significant deviations from zero shifts and zero rotation is an indication of inferior quality of the GNSS/INS trajectory). The registration of the TLS and MLS point clouds is done to ensure that there are uniquely defined local vertical and local horizontal directions within the study site.

To evaluate the comparative performance of TLS-based and MLS-based inspection strategies, the experimental results for this dataset focused on a single face of the wall that has 32 panels. As already mentioned, this research had two MLS drive runs in opposite directions covering the MSE wall. For the MLS registration process, a total of three registration steps are conducted. The first and second steps involved the registration of the Riegl and ZF scans in each drive run. The third step performed the alignment between the combined/registered scans from the two drive runs. For the TLS, the two scans were registered. Finally, the TLS and MLS point clouds were registered to a common reference frame defined by the latter.

Figure 4.20 to Figure 4.23 qualitatively illustrate the point cloud alignment of the derived point clouds from the two scanners in a given run, point clouds from two different runs in opposite directions, point clouds from the two TLS scans, and point clouds from TLS and MLS units. In each of these figures, four vertical profiles were manually extracted to illustrate the alignment quality. These profiles exhibit an overall alignment, which is commensurate with the expected accuracy range of the individual system, between point clouds from the scanners in a given drive run, two drive runs, two TLS scans, and the TLS/MLS units.

Table 4.2 to Table 4.5 show the respective transformation parameters along with the square root of a-posteriori variance factor ($\hat{\boldsymbol{\sigma}}_{\circ}$) and average/root mean square error (RMSE) of the normal distances between the registered point clouds in Figure 4.20 to Figure 4.23. Close inspection of Figure 4.20 to Figure 4.23 and Table 4.2 to Table 4.5 reveals the following:

1. The estimated magnitude of the transformation parameters necessary for the alignment of the Riegl and ZF scanner point clouds indicates the high quality of the system calibration as indicated by small values of these parameters (the estimated parameters are in the range of 2 cm and 0.02°).
2. The estimated transformation parameters necessary for the alignment of the MLS point clouds from different drive runs indicate the presence of some discrepancies between these point clouds in the range of 3 to 5 cm and -0.01° to 0.19°. These are mainly caused by the impact of environmental factors on the GNSS/INS trajectory derivation.
3. The reported square root of a-posteriori variance factor ($\hat{\boldsymbol{\sigma}}_{\circ}$) and average/root mean square error (RMSE) of the normal distances between conjugate primitives for the different point clouds show the alignment quality following the registration process (i.e., in the 1 to 2 cm range).

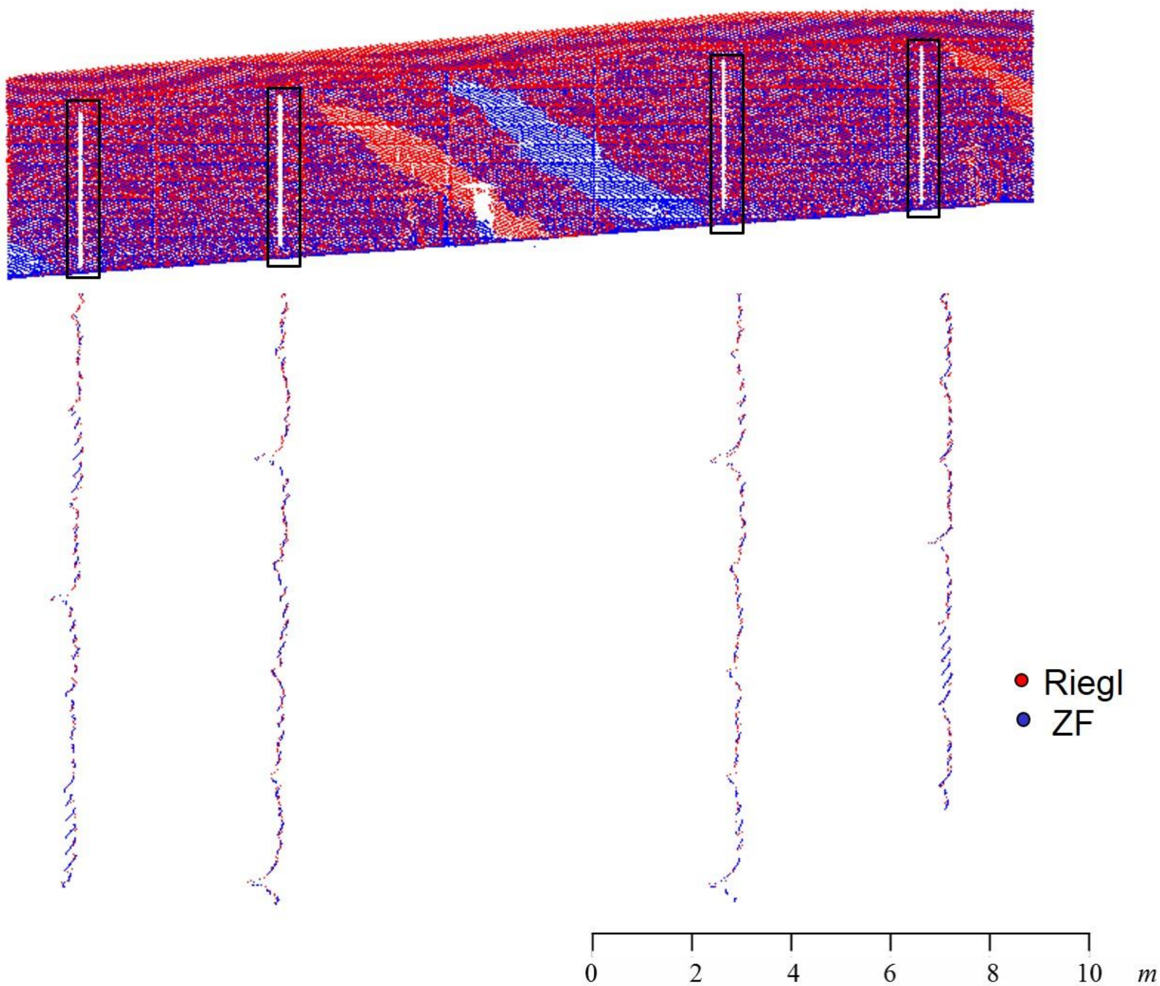

Figure 4.20. Cross sections illustrating the alignment quality of registered Riegl and ZF scans from a given drive run for the MSE wall at Site-1

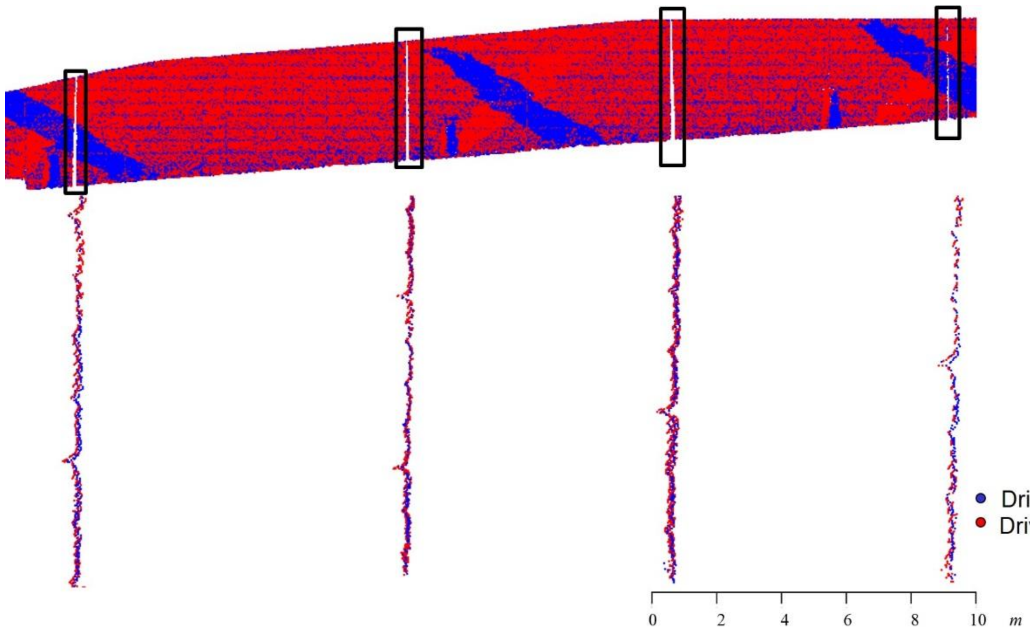

Figure 4.21. Cross sections illustrating the alignment quality of registered point clouds from the two MLS drive runs for the MSE wall at Site-1

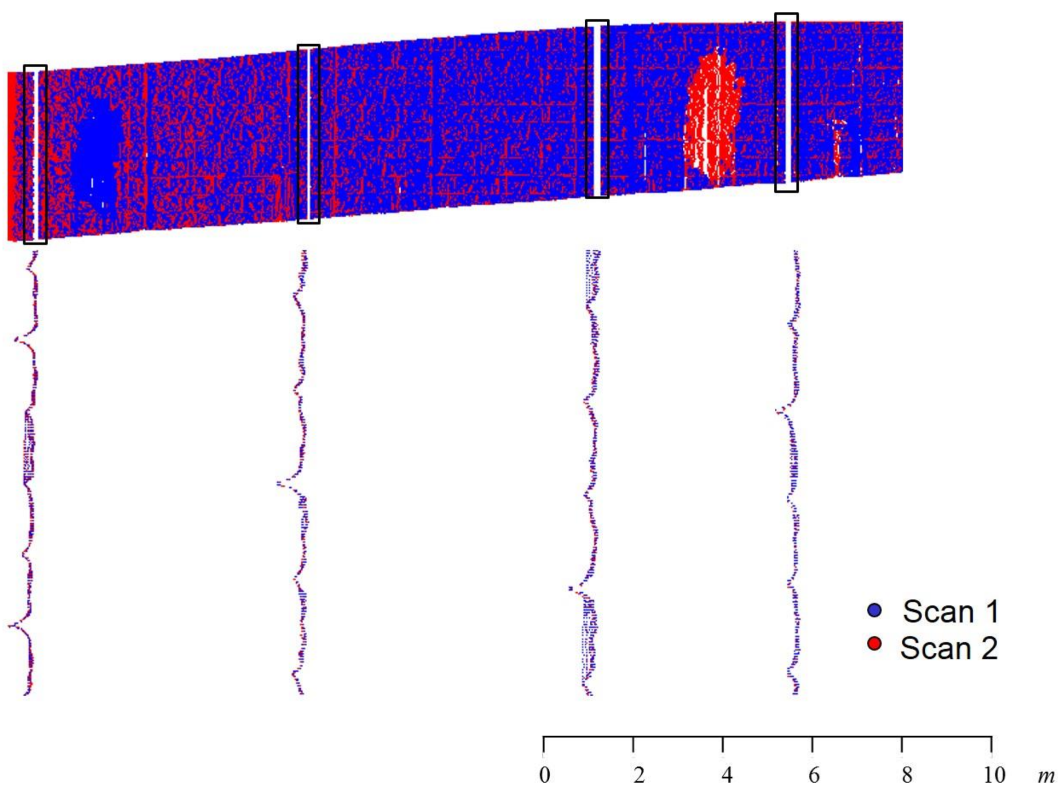

Figure 4.22. Cross sections illustrating the alignment quality of registered TLS scans of the MSE wall at Site-1

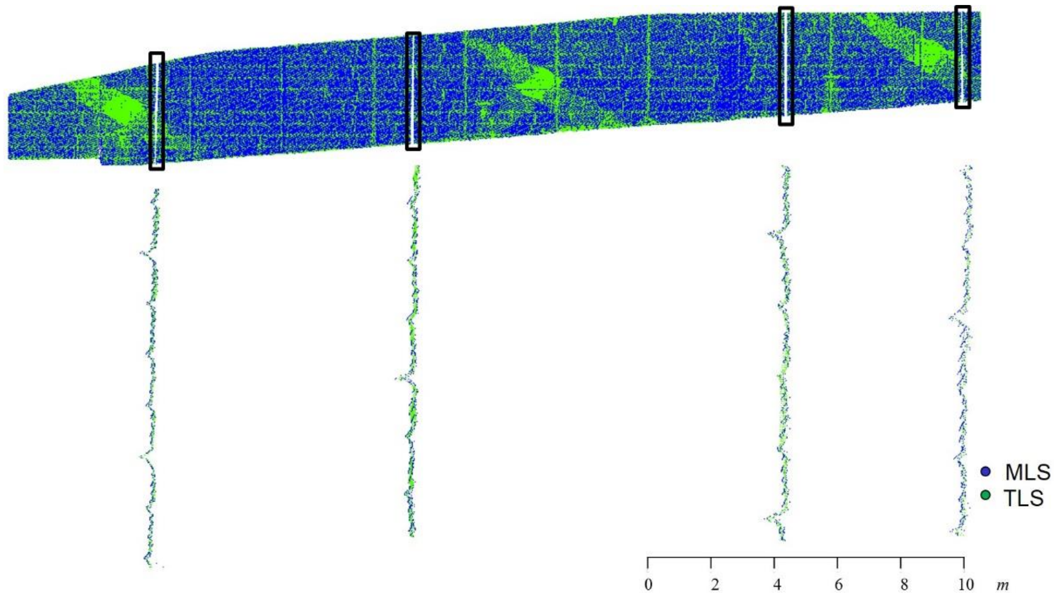

Figure 4.23. Cross sections illustrating the alignment quality of registered TLS and MLS point clouds for the MSE wall at Site-1

Table 4.2. Estimated transformation parameters and quality measures (square root of a-posteriori variance factor, average normal distance among point-patch pairs, and RMSE of the normal distances) following the registration of the Riegl and ZF scans in a given drive run at Site-1

X_T (*m±mm*)	Y_T (*m±mm*)	Z_T (*m±mm*)	Ω (deg±sec)	Φ (deg±sec)	Κ (deg±sec)	$\hat{\sigma}_o$ (m)	Average Normal Dist. (m)	RMSE (m)
0.020	0.010	0.005	-0.0012	0.022	0.0003	0.0024	0.0023	0.0032
±0.01	±0.03	±0.02	±0.003	±0.029	±0.004			

Table 4.3. Estimated transformation parameters and quality measures (square root of a-posteriori variance factor, average normal distance among point-patch pairs, and RMSE of the normal distances) following the registration of the MLS point clouds from different drive runs at Site-1

XT (m±mm)	YT (m±mm)	ZT (m±mm)	Ω (deg±sec)	Φ (deg±sec)	Κ (deg±sec)	$\hat{\sigma}_o$ (m)	Average Normal Dist. (m)	RMSE (m)
-0.058	0.032	0.035	-0.012	0.189	0.009	-0.058	0.032	0.035
±1.04	±0.270	±0.410	±0.018	±0.120	±0.011			

Table 4.4. Estimated transformation parameters and quality measures (square root of a-posteriori variance factor, average normal distance among point-patch pairs, and RMSE of the normal distances) following the registration of the TLS scans at Site-1

XT (m±mm)	YT (m±mm)	ZT (m±mm)	Ω (deg±sec)	Φ (deg±sec)	Κ (deg±sec)	$\hat{\sigma}_o$ (m)	Average Normal Dist. (m)	RMSE (m)
-0.817	13.11	-0.722	0.04	0.01	1.06	0.003	0.0048	0.005
±2.91	±4.02	±1.34	±0.418	±0.302	±0.220			

Table 4.5. Estimated transformation parameters and quality measures (square root of a-posteriori variance factor, average normal distance among point-patch pairs, and RMSE of the normal distances) following the registration of the MLS and TLS point clouds at Site-1

XT (m±mm)	YT (m±mm)	ZT (m±mm)	Ω (deg±sec)	Φ (deg±sec)	K (deg±sec)	$\hat{\sigma}_{\circ}$ (m)	Average Normal Dist. (m)	RMSE (m)
0.641	0.431	-0.181	-0.066	0.341	1.67	0.010	0.0052	0.008
±1.70	±0.39	±0.70	±0.032	±0.170	±0.018			

Serviceability measures

Figure 4.24 illustrates the longitudinal and transversal angular distortions for the textured MSE wall planar face (TLS in green and MLS in blue) as well as the recommended tolerable angular distortions (denoted by the red lines). These angular distortions are evaluated using the longitudinal and transversal lines in Figure 4.17. The horizontal line in Figure 4.24 (a) represents the tolerable longitudinal distortions for a joint width of 19 mm (0.75 in.), while the horizontal lines in Figure 4.24(b) represent the tolerable transversal angular distortions, as prescribed in AASHTO (2014). Figure 4.24 reveals that the angular distortions (both longitudinal and transversal) obtained from the MLS closely resemble those derived using the TLS. This confirms the capability of mobile LiDAR in achieving high quality assessment of the standard serviceability measures. As far as the MSE wall evaluation is concerned, Figure 4.24(a) and Figure 4.24(b), show that this wall satisfied the longitudinal angular distortion criterion for a joint width of 19 mm (0.75 in.). However, it failed to meet the tolerable transversal angular distortion criterion of 1/240. As for the recently available serviceability measures, the estimated values (namely, the position of the most lower left corner of each panel – X_o, Y_o, and Z_o – and the angular orientation of each panel – θ_{x_P}, θ_{y_P}, and θ_{z_P}– relating the P_{cs} and LF_{cs} coordinate systems) are listed in Table 4.6 for TLS and MLS, respectively. For a perfectly constructed MSE wall, the X-coordinate of the origin of the P_{cs} relative to the LF_{cs}, denoted as X_o, should be close to zero. Moreover, the YZ- coordinates of the origin of the P_{cs}, denoted as Y_o and Z_o, should reflect the dimensions of the panels as well as the gap between the panels along the width and height directions, respectively. The position of the panel can be used to detect potential relative movements among the panels in a given face. Such movement can be identified and quantified through repetitive scans over time. The second set of measures is the angular rotations representing the relationship between the LF_{cs} and P_{cs}. As mentioned earlier, the rotation angles θ_{x_P}, θ_{y_P}, and θ_{z_P} represent the rotations that need to be applied to the LF_{cs} until it is parallel to the P_{cs}. More specifically, θ_{y_P} and θ_{z_P} can be viewed as rotations of the panel out of the LF_{cs}, while θ_{x_P} represents a rotation in the plane of the panel. For a perfectly constructed MSE wall, these rotation angles should be as close to zero as possible. Although it is instructive to inspect the data provided in Table 4.6 for the 32 panels constituting the textured MSE wall face in question, a graphical summary is much more intuitive for identifying trends and outliers. Figure 4.25 shows the Cumulative Distribution Functions (CDF) for the three angular values (θ_{x_P}, θ_{y_P}, and θ_{z_P}) and the panel-to-panel normal distance of TLS and MLS datasets. Table 4.7 provides summary statistics of the proposed serviceability measures for the investigated 32 MSE wall panels using TLS and MLS point clouds, respectively. For TLS-based derivation measures, the 95th percentile values of angular tilts (θ_{x_P}, θ_{y_P}, and θ_{z_P}) are 0.62°, 0.15°, and 0.63°, respectively. These values almost agree with same measures derived from MLS-based. For the TLS/MLS comparative evaluation, Table 4.8 shows the statistics of the differences between the TLS-based and the MLS-based serviceability measures. In this table, it can be concluded that MLS-based similarity measures are within 5 cm and 0.5° when compared to those from TLS.

(a)

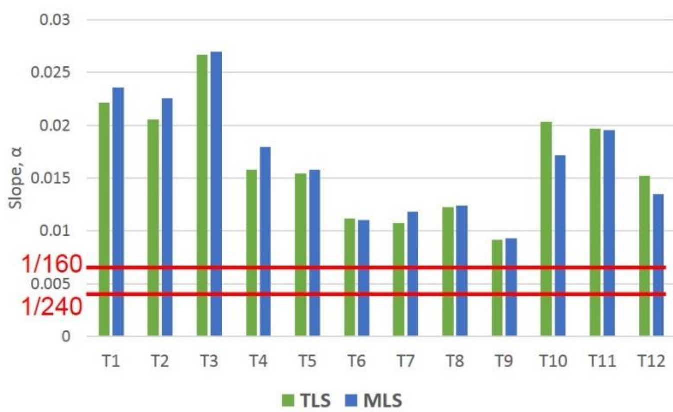

(b)

Figure 4.24. Angular distortion for the textured MSE wall face at Site-1: (a) longitudinal angular distortion along lines L1-L5, and (b) transversal angular distortion along lines T1-T12 (the horizontal lines represent the tolerable angular distortions) – L1-L5 and T1-T12 are illustrated in Figure 4.17

Table 4.6. TLS-based and MLS-based panel parametrization for the textured MSE wall at Site-1

ID	X_o (m)	Y_o (m)	Z_o (m)	θ_{xp} (deg.)	θ_{yp} (deg.)	θ_{zp} (deg.)	X_o (m)	Y_o (m)	Z_o (m)	θ_{xp} (deg.)	θ_{yp} (deg.)	θ_{zp} (deg.)
1	0.08	-0.38	0.06	0.00	0.00	-0.38	0.05	-0.35	0.00	0.00	0.00	-0.33
2	0.13	-0.38	1.55	0.01	-0.89	-0.21	0.11	-0.34	1.50	-1.92	-0.83	0.13
3	0.10	2.65	-0.32	0.46	-0.80	-1.11	0.08	2.66	-0.02	0.67	-1.36	-0.94
4	0.12	2.61	0.81	0.02	-1.06	-1.26	0.08	2.64	0.76	0.20	-1.19	-1.43
5	0.14	2.62	2.32	-0.64	1.06	-1.04	0.11	2.65	2.27	-0.43	0.67	-1.08
6	0.16	5.61	0.03	0.62	-0.43	-0.57	0.13	5.63	-0.02	0.62	-0.51	-0.58
7	0.18	5.61	1.53	0.54	-0.42	-0.76	0.16	5.63	1.48	0.50	-0.61	-0.70
8	0.23	5.61	3.02	-0.17	2.04	-0.35	0.20	5.64	2.98	0.01	1.12	-0.36
9	0.21	8.41	0.15	0.09	-3.78	-0.79	0.19	8.60	-0.06	0.86	-1.67	-0.54
10	0.20	8.57	0.78	0.17	-0.02	-0.87	0.18	8.62	0.73	0.28	-0.11	-0.79
11	0.25	8.58	2.29	0.10	-1.06	-0.60	0.23	8.63	2.24	0.41	-1.25	-0.55
12	0.25	11.58	0.40	0.34	-0.88	-0.42	0.22	11.62	0.36	-0.24	-0.61	-0.27
13	0.27	11.57	1.52	0.21	-0.43	-0.08	0.24	11.60	1.47	0.10	-0.52	-0.11
14	0.30	11.58	3.02	0.34	-1.05	-0.07	0.28	11.61	2.98	-0.31	-1.14	0.05
15	0.27	14.56	0.77	0.46	-0.62	0.05	0.25	14.61	0.73	0.62	-0.89	0.25
16	0.29	14.56	2.28	0.37	-1.24	-0.06	0.27	14.61	2.23	0.66	-1.35	0.12
17	0.29	14.58	3.77	0.30	0.00	0.01	0.28	14.63	3.74	-1.84	-1.00	0.09
18	0.28	17.56	0.76	0.92	-1.44	0.21	0.25	17.62	1.01	-0.24	0.20	0.28
19	0.28	17.56	1.54	0.24	-0.59	-0.08	0.25	17.62	1.50	0.28	-0.79	-0.07
20	0.30	17.56	3.04	0.30	-1.19	-0.06	0.28	17.61	2.99	0.57	-1.54	-0.01
21	0.27	20.55	1.11	1.54	-0.42	0.30	0.24	20.55	1.10	-1.73	-0.33	0.30
22	0.30	20.55	2.28	0.01	-0.71	0.26	0.27	20.59	2.24	-0.15	-0.91	0.28
23	0.31	20.55	3.78	-0.65	-1.68	0.10	0.29	20.60	3.73	-0.28	-2.04	0.21
24	0.28	23.55	1.53	0.37	-1.41	-0.06	0.25	23.58	1.48	-0.01	-1.51	0.10
25	0.28	23.55	3.02	0.48	-1.11	-0.20	0.26	23.60	2.98	0.52	-1.27	-0.05
26	0.25	26.51	1.52	0.37	-0.44	0.48	0.22	26.53	1.49	-0.51	-0.80	0.51
27	0.27	26.53	2.28	0.32	-0.81	0.63	0.25	26.58	2.24	0.19	-1.03	0.83
28	0.29	26.54	3.77	0.49	0.15	0.61	0.27	26.59	3.71	0.09	-0.11	0.73
29	0.22	29.67	1.90	0.28	0.01	0.13	0.20	29.58	1.86	0.41	-0.47	0.28
30	0.26	29.53	3.04	0.28	-0.66	0.45	0.23	29.57	3.03	-0.46	-0.71	0.47
31	0.23	32.52	2.29	0.37	-0.86	1.23	0.21	32.56	2.24	0.15	-1.09	1.27
32	0.26	32.52	3.78	0.54	-0.63	1.41	0.23	32.56	3.73	-0.56	-0.75	1.44

Table 4.7 TLS-based and MLS-based summary statistics of the derived serviceability measures for the MSE wall at Site-1

	θ_{xp} (deg.)	θ_{yp} (deg.)	θ_{zp} (deg.)	Panel-to-panel Displacement (mm)	θ_{xp} (deg.)	θ_{yp} (deg.)	θ_{zp} (deg.)	Panel-to panel Displacement (mm)
Sample Size	32	32	32	167	32	32	32	167
Minimum Value	-0.65	-3.78	-1.26	-24.50	-0.84	-2.04	-1.43	-29.00
Maximum Value	1.54	2.04	1.41	23.10	0.86	1.12	1.44	32.50
Range	1.26	1.83	1.74	47.60	1.39	1.87	1.91	61.50
Average	0.28	-0.67	-0.10	-0.01	0.06	-0.77	-0.02	0.39
Standard Deviation	0.39	0.92	0.62	8.28	0.46	0.67	0.63	8.59
5^{th} Percentile	-0.64	-1.68	-1.11	-13.60	-0.73	-1.67	-1.08	-11.30
25^{th} Percentile	0.09	-1.06	-0.57	-5.70	-0.31	-1.25	-0.54	-5.60
50^{th} Percentile (median)	0.30	-0.71	-0.07	0.20	0.09	-0.89	0.04	0.10
75^{th} Percentile	0.46	-0.42	0.21	5.40	0.41	-0.51	0.28	5.50
95^{th} Percentile	0.62	0.15	0.63	11.80	0.66	0.20	0.83	13.50
Interquartile Range (IQR)	0.37	0.64	0.78	11.10	0.71	0.74	0.82	11.10

Table 4.8. RMSE of the differences between the TLS-based and MLS-based serviceability measures for the MSE wall at Site-1

	X_o (m)	Y_o (m)	Z_o (m)	θ_{xp} (deg.)	θ_{yp} (deg.)	θ_{zp} (deg.)	Panel-to-panel-displacement (m)
RMSE	0.02	0.05	0.06	0.39	0.55	0.11	0.0178

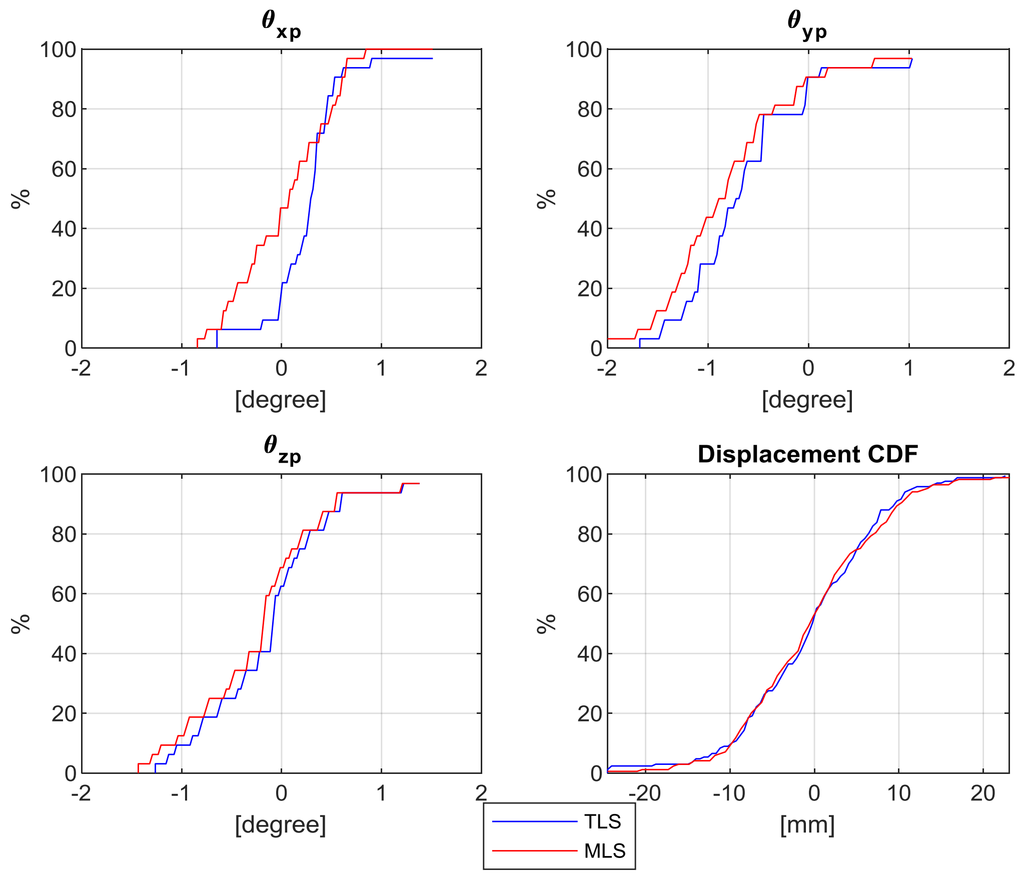

Figure 4.25. Cumulative Distribution Functions (CDF) for panel 3D orientation and panel-to-panel displacement using TLS (in blue) and MLS (in red) point clouds at Site-1

4.6.2 Experimental Results for Site-2

This dataset is used to further highlight the MLS capability in deriving serviceability measures for a large textured MSE wall. As previously mentioned, the MSE wall at Site-2 has a total of 376 panels along two sides (296 panels along Side A and 80 panels along Side B). There are a total of

4 drive runs in two opposite directions – two drive runs in each direction – covering the MSE wall. The drive runs in each direction cover only one side of the MSE wall. Side A and Side B are sectioned into 6 and 4 planar faces, respectively. To illustrate some of the results from the proposed processing strategy, the following discussion focuses on one face with 31 panels. For the overall summary statistics, the serviceability measures for 285 of the 376 panels are reported (incomplete and partially occluded panels were excluded). Similar to the processing workflow for Site-1, the registration between the two scanners (i.e., Riegl and ZF sensors) in a given drive run was first performed. Then, the point clouds from the different drive runs were registered. In total, there were three registration steps for the MLS scans in a given direction (two steps for the registration of the Riegl and ZF scans in each of the two drive runs in that direction and the third step for the alignment of the combined/registered scans from those drive runs). Qualitative evaluation of the alignment following the registration procedure when applied to the scanners' point clouds in a given run and the point clouds from two drive runs is shown in Figure 4.26 and Figure 4.27, respectively. The two different colors (e.g., red and blue) in Figure 4.26 and Figure 4.27 represent two scanners and two different drive runs, respectively. In those figures, four cross-sectional profiles are used to illustrate the alignment quality. The estimated transformation parameters together with the associated statistics are shown in Table 4.9 and Table 4.10. Inspection of the profile alignment in Figure 4.26 and Figure 4.27 as well as the reported transformation parameters in Table 4.9 and Table 4.10 further confirms the derived observations from Site-1; namely, high quality of the system calibration parameters, small discrepancies caused by the GNSS/INS trajectory, and very good alignment following the registration process.

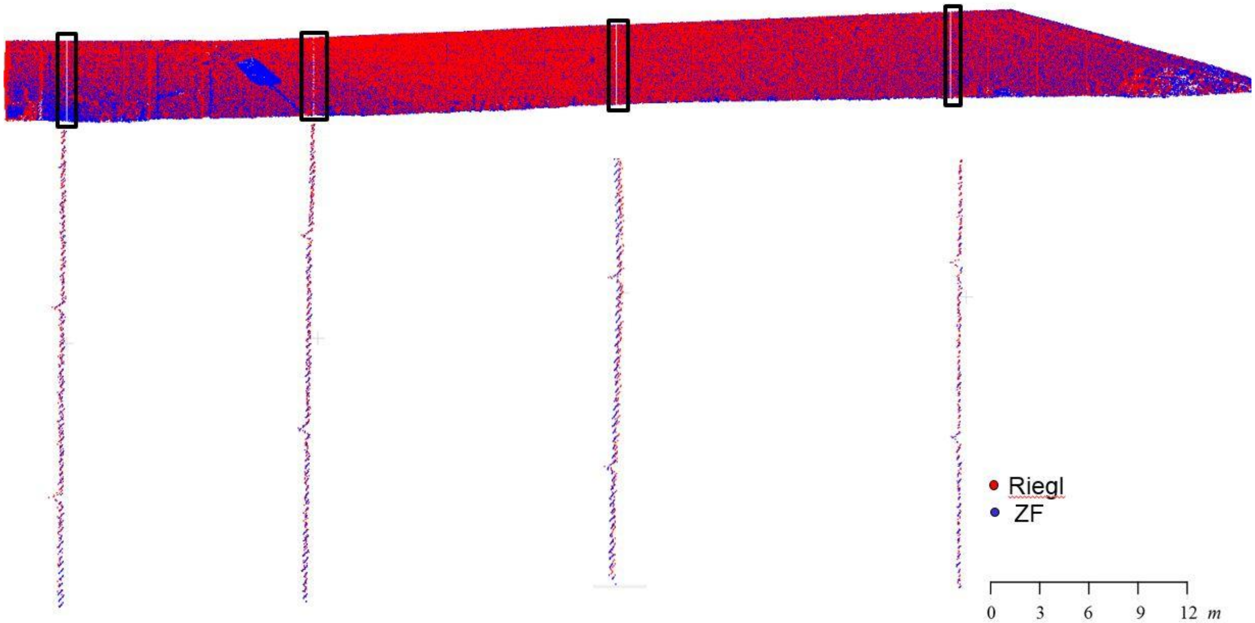

Figure 4.26. Cross sections illustrating the alignment quality of the Riegl and ZF point clouds from a given drive run of the MSE wall at Site-2

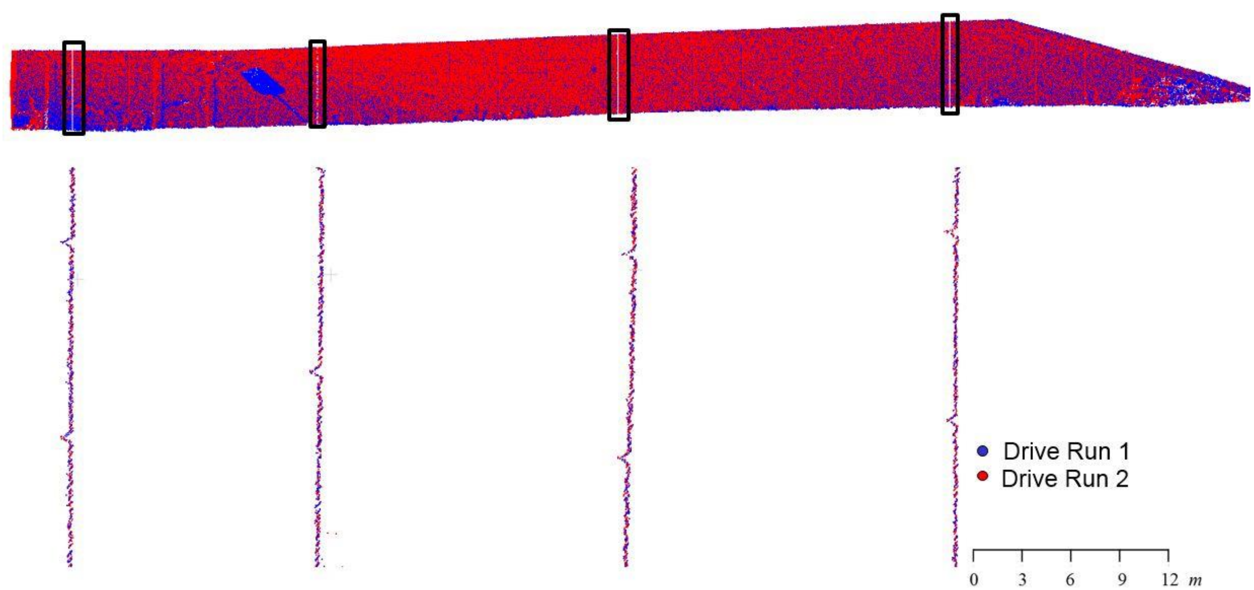

Figure 4.27 Cross sections illustrating the alignment quality of MLS point clouds from two drive runs in the same direction of the MSE wall at Site-2

Table 4.9. Estimated transformation parameters and quality measures (square root of a-posteriori variance factor, average normal distance among point-patch pairs, and RMSE of the normal distances) following the registration of the Riegl and ZF point clouds for one of the drive runs at Site-2

XT (m±mm)	YT (m±mm)	ZT (m±mm)	Ω (deg±sec)	Φ (deg±sec)	K (deg±sec)	$\hat{\sigma}_\circ$ (m)	Average Normal Dist. (m)	RMSE (m)
0.011	0.019	0.014	-0.04	0.13	-0.008	0.0045	0.0033	0.0062
0.02	0.04	0.03	0.011	0.029	0.004			

Table 4.10. Estimated transformation parameters and quality measures (square root of a-posteriori variance factor, average normal distance among point-patch pairs, and RMSE of the normal distances) following the registration of the MLS point clouds from two drive runs of the MSE wall at Site-2

XT (m±mm)	YT (m±mm)	ZT (m±mm)	Ω (deg±sec)	Φ (deg±sec)	K (deg±sec)	$\hat{\sigma}_\circ$ (m)	Average Normal Dist. (m)	RMSE (m)
-0.065	-0.009	-0.037	-0.011	-0.028	0.009	0.0039	0.003	0.0043
0.01	0.02	0.02	0.007	0.014	0.00			

Following the registration of the different point clouds, this research proceeds by deriving the different serviceability measures. The established longitudinal and transversal lines in Figure 4.28 are used for evaluating the angular distortions for one of the MSE wall faces at Site-2. Figure 4.29 the longitudinal and transversal angular distortions for that face as well as the tolerable angular distortions (i.e., denoted by red lines). The horizontal line in Figure 4.29(a) represents the tolerable longitudinal distortions for a joint width of 19 mm (0.75 in.), while the horizontal lines in Figure 4.29(b) represent the tolerable transversal angular distortions, as prescribed in AASHTO, 2014. As shown in Figure 4.29(a) and Figure 4.29(b), this MSE wall face satisfied the longitudinal angular distortion criterion for a joint width of 19 mm (0.75 in.). However, it failed to meet the tolerable transversal angular distortion criterion of 1/240.

The estimated values of the other serviceability measures (namely, the position of the most lower left corner of each panel – X_o, Y_o, and, Z_o – and the angular orientation of each panel – θ_{x_P}, θ_{y_P}, and θ_{z_P}– relating the LF_{cs} and P_{cs} coordinate systems) for the illustrative face with 31 panels are listed in Table 4.11. Table 4.12 provides statistics of the proposed serviceability measures for all the complete/non-occluded panels of the textured MSE wall at Site-2 (285 panels). Although it is instructive to inspect the data provided in Table 4.12 for all the panels constituting the textured MSE wall, a graphical summary is much more intuitive for identifying trends and outliers. Figure 4.30 shows the Cumulative Distribution Functions (CDF) for the three angular values (θ_{x_P}, θ_{y_P}, and θ_{z_P}) and the panel-to-panel normal distance of the MLS dataset at this site. One of the basic assumptions of MSE walls is that the joints (i.e., gaps) between panels are sufficiently close and have minimal offset along the X-axis of the Pcs between neighboring panels - according to FHWA (2009). It can be concluded from this table that 75% of the panels have an offset less than 0.6 cm, which indicates that the wall meets tolerable out-plane offset as prescribed by FHWA (2009).

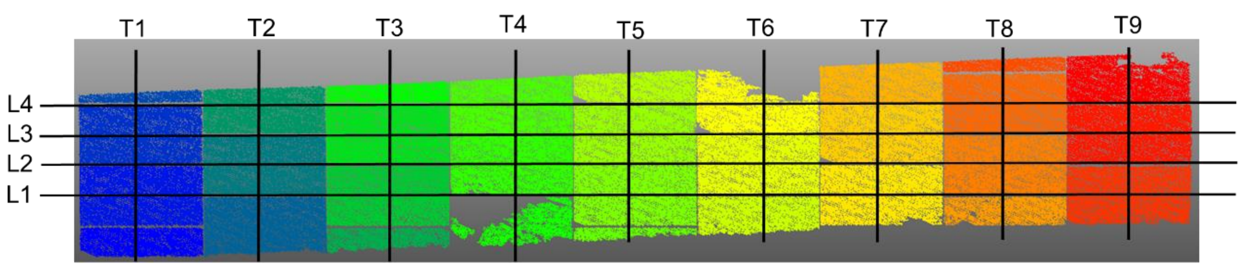

Figure 4.28. Longitudinal and transversal lines used for defining angular distortions for one of the faces of the MSE wall at Site-2

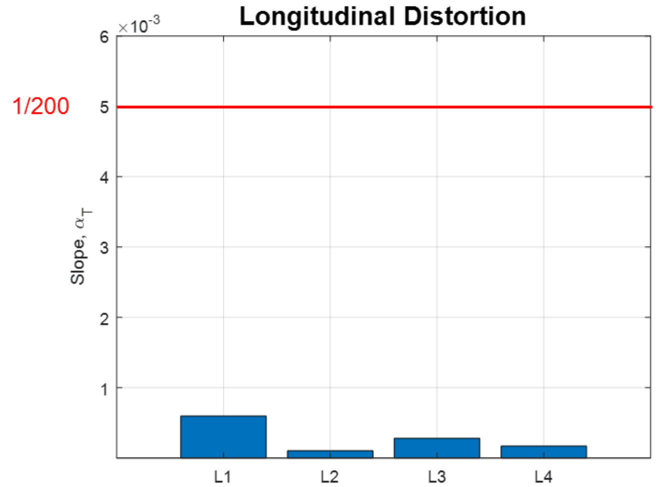

(a)

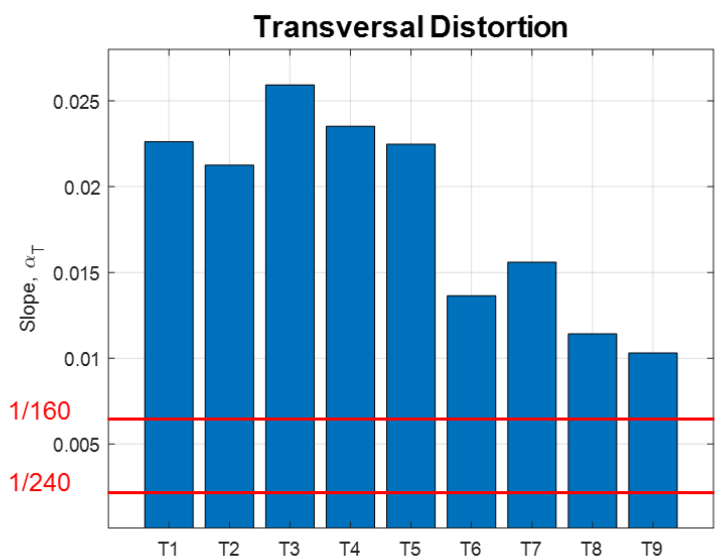

(b)

Figure 4.29. Angular distortions for one of the faces of the MSE wall at Site-2: (a) longitudinal angular distortion along lines L1-L4, and (b) transversal angular distortion along lines T1-T9 (the horizontal red lines represent the tolerable angular distortions)

Table 4.11. MLS-based Panel Parametrization for one of the MSE wall faces at Site-2

ID	Xo (m)	Yo (m)	Zo (m)	θ_{xp} (deg.)	θ_{yp} (deg.)	θ_{zp} (deg.)
1	0.02	0.06	0.13	0.00	0.00	0.96
2	0.03	0.05	0.80	0.71	2.52	0.92
3	0.08	0.05	2.34	-0.12	2.01	1.12
4	0.12	0.00	3.87	-1.11	3.45	1.15
5	-0.02	3.05	0.09	-0.15	1.80	0.29
6	0.00	3.06	1.54	0.88	2.62	0.24
7	0.05	3.05	3.11	-0.29	1.45	0.20
8	-0.04	6.05	0.12	-0.26	0.67	0.58
9	-0.03	6.03	0.81	0.03	2.81	0.48
10	0.02	6.04	2.35	-0.08	2.79	0.30
11	0.06	6.02	3.82	-0.48	1.02	0.30
12	-0.05	9.16	0.51	-0.33	1.31	-0.04
13	-0.03	9.03	1.53	1.02	3.25	-0.31
14	0.05	9.05	3.09	-0.54	0.97	0.19
15	-0.04	12.03	0.35	1.61	-0.55	-0.27
16	-0.04	12.05	0.84	-0.23	3.06	-0.29
17	0.02	12.02	2.38	-0.66	1.88	-0.15
18	0.04	12.04	3.89	-0.22	1.76	0.14
19	-0.03	15.03	0.54	0.99	1.74	0.15
20	0.01	15.03	1.61	-0.28	2.40	0.34
21	0.04	15.05	3.16	-0.30	0.28	0.46
22	-0.04	18.03	0.80	0.45	2.13	-0.24
23	0.00	18.05	2.38	0.71	1.52	-0.03
24	0.02	18.02	3.82	0.33	1.09	0.05
25	-0.03	21.02	0.73	0.60	1.07	-0.63
26	-0.02	21.03	1.55	1.27	3.07	-0.99
27	0.03	21.01	3.09	-0.94	0.60	-0.91
28	0.03	20.96	4.64	-1.93	0.83	-0.32
29	0.01	24.03	0.85	-0.66	3.14	-0.24
30	0.07	24.02	2.35	-0.52	1.07	-0.23
31	0.06	24.00	3.83	-0.26	0.09	-0.17

Table 4.12. MLS-based summary statistics of the serviceability measures for 285 panels of the MSE wall at Site-2

	θ_{xp} (deg.)	θ_{yp} (deg.)	θ_{zp} (deg.)	Panel-to-panel Displacement mm)
Sample Size	285	285	285	1538
Minimum Value	-2.95	-2.09	-1.72	-31.40
Maximum Value	2.85	3.61	1.81	34.90
Range	5.80	5.70	3.53	66.30
Average	0.16	0.55	0.01	-0.21
Standard Deviation	0.92	1.02	0.52	9.03
5th Percentile	-1.10	-0.87	-0.86	-14.70
25th Percentile	-0.37	-0.10	-0.33	-6.40
50th Percentile (median)	0.00	0.41	0.00	-0.30
75th Percentile	0.73	1.12	0.34	5.90
95th Percentile	1.89	2.62	0.87	14.00
Interquartile Range (IQR)	1.10	1.22	0.67	12.30

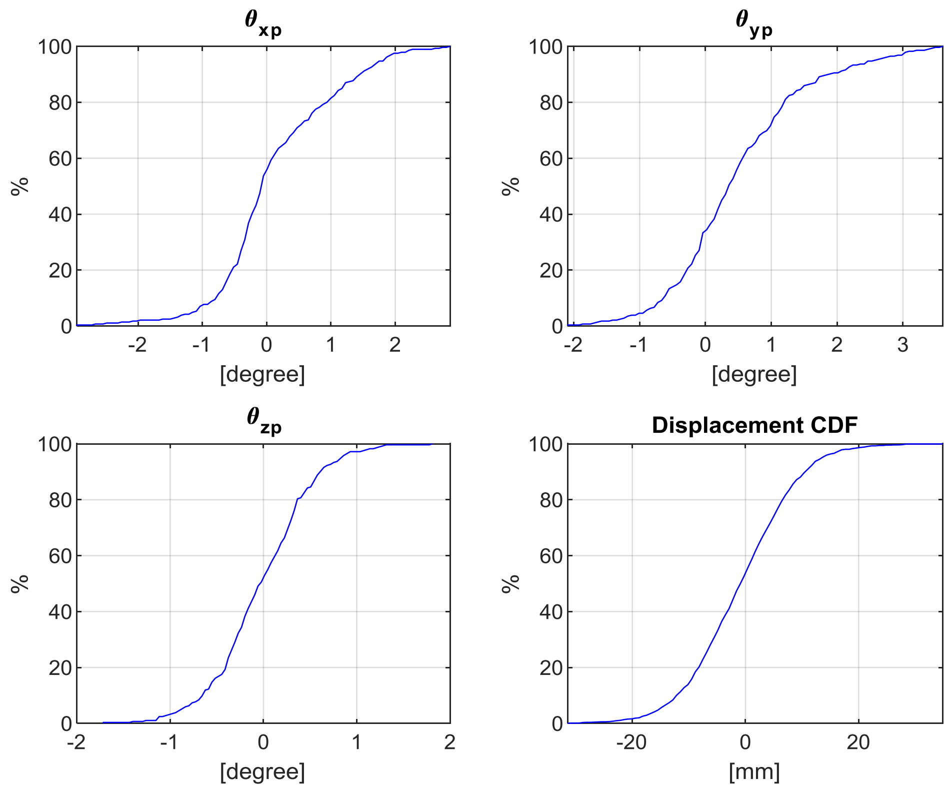

Figure 4.30. Cumulative Distribution Functions (CDF) for the MLS-based panel 3D orientation and panel-to-panel displacement at Site-2

4.7 Conclusions and Recommendations for Future Work

MSE walls are a commonly-used civil infrastructure due to their economic benefits, ease of construction, and accommodating tight right-of-way constraints. Continuous monitoring of MSE walls is necessary to ensure their performance using a wide range of serviceability measures that describe both global and local deformations within the wall. Current approaches for MSE wall monitoring are time consuming, limit access to transportation corridors, and could subject the inspectors and/or instrument operators to risk from incoming traffic. Prior research has shown that TLS is a promising tool for deriving standard/global and new/local serviceability measures. The time-consuming nature of scanner set-up and data collection makes it an impractical approach that could not be scalable. Therefore, this research has proposed the use of MLS for the data acquisition and introduced a processing framework that could produce all types of serviceability measures. Achieving the research objectives has been tested through two case studies with the first one evaluating the comparative performance of TLS and MLS data acquisition modalities. The second case study aimed at illustrating the feasibility of using MLS for monitoring large MSE walls. The key findings/contributions of the proposed acquisition/processing strategy can be summarized as follows:

1. Illustrating the potential of Mobile LiDAR in collecting point clouds with sufficient point density to derive global and local serviceability measures;
2. Introducing a framework for point cloud processing, which include registration, segmentation, panel isolation, and serviceability measures evaluation, more specifically:
    a. A hybrid approach has been introduced for the fine registration of scans from different sensors in a given drive run and scans from different drive runs;
    b. A rigorous procedure has been devised to identify/isolate the individual panels along the MSE wall in a unique manner. For this task, a template matching procedure has been developed to ensure consistent definition of the individual panels along the wall;
    c. The extracted panels are then used to derive both global and local serviceability measures;
3. With an accurate system calibration and high quality GNSS/INS onboard the Mobile LiDAR System (MLS) , point clouds from different sensors and different drive runs are shown to enhance the level of the detail in the collected point clouds;
4. The potential of MLS has been evaluated through comparative evaluation with TLS – derived serviceability measures from TLS and MLS are in close agreement;

5. Extensive testing with multiple real datasets has shown the feasibility of the different components of the proposed processing strategy. To the best of the authors' knowledge, this is the first study of its kind (i.e., first study that has verified the ability of mobile LiDAR in the acquisition and generation of wide-range of serviceability measures for textured MSE walls).

The proposed methodology in this research can be used to establish acceptance criteria for new projects, to derive measures for monitoring the long-term serviceability of existing MSE walls, and/or to propose criteria to assess the serviceability of MSE walls in regions susceptible to natural disasters. This would, in turn, result in reducing costs associated with infrastructure management, and improving the overall quality of our infrastructure by enhancing maintenance operations. Future extensions of the work, will focus on the following actions:

1. Development of a fully automated partitioning process for MSE walls with piece-wise planar façades,
2. Incorporate the reported discrepancies among the point clouds from multiple scans onboard the MLS or different drive runs to improve the system calibration and GNSS/INS trajectory, or identify the proper transformation function relating point clouds from different drive runs (the latter would be critical for excessively long MSE walls),
3. Investigate the impact of environmental parameters (neighboring traffic) as well as technical factors (driving speed) on the derived serviceability measures,
4. Expand the processing strategy to handle MSE walls with non-identical panels that could be either smooth or textured, and
5. Investigate the potential of using lower grade MLS as well as less point density in generating reliable serviceability measures.

5. CONCLUSIONS AND RECOMMENDATIONS FOR FUTURE WORK

This chapter shows the conclusions from the research findings, which were verified by the experimental results using real datasets as well as how the objectives of this dissertation were fulfilled. This dissertation started with an overview of MSE walls monitoring for civil infrastructure systems. It then described the need for periodically testing on individual structural components where the main goal is to measure both standard and recently-available serviceability measures. Traditional instrumentations for infrastructure monitoring were listed and described. The challenges associated with some of the typical instruments were outlined, e.g., necessity for contact, observations of individual points, observation in a single direction/dimension and lack of permanent record. Since using an ultra-high accuracy system (MLS) and the proposed strategy have the potential to overcome such challenges, a literature review was conducted on traditional approaches for structural deformations/displacements monitoring. For example, laser scanning and some instruments which used in the geotechnical area for deformations measurements were reviewed. The four main shortcomings/drawbacks of the reviewed literature were:

1. No such comprehensive strategy in acquisition the data for the object of the interest.
2. The measures are either global (e.g., longitudinal and transversal measures) or within the very close proximity to the structures being monitored (e.g., in 1D direction). This could be deceiving for the decision-maker.
3. Traditional methods for monitoring MSE walls are limited to very close proximity of to the structures being monitored. In addition, because of their dependence on inclinometer measurements, which are affected by electromagnetic interference, signal loss for long distance transmission, and human error, they encounter inherent subjectivity that can

greatly impact the quantity and quality of measurements and affect the overall inference measures of textured MSE walls.

5.1 Conclusion

This dissertation aimed to introduce a new framework for deriving standards and recently-available performance measures for smooth and textured precast concrete panels of MSE walls. First objective was established development of a monitoring strategy that could be used for the delivery of both standard and recently available serviceability measures. Next, the monitoring strategy is based on reliable, scalable data acquisition procedure – more specifically, point clouds captured by a Mobile LiDAR mapping System (MLS) will be used for serviceability measures derivation. The final objective was the strategy could handle MSE walls with smooth or textured precast concrete panels along either planar or piece-wise planar façades. Thus this systematic proposed strategy enabled us effectively used to monitor and assess the long-term performance of MSE walls. The ultimate objective of this research was to introduce an approach mathematical characterization and to accurately evaluate and quantify any deformation of MSE walls of each panel with respect to Levelled Face coordinate system (LF_{cs}). How the intended objectives were met as well as the advantages and shortcomings of the approaches proposed in this dissertation are discussed.

5.2 Contributions of the dissertation

MSE walls are a commonly-used civil infrastructure due to its economic benefits, ease of construction, and managing tight right-of-way constraints. Continuous monitoring of MSE walls is necessary to ensure its performance using a wide range of serviceability measures that describe both global and local deformations within the wall. Current approaches for MSE wall monitoring are time consuming, limit access to transportation corridors, and could subject the inspectors and/or instrument operators to risk from incoming traffic. Prior research has shown that TLS is a promising tool for deriving standard/global and new/local serviceability measures. The consumed time by the scanner set-up and data collection makes it impractical approach that could not be scalable. Therefore, this study has proposed the use of MLS for the data acquisition and introduced a processing framework that could produce all types of serviceability measures. Achieving the research objectives has been tested through two case studies with the first one evaluating the comparative performance of TLS and MLS data acquisition modalities. The second case study aimed at illustrating the feasibility of using MLS for monitoring large MSE walls. The key findings/contributions of the proposed acquisition/processing strategy can be summarized as follows:

1. Illustrating the potential of Mobile LiDAR in collecting point clouds with sufficient point density to derive global and local serviceability measures;
2. Introducing a framework for point cloud processing, which include registration, segmentation, panel isolation, and serviceability measures evaluation, more specifically:
    a. A hybrid approach has been introduced for the fine registration of scans from different sensors in a given drive run and scans from different drive runs;
    b. A rigorous procedure has been devised to identify/isolate the individual panels along the MSE wall in a unique manner. For this task, a template matching procedure has been developed to ensure consistent definition of the individual panels along the wall;
    c. The extracted panels are then used to derive both global and local serviceability measures;

d. With an accurate system calibration and high quality GNSS/INS onboard the Mobile LiDAR System (MLS), point clouds from different sensors and different drive runs are shown to enhance the level of the detail in the collected point clouds;

3. The potential of MLS has been evaluated through comparative evaluation with TLS – derived serviceability measures from TLS and MLS are in close agreement;
4. Extensive testing with multiple real datasets has shown the feasibility of the different components of the proposed processing strategy. To the best of the authors' knowledge, this is the first study of its kind (i.e., first study that has verified the ability of mobile LiDAR in the acquisition and generation of wide-range of serviceability measures for textured MSE walls).

The proposed methodology in this research can be used to establish acceptance criteria for new projects, to derive measures for monitoring the long-term serviceability of existing MSE walls, and/or to propose criteria to assess the serviceability of MSE walls in regions susceptible to natural disasters. This would, in turn, result in reducing costs associated with infrastructure management, and improving the overall quality of our infrastructure by enhancing maintenance operations. Future extensions of the work will focus on the following actions:

5.3 Recommendations for future work

For future work, we plan to focus on the following activities:

1. Development of a fully-automated partitioning process for MSE walls with piece-wise planar surfaces,
2. Incorporate the reported discrepancies among the point clouds from multiple scans onboard the MLS or different drive runs to improve the system calibration and GNSS/INS trajectory,

3. Investigate the impact of environmental parameters (neighboring traffic) as well as technical factors (driving speed) on the derived serviceability measures,
4. Expand the processing strategy to handle MSE walls with non-identical panels that could be either smooth or textured, and
5. Investigate the potential if using lower grade MLS in generating reliable serviceability measures.

REFERENCES

AASHTO. (2014). AASHTO LRFD bridge design specifications - 7th edition. American Association of State Highway and Transportation Officials, Washington, DC, USA.

Abu-Hejleh, N., McMullen, M., Hearn, G., & Zornberg, J. G. (2001). Design and Construction Guidelines for MSE Walls with Independent Full-height Facing Panels (Vol. 5). Report No. CDOT-DTD-R-2001.

Al-Durgham, K., Habib, A., & Kwak, E. (2013). RANSAC approach for automated registration of terrestrial laser scans using linear features. *ISPRS Int. Arch. Photogramm. Remote Sens. Spat. Inf. Sci*, *2*, 13-18.

Al-Durgham, M., & Habib, A. (2013). A framework for the registration and segmentation of heterogeneous LiDAR data. *Photogrammetric Engineering & Remote Sensing*, *79*(2), 135-145.

Al-Rawabdeh, A., Moussa, A., Foroutan, M., El-Sheimy, N., & Habib, A. (2017). Time series UAV image-based point clouds for landslide progression evaluation applications. *Sensors*, *17*(10), 2378.

Ansari, F. (Ed.). (2005). Sensing issues in civil structural health monitoring (p. 525). Dordrecht, The Netherlands: Springer.

Batten, M., Powrie, W., Boorman, R., Yu, H. T., & Leiper, Q. (1999). Use of vibrating wire strain gauges to measure loads in tubular steel props supporting deep retaining walls. *Proceedings of the Institution of Civil Engineers-Geotechnical Engineering*, *137*(1), 3-13.

Berg, R. R., Christopher, B. R., Samtani, N. C., & Berg, R. R. (2009). *Design of mechanically stabilized earth walls and reinforced soil slopes–Volume I* (No. FHWA-NHI-10-024). United States. Federal Highway Administration.

Besl, P. J., & McKay, N. D. (1992, April). Method for registration of 3-D shapes. In *Sensor fusion IV: control paradigms and data structures* (Vol. 1611, pp. 586-606). International Society for Optics and Photonics.

Brownjohn, J. M. (2006). Structural health monitoring of civil infrastructure. Philosophical Transactions of the Royal Society A: Mathematical, Physical and Engineering Sciences, 365(1851), 589-622.

California Department of Transportation. 2011. "Terrestrial laser scanning specifications." Accessed July 04, 2018.
http://www.dot.ca.gov/hq/row /landsurveys/SurveysManual/15_Surveys.pdf

Chang, P. C., Flatau, A., & Liu, S. C. (2003). Health monitoring of civil infrastructure. *Structural health monitoring*, *2*(3), 257-267.

Cleveland, L. J., & Wartman, J. (2006). Principles and applications of digital photogrammetry for geotechnical engineering. In Site and Geomaterial Characterization (pp. 128-135).

Detchev, I., Habib, A., & El-Badry, M. (2013). Dynamic beam deformation measurements with off-the-shelf digital cameras. *Journal of Applied Geodesy*, *7*(3), 147-157.

Dunnicliff, J. (1993). Geotechnical instrumentation for monitoring field performance. John Wiley & Sons.

Faro Laser Scanner Focus X330 Specification (2013). Available online: http://geosense.gr/assets/pdf/x330.pdf (accessed on 07/04/2018)

Farrar, C. R., & Worden, K. (2006). An introduction to structural health monitoring. *Philosophical Transactions of the Royal Society A: Mathematical, Physical and Engineering Sciences*, *365*(1851), 303-315.

Fischler, M. A., & Bolles, R. C. (1981). Random sample consensus: a paradigm for model fitting with applications to image analysis and automated cartography. *Communications of the ACM*, *24*(6), 381-395.

Fischler, M. A., & Bolles, R. C. (1981). Random sample consensus: a paradigm for model fitting with applications to image analysis and automated cartography. Communications of the ACM, 24(6), 381-395.

Freeman, H., & Shapira, R. (1975). Determining the minimum-area encasing rectangle for an arbitrary closed curve. *Communications of the ACM*, *18*(7), 409-413.

Geosense, Marton Geotechnical Services Ltd. APPLICATION GUIDE - INCLINOMETERS (2014). Available online: November 30, 2019: https://www.geosense.co.uk/media/BlockAttributeValueFile/140/file/1InclinometersApplicationGuideV1.0.pdf

González-Aguilera, D., Gómez-Lahoz, J., Muñoz-Nieto, Á., & Herrero-Pascual, J. (2008). Monitoring the health of an emblematic monument from terrestrial laser scanner. *Nondestructive Testing and Evaluation*, *23*(4), 301-315.

Gordon, S. J., & Lichti, D. D. (2007). Modeling terrestrial laser scanner data for precise structural deformation measurement. *Journal of surveying engineering*, *133*(2), 72-80.

Grant, D., Bethel, J., & Crawford, M. (2012). Point-to-plane registration of terrestrial laser scans. ISPRS Journal of Photogrammetry and Remote Sensing, 72, 16-26.

Green, G. E., & Mikkelsen, P. E. (1988). Deformation measurements with inclinometers. *Transportation Research Record*, (1169).

Habib, A., & Lin, Y. J. (2016). Multi-class simultaneous adaptive segmentation and quality control of point cloud data. *Remote Sensing*, *8*(2), 104.

Habib, A., Bang, K. I., Kersting, A. P., & Chow, J. (2010). Alternative methodologies for LiDAR system calibration. *Remote Sensing*, *2*(3), 874-907.

Habib, A., Detchev, I., & Bang, K. (2010). A comparative analysis of two approaches for multiple-surface registration of irregular point clouds. *Int. Arch. Photogramm. Remote Sens. Spat. Inf. Sci*, *38*(1).

Habib, A., Detchev, I., & Bang, K. (2010). A comparative analysis of two approaches for multiple-surface registration of irregular point clouds. *Int. Arch. Photogramm. Remote Sens. Spat. Inf. Sci*, *38*(1).

Inaudi, D., & Glisic, B. (2008, May). Overview of fibre optic sensing applications to structural health monitoring. In Symposium on Deformation Measurement and Analysis (pp. 1-10).

Indiana Department of Transportation, "Indiana Department of Transportation Standard Specifications 2016," October, 2019 [Online]. Available: http://www.in.gov/dot/div/contracts/standards/book/sep15/2016Master.pdf

Jiang, Y., Han, J., Parsons, R. L., & Cai, H. (2015). *Field monitoring of mechanically stabilized earth walls to investigate secondary reinforcement effects* (No. KS-15-09). Kansas. Dept. of Transportation. Bureau of Research.

Knaak, T. (2012). "Structural wall monitoring," TopoDOT Tech Notes #1017 rev: A, Certainty 3D, Orlando, FL.

Koerner, R. M., & Koerner, G. R. (2011). Recommended Layout of Instrumentation to Monitor Potential Movement of MSE Walls, Berms and Slopes. *GRI White Paper*, *19*, 04.

Koerner, R. M., & Koerner, G. R. (2011). The importance of drainage control for geosynthetic reinforced mechanically stabilized earth walls. *Journal of GeoEngineering*, *6*(1), 3-13.

Kuang, K. S., Cantwell, W. J., & Scully, P. J. (2002). An evaluation of a novel plastic optical fibre sensor for axial strain and bend measurements. Measurement Science and Technology, 13(10), 1523.

Laefer, D., & Lennon, D. (2008). Viability assessment of terrestrial LiDAR for retaining wall monitoring. In *GeoCongress 2008: Geosustainability and Geohazard Mitigation* (pp. 247-254).

Lienhart, W., Monsberger, C., Kalenjuk, S., & Woschitz, H. (2018). High Resolution Monitoring of Retaining Walls with Distributed Fibre Optic Sensors and Mobile Mapping Systems. In *7th Asia-Pacific Workshop on Structural Health Monitoring*.

Lin, Y. J., Habib, A., Bullock, D., & Prezzi, M. (2019). Application of High-Resolution Terrestrial Laser Scanning to Monitor the Performance of Mechanically Stabilized Earth Walls with Precast Concrete Panels. *Journal of Performance of Constructed Facilities*, *33*(5), 04019054.

Lostumbo, J. M., & Artieres, O. (2011). Geosynthetic Enabled with Fiber Optic Sensors for MSE Bridge Abutment Supporting Shallow Bridge Foundation. In Geo-Frontiers 2011: Advances in Geotechnical Engineering (pp. 3497-3504).

Lostumbo, J. M., & Artieres, O. (2011). Geosynthetic Enabled with Fiber Optic Sensors for MSE Bridge Abutment Supporting Shallow Bridge Foundation. In Geo-Frontiers 2011: Advances in Geotechnical Engineering (pp. 3497-3504).

Maas, H. G., & Hampel, U. (2006). Photogrammetric techniques in civil engineering material testing and structure monitoring. Photogrammetric Engineering & Remote Sensing, 72(1), 39-45.

McGuire, M. P., Yust, M. B. S., & Collin, J. G. (2016). As-Built Verification, Condition Assessment, and Forensic Analysis of Mechanically-Stabilized Earth Walls Incorporating Terrestrial Lidar. In *Geotechnical and Structural Engineering Congress 2016* (pp. 467-482).

McGuire, M. P., Yust, M. B., & Shippee, B. J. (2017). Application of Terrestrial Lidar and Photogrammetry to the As-Built Verification and Displacement Monitoring of a Segmental Retaining Wall. In *Geotechnical Frontiers 2017* (pp. 461-471).

McGuire, M. P., Yust, M. B., & Shippee, B. J. (2017). Application of Terrestrial Lidar and Photogrammetry to the As-Built Verification and Displacement Monitoring of a Segmental Retaining Wall. In Geotechnical Frontiers 2017 (pp. 461-471).

Mikhail, E. M., Bethel, J. S., & McGlone, J. C. (2001). Introduction to modern photogrammetry. New York.

Mills, J. P., Newton, I., & Peirson, G. C. (2001). Pavement deformation monitoring in a rolling load facility. The Photogrammetric Record, 17(97), 07-24.

Mohamad, H., Soga, K., Pellew, A., & Bennett, P. J. (2011). Performance monitoring of a secant-piled wall using distributed fiber optic strain sensing. Journal of Geotechnical and Geoenvironmental Engineering, 137(12), 1236-1243.

Novatel_IMU-ISA-100C Specification. Available online: https://www.novatel.com/assets/Documents/Papers/IMUISA100CD19539v2.pdf

Oats, R. C., Escobar-Wolf, R., & Oommen, T. (2019). Evaluation of photogrammetry and inclusion of control points: Significance for infrastructure monitoring. Data, 4(1), 42.

Oats, R., Escobar-Wolf, R., & Oommen, T. (2017). A Novel Application of Photogrammetry for Retaining Wall Assessment. *Infrastructures*, *2*(3), 10.

Olsen, M. J., Kuester, F., Chang, B. J., & Hutchinson, T. C. (2009). Terrestrial laser scanning-based structural damage assessment. Journal of Computing in Civil Engineering, 24(3), 264-272.

Olsen, M. J., Kuester, F., Chang, B. J., & Hutchinson, T. C. (2009). Terrestrial laser scanning-based structural damage assessment. Journal of Computing in Civil Engineering, 24(3), 264-272.

Oskouie, P., Becerik-Gerber, B., & Soibelman, L. (2014). Automated cleaning of point clouds for highway retaining wall condition assessment. In *Computing in Civil and Building Engineering (2014)* (pp. 966-974).

Oskouie, P., Becerik-Gerber, B., & Soibelman, L. (2016). Automated measurement of highway retaining wall displacements using terrestrial laser scanners. *Automation in Construction*, *65*, 86-101.

Passe, P.D., 2000. Mechanically Stabilized Earth Wall Inspector's Handbook. State of Florida, Department of Transportation.

Pei, H. F., Yin, J. H., Zhu, H. H., Hong, C. Y., Jin, W., & Xu, D. S. (2012). Monitoring of lateral displacements of a slope using a series of special fibre Bragg grating-based in-place inclinometers. Measurement Science and Technology, 23(2), 025007.

Ravi, R., Lin, Y. J., Elbahnasawy, M., Shamseldin, T., & Habib, A. (2018). Simultaneous System Calibration of a Multi-LiDAR Multicamera Mobile Mapping Platform. *IEEE Journal of selected topics in applied earth observations and remote sensing*, *11*(5), 1694-1714.

Rearick, A., & Khan, A. (2017). MSE Wall Design and Construction Policy Updates.

Riegl Specification". Available online: http://www.riegl.com/uploads/tx_pxpriegldownloads/Datasheet-RIEGL_VUX-1HA__2018-04-26.pdf

Scaioni, M., Alba, M., Roncoroni, F., & Giussani, A. (2010). Monitoring of a SFRC retaining structure during placement. *European Journal of Environmental and Civil Engineering*, *14*(4), 467-493.

Schmidt, J. M. (2011). MSE Wall Engineering–A New Look at Contracting, Design, and Construction.

Schneider-Gloetzl, J., Gloetzl, R., Krebber, K., Liehr, S., Wendt, M., & Wosniok, A. (2010). Geotechnical monitoring of construction activities by distributed fiber optic sensors embedded in geotextiles.

Schneider-Gloetzl, J., Gloetzl, R., Krebber, K., Liehr, S., Wendt, M., & Wosniok, A. (2010). Geotechnical monitoring of construction activities by distributed fiber optic sensors embedded in geotextiles.

Schneider-Gloetzl, J., Gloetzl, R., Krebber, K., Liehr, S., Wendt, M., & Wosniok, A. (2010). Geotechnical monitoring of construction activities by distributed fiber optic sensors embedded in geotextiles.

Shamseldin, T. (2018). System Architecture, Calibration, and Control for LiDAR Systems Onboard Unmanned Vehicles (Doctoral dissertation, Purdue University).

Udd, E. (1996). Fiber optic smart structures. Proceedings of the IEEE, 84(6), 884-894.

Wei, Y. M., Kang, L., & Yang, B. (2013). Applications of structure from motion: a survey. Journal of Zhejiang University SCIENCE C, 14(7), 486-494.

Yang, G., Zhang, B., Lv, P., & Zhou, Q. (2009). Behaviour of geogrid reinforced soil retaining wall with concrete-rigid facing. Geotextiles and Geomembranes, 27(5), 350-356.

ZF Specification". Available online: https://www.zflaser.com/fileadmin/editor/Datenblaetter/Z_F_PROFILER_9012_Datasheet_E_final_compr.pdf